CHAOS AND MOMENTUM DIFFUSION OF THE CLASSICAL AND QUANTUM KICKED ROTOR

Yindong Zheng, B.S., M.S.

Dissertation Prepared for the Degree of

DOCTOR OF PHILOSOPHY

UNIVERSITY OF NORTH TEXAS

August 2005

APPROVED:

Donald H. Kobe, Major Professor
Paolo Grigolini, Committee Member
Jacek Kowalski, Committee Member
Arkadii Krokhin, Committee Member
Duncan Weathers, Program Coordinator
Floyd McDaniel, Chair of the Department of Physics
Sandra L. Terrell, Dean of the Robert B. Toulouse School of Graduate Studies

Zheng, Yindong, Chaos and Momentum Diffusion of the Classical and Quantum Kicked Rotor. Doctor of Philosophy (Physics), August 2005, 121 pp., 5 tables, 34 figures, references, 68 titles.

The de Broglie-Bohm (BB) approach to quantum mechanics gives trajectories similar to classical trajectories except that they are also determined by a quantum potential. The quantum potential is a "fictitious potential" in the sense that it is part of the quantum kinetic energy. We use quantum trajectories to treat quantum chaos in a manner similar to classical chaos. For the kicked rotor, which is a bounded system, we use the Benettin, *et al.* method to calculate both classical and quantum Lyapunov exponents as a function of control parameter K and find chaos in both cases. Within the chaotic sea we find in both cases nonchaotic stability regions for K equal to multiples of π. For even multiples of π the stability regions are associated with classical accelerator mode islands and for odd multiples of π they are associated with new oscillator modes. We examine the structure of these regions.

Momentum diffusion of the quantum kicked rotor is studied with both BB and standard quantum mechanics (SQM). A general analytical expression is given for the momentum diffusion at quantum resonance of both BB and SQM. We obtain agreement between the two approaches in numerical experiments. For the case of nonresonance the quantum potential is not zero and must be included as part of the quantum kinetic energy for agreement. The numerical data for momentum diffusion of classical kicked rotor is well fit by a power law DN^{β} in the number of kicks N. In the anomalous momentum diffusion regions due to accelerator modes the exponent $\beta(K)$ is slightly less than quadratic, except for a slight dip, in agreement with an upper bound $(K^2/2)N^2$. The

corresponding coefficient $D(K)$ in these regions has three distinct sections, most likely due to accelerator modes with period greater than one.

We also show that the local Lyapunov exponent of the classical kicked rotor has a plateau for a duration that depends on the initial separation and then decreases asymptotically as $O(t^{-1}lnt)$, where t is the time. This behavior is consistent with an upper bound that is determined analytically.

ACKNOWLEDGEMENTS

I would like to thank everybody who helped me at any point of this dissertation.

I am very grateful to Professor Dr. Donald H. Kobe for his continuing interest in Lyapunov exponent, momentum diffusion, de Broglie-Bohm approach of quantum mechanics and the kicked rotor. I also appreciate greatly his professional and moral support and his encouragement. Without Professor Kobe's help, it would have been impossible for me to have finished this dissertation.

I would also thank Professors Paolo Grigolini, Arkadii Krokhin, Jacek Kowalski, Wolfgang Schleich, Constantino Tsallis, Williams D. Deering, John Neuberger, and Robert O' Connell, as well as Dr. Gerardo Aquino, for their helpful discussions.

I appreciate greatly the encouragement and discussions with Professor Marlan O. Scully on the research, especially in connection with the de Broglie-Bohm approach to quantum mechanics.

This work was partially supported by ONR N00014-03-1-0639/TAMU TEES 53494.

Last but not least, I am very grateful to my parents for their teaching, encouragement, understanding and support. This dissertation is dedicated to my beloved and respected parents.

CONTENTS

ACKNOWLEDGEMENTS ii

LIST OF TABLES vii

LIST OF FIGURES viii

1 INTRODUCTION 1

2 DEFINITION OF CLASSICAL AND QUANTUM CHAOS 5

2.1 Classical Deterministic Chaos 5

2.2 Quantum Theory of Motion 6

2.3 Quantum Lyapunov Exponent 9

3 THE KICKED ROTOR MODEL 11

3.1 Introduction 11

3.2 Classical Kicked Rotor 12

3.2.1 Simple Pendulum Model 12

3.2.2 Hamiltonian of Classical Kicked Rotor 12

3.2.3 Mapping of the Classical Kicked Rotor 13

3.3 Quantum Kicked Rotor 15

3.4 Atom Optics Kicked Rotor 17

3.5 Experimental Realization of Atom Optics Kicked Rotor 20

4 CLASSICAL CHAOS OF THE KICKED ROTOR 23

4.1 Introduction 23

4.2 Local Lyapunov Exponent 25

4.3 Numerical Calculations for Trajectories of the Kicked Rotor 26

4.4 Upper Bound for Local Lyapunov Exponents 33

4.5 Lyapunov Exponent of the Kicked Rotor 36

4.6 Conclusion 42

5 MOMENTUM DIFFUSION IN THE CLASSICAL KICKED ROTOR 43

5.1 Introduction 43

5.2 Equations for Momentum Diffusion 44

5.3 Calculation of Momentum Diffusion 46

5.4 Anomalous Momentum Diffusion 49

5.5 Linear Momentum Diffusion 54

5.6 Conclusion 57

6 QUANTUM CHAOS OF THE KICKED ROTOR:

DE BROGLIE-BOHM APPROACH 59

6.1 Introduction 59

6.2 Solution of the Schrödinger Equation 60

6.3 Mapping of Bohmian Trajectories of the Kicked Rotor at Quantum Resonance 62

6.4 Numerical Experiment of Bohmian Trajectories 64

6.5 Conclusion 67

7 QUANTUM MOMENTUM DIFFUSION OF THE KICKED ROTOR:

STANDARD QUANTUM MECHANICAL APPROACH 70

7.1 Introduction 70

7.2 Momentum Diffusion at Quantum Resonance 71

7.3 Numerical Results for SQM 73

7.4 Conclusion 77

8 QUANTUM MOMENTUM DIFFUSION OF THE KICKED ROTOR:

DE BROGLIE-BOHM APPROACH 79

8.1 Introduction 79

8.2 Fictitious Quantum Potential 80

8.3 Momentum Diffusion at Resonance: BB 82

8.4 Numerical Results for BB 84

8.5 Conclusion 86

9 SUMMARY AND DISCUSSION 88

APPENDICES 90

A MATHEMATICAL DETAILS 91

A.1 Dimensionless Hamiltonian 91

A.2 Schrödinger Equation in Dimensionless Units 92

A.3 Worst Case Scenario 93

A.4 Quantum Potential Terms 96

A.5 Expansion in Bessel Function 98

A.6 Coefficients 99

A.7 Mathematical Induction for the Oscillator Modes 100

B FIGURES OF CLASSICAL STABILITY REGIONS AT CHAOTIC SEA 102

C FIGURES OF CLASSICAL ANOMALOUS MOMENTUM DIFFUSION 106

D FIGURES OF QUANTUM STABILITY REGIONS IN THE CHAOTIC SEA 115

BIBLIOGRAPHY 119

LIST OF TABLES

4.1 Classical evolution of the momentum and angle for $m\pi$ group with m odd. 39

5.1 Properties of anomalous diffusion modes for K between 0 and 50. 53

5.2 Properties of anomalous diffusion modes for K between 50 and 100. 53

7.1 Standard quantum mechanics quadratic diffusion rates D at resonance with different control parameters K and different initial states for numerical simulation data and theoretical values in Eq. (7.2). 77

8.1 de Broglie-Bohm quadratic diffusion rates D at resonance with different control parameters K and an initial zero-momentum $(p_0 = 0)$ for numerical simulation data and theoretical values in Eq. (8.12). 86

LIST OF FIGURES

3.1 Illustration of classical kicked rotor with x the angle from vertical. (a) simple pendulum. (b) one example of classical kicked rotor. 14

3.2 Illustration of experimental realization of atom optics kicked rotor. (a) is the core part of the experimental setup while (b) is the illustration of two level atom in standing wave potential. 21

4.1 Trajectory simulation and Lyapunov exponent in the chaotic regime with $K = 10$ as a function of time N. (a) Simulation of two adjacent trajectories in coordinate space with initial separation distance $d(0) = 10^{-6}$ and $x_0 = 3$. (b) Ratio $d(N)/d(0)$ of distances in phase space as a function of time N. (c) Logarithm of $d(N)/d(0)$. (d) Corresponding local Lyapunov exponent L in Eq. (4.1). 27

4.2 Local Lyapunov exponent L as a function of time N for $K = 10$, $x_0 = 3$ and different values of $d(0)$. From left to right $d(0) = 10^{-6}, 10^{-8}, 10^{-10}$, and 10^{-12}, respectively. . 29

4.3 Local Lyapunov exponent L as a function of time N for $K = 10$, $x_0 = 0$ and different values of $d(0)$. From left to right $d(0) = 10^{-5}, 10^{-15}, 10^{-25}$, and 10^{-35}, respectively. 30

4.4 Trajectory simulation in the nonchaotic regime for $K = 0.96, x_0 = 3$ and $d(0) = 10^{-6}$. On the scale shown the two trajectories overlap each other. The dashed line is only a guide for the eye. 32

4.5 Lyapunov exponent of the classical trajectories from Benettin *et al.* approach with respect to K. 2000 points were evenly sampled on K. The inset shows the transition from the non-chaotic to chaotic regimes. 1000 points were sampled on K. 37

4.6 Higher resolution on K for the Lyapunov exponent of the classical trajectories at Benettin *et al.* approach. $\Delta K = 0.002$ (a) $K = 3\pi$ region. Dashed line points to $K = 3\pi$ and solid lines illustrate region of Eq. (4.13) (b) $K = 4\pi$ region. Solid lines illustrate region of Eq. (4.12) while the dashed line is the right boundary of the second accelerator mode islands(c) $K = 5\pi$ region. Dashed line points to $K = 5\pi$ and solid lines illustrate region of Eq. (4.13) (d) $K = 6\pi$ region. Solid lines illustrate region of Eq. (4.12) and the dashed line is the right edge of the second accelerator mode islands. 38

4.7 Trajectory simulation for the illustration of the chaotic and two types of non-chaotic. The initial distance for the two trajectories in each subgraph is $d_0 = 10^{-6}$, the initial momentum is $p_0 = 0$, and the initial position is $x_0 = \pi/2$. (a) $K = 4\pi$. (b) $K = 9.2643$. (c) $K = 3\pi$. (d) $K = 9.6$. 41

5.1 Linear diffusion rate D_L divided by $K^2/2$ for K from 0 to 100. The solid line is eq. (5.6). 47

5.2 Values of exponent $\beta(K)$ in Eq. (5.7) around nonlinear regions of anomalous diffusion for (a) $K_1 = 6.49$, (b) $K_4 = 25.17$, (c) $K_8 = 50.28$ and (d) $K_{12} = 75.44$. The increment in K used for computation is $1/20$ for (a) and (b), while it is $1/80$ for (c) and (d). . . . 50

5.3 Values of coefficient $D(K)$ in Eq. (5.7) around nonlinear regions of diffusion for (a) $K_1 = 6.49$, (b) $K_4 = 25.17$, (c) $K_8 = 50.28$ and (d) $K_{12} = 75.44$. The increment in K used for computation is $1/20$ for (a), while it is $1/80$ for (b), (c) and (d). 51

5.4 Momentum diffusion for several values of the control parameter K near modes 1 and 8 and the least squares fit to eq. (5.7) for K_1 and K_8 using data between kicks from 1000 to 5000. 55

5.5 Linear fit to the diffusion for $K = 10$. 56

6.1 Benettin *et al.* approach for the Lyapunov exponent for Bohmian trajectories. $K = 12.5, 6.49, 2\pi$, and 0.55. 65

6.2 Lyapunov exponent of the Bohmian trajectories at Benettin *et al.* approach respecting to K. 2000 points are evenly sampled on K. The small figure shows the transition of non-chaotic to chaotic. 500 points are evenly sampled. 66

6.3 Higher resolution on Lyapunov exponent of the Bohmian trajectories from the Benettin *et al.* approach with respect to K. $\Delta K = 0.002$ (a) $K = \pi$ region, (b) $K = 2\pi$ region, (c) $K = 3\pi$ region (d) $K = 4\pi$ region. 68

7.1 Probability distribution and momentum diffusion for standard quantum mechanics with an initial zero-momentum state. The control parameter is $K = 12.5$. (a) Probability distribution of momentum eigenvalues as a function of time from 0 to 100 kicks for nonresonance with $\bar{k} = 2$. (b) Momentum diffusion as a function of time (kicks) for the nonresonant case in (a). The dots are numerical data and the dash-dot line is the classical $(K^2/2)N$ for reference. (c) Probability distribution of momentum eigenvalues as a function of time from 0 to 100 kicks for resonance with $\bar{k} = 4\pi$. (d) Momentum diffusion as a function of time (kicks) for resonant case in (c). The dots are numerical data, the dash-dot line is $(K^2/2)N^2$ in Eq. (7.3), and the solid line is a fitted quadratic curve. 74

7.2 Probability distribution and momentum diffusion for standard quantum mechanics with an initial Gaussian distribution of momentum eigenvalues. The control parameter is $K = 12.5$. (a) Probability distribution of momentum eigenvalues as a function of time from 0 to 100 kicks for nonresonance with $\bar{k} = 2$. (b) Momentum diffusion as a function of time (kicks) for the nonresonant case in (a). The dots are numerical data and the dash-dot line is the classical $(K^2/2)N$ for reference. (c) Probability distribution of momentum eigenvalues as a function of time from 0 to 100 kicks for resonance with $\bar{k} = 4\pi$. (d) Momentum diffusion as a function of time (kicks) for resonant case in (c). The dots are numerical data, the dash-dot line is the theoretical curve in Eq. (7.5), and the solid line is a fitted quadratic curve. 76

8.1 Momentum diffusion de Broglie-Bohm approach with an initial zero-momentum state. The control parameter is $K = 12.5$. Subgraphs (a), (b), and (c) are for the nonresonant case with $\bar{k} = 2$, where the dash-dot lines are the classical $(K^2/2)N$ for reference. (a) The numerical data of a weighted average for $(S')^2$ for time from 0 to 100 kicks. (b) The numerical data of a weighted average for twice the quantum potential $2Q$ for time from 0 to 100 kicks. (c) The sum of (a) and (b), which is a weighted average for twice the quantum kinetic energy. (d) Resonant case with $\bar{k} = 4\pi$. The dots are the numerical data, the dash-dot curve is $(K^2/2)N^2$ for reference, and the solid line is a fitted quadratic curve. 85

B.1 Higher resolution on K for the Lyapunov exponent of the classical trajectories at Benettin *et al.* approach. $\Delta K = 0.002$ (a) $K = 7\pi$ region. Dashed line points to $K = 7\pi$ and solid lines illustrate region of Eq. (4.13) (b) $K = 8\pi$ region. Solid lines illustrate region of Eq. (4.12) while the dashed line is the right boundary of the second accelerator mode islands (c) $K = 9\pi$ region. Dashed line points to $K = 9\pi$ and solid lines illustrate region of Eq. (4.13) (d) $K = 10\pi$ region. Solid lines illustrate region of Eq. (4.12) and the dashed line is the right edge of the second accelerator mode islands. 103

B.2 Higher resolution on K for the Lyapunov exponent of the classical trajectories at Benettin *et al.* approach. $\Delta K = 0.002$ (a) $K = 11\pi$ region. Dashed line points to $K = 11\pi$ and solid lines illustrate region of Eq. (4.13) (b) $K = 12\pi$ region. Solid lines illustrate region of Eq. (4.12) while the dashed line is the right boundary of the second accelerator mode islands (c) $K = 13\pi$ region. Dashed line points to $K = 13\pi$ and solid lines illustrate region of Eq. (4.13) (d) $K = 14\pi$ region. Solid lines illustrate region of Eq. (4.12) and the dashed line is the right edge of the second accelerator mode islands. 104

B.3 Higher resolution on K for the Lyapunov exponent of the classical trajectories at Benettin *et al.* approach. $\Delta K = 0.002$ $K = 15\pi$ region. Dashed line points to $K = 15\pi$ and solid lines illustrate region of Eq. (4.13) 105

C.1 Values of exponent $\beta(K)$ in Eq. (5.7) around nonlinear regions of anomalous diffusion for (a) $K_1 = 6.49$, (b) $K_2 = 12.65$, (c) $K_3 = 18.90$ and (d) $K_4 = 25.17$. The increment in K used for computation is $1/20$. 107

C.2 Values of exponent $\beta(K)$ in Eq. (5.7) around nonlinear regions of anomalous diffusion for (a) $K_5 = 31.50$, (b) $K_6 = 37.79$, (c) $K_7 = 44.01$ and (d) $K_8 = 50.28$. The increment in K used for computation is $1/20$. 108

C.3 Values of exponent $\beta(K)$ in Eq. (5.7) around nonlinear regions of anomalous diffusion for (a) $K_9 = 56.56$, (b) $K_{10} = 62.85$, (c) $K_{11} = 69.13$ and (d) $K_{12} = 75.44$. The increment in K used for computation is $1/80$. 109

C.4 Values of exponent $\beta(K)$ in Eq. (5.7) around nonlinear regions of anomalous diffusion for (a) $K_{13} = 81.69$, (b) $K_{14} = 88.00$, and (c) $K_{15} = 94.25$. The increment in K used for computation is $1/80$. 110

C.5 Values of exponent $D(K)$ in Eq. (5.7) around nonlinear regions of anomalous diffusion for (a) $K_1 = 6.49$, (b) $K_2 = 12.65$, (c) $K_3 = 18.90$ and (d) $K_4 = 25.17$. The increment in K used for computation is $1/20$ for (a) while $1/40$ for (b), (c), and (d). . 111

C.6 Values of exponent $D(K)$ in Eq. (5.7) around nonlinear regions of anomalous diffusion for (a) $K_5 = 31.50$, (b) $K_6 = 37.79$, (c) $K_7 = 44.01$ and (d) $K_8 = 50.28$. The increment in K used for computation is $1/80$. 112

C.7 Values of exponent $D(K)$ in Eq. (5.7) around nonlinear regions of anomalous diffusion for (a) $K_9 = 56.56$, (b) $K_{10} = 62.85$, (c) $K_{11} = 69.13$ and (d) $K_{12} = 75.44$. The increment in K used for computation is $1/80$. 113

C.8 Values of exponent $D(K)$ in Eq. (5.7) around nonlinear regions of anomalous diffusion for (a) $K_{13} = 81.69$, (b) $K_{14} = 88.00$, and (c) $K_{15} = 94.25$. The increment in K used for computation is $1/80$. 114

D.1 Higher resolution on Lyapunov exponent of the Bohmian trajectories at Benettin *et al.* approach respecting to K. $\Delta K = 0.002$ (a) $K = 5\pi$ region, (b) $K = 6\pi$ region, (c) $K = 7\pi$ region (d) $K = 8\pi$ region. 116

D.2 Higher resolution on Lyapunov exponent of the Bohmian trajectories at Benettin *et al.* approach respecting to K. $\Delta K = 0.002$ (a) $K = 9\pi$ region, (b) $K = 10\pi$ region, (c) $K = 11\pi$ region (d) $K = 12\pi$ region. 117

D.3 Higher resolution on Lyapunov exponent of the Bohmian trajectories at Benettin *et al.* approach respecting to K. $\Delta K = 0.002$ (a) $K = 13\pi$ region, (b) $K = 14\pi$ region, (c) $K = 15\pi$ region (d) $K = 16\pi$ region. 118

CHAPTER 1

INTRODUCTION

The original definition of classical chaos is a system with exponential sensitivity to initial conditions. However, In quantum mechanics because of the linear property of the Schrödinger equation, variation on initial condition of the wave function will result in no change in the correlation function, which will result in no chaos in quantum mechanics. Berry's correspondence theorem [1] says that all classical chaotic systems also have quantum chaos. Reference [2] calls quantum chaos the quantum mechanics of classically chaotic systems. Currently the study of quantum chaos is certainly going beyond this point. However, the field remains largely unsettled [3, 4].

The concept of chaos is strong sensitivity to initial conditions. For quantum chaos, a variation of the Hamiltonian can be introduced to test the stability of the quantum system to the Hamiltonian [5]. A correlation function of the unperturbed and perturbed is studied and a signature of quantum chaos is given [5]. Other criteria are also introduced [5, 6, 7, 8, 9]. Among these approaches to quantum chaos, only the de Broglie-Bohm approach [10, 11, 12] of quantum mechanics [6] is analogous to classical chaos.

Positive Lyapunov exponents or KS entropy is the signature of classical deterministic chaos, and this is also taken as the case for Bohmian trajectories [6, 13, 14]. The use of the trajectories of de Broglie-Bohm theory to quantum chaos is a break-through in the application of the theory.

de Broglie-Bohm theory is recognized as a casual interpretation of quantum mechanics, and is completely consistent with standard quantum mechanics.

Bohmian trajectories are used for the quantum chaos study in this dissertation. In many cases, analytical solutions for Lyapunov exponents, especially for Bohmian trajectories, are difficult to obtain. Numerical simulation and computation are necessary and have proved to be a very powerful method in our study.

The kicked rotor is called the standard model in classical mechanics [7, 15, 16, 17]. It is one of the typical examples of one dimensional Hamiltonian chaos. This model originally starts from a pendulum kicked by periodically kicked δ-force. It provides a testing ground for many theoretical ideas, such as chaos, momentum diffusion, and quantum to classical correspondence principle [18, 19, 20, 21, 22]. We select the kicked rotor as the theoretical model for our study throughout the dissertation.

Momentum diffusion study has its significance at quantum break down and quantum to classical limitation [23, 24, 25, 26]. With experimental realization of atom optics kicked rotor, the real experimental data can also be used for momentum diffusion [20, 27]. In this dissertation momentum diffusion of the kicked rotor for both classical and quantum cases is one of the main topics.

In addition to momentum diffusion, the Lyapunov exponent approach to chaos for both the classical and quantum kicked rotor is studied and new results are given.

Chapter 2 first gives mathematical expressions for Lyapunov exponents of both in the original form and then in the modified version of Benettin *et al.* for bounded systems. Then the basic

part of the de Broglie-Bohm quantum theory of motion is given, and applied to quantum Lyapunov exponents for Bohmian trajectories.

Chapter 3 has a short introduction to the kicked rotor model. Its connection to a simple pendulum and the modern realistic quantum model of the atom optics kicked rotor is given. The experimental set-up of the atom optics kicked rotor, the theoretical derivation of the Hamiltonian from the real model and the initial conditions are introduced. The classical map for the kicked rotor from the Hamiltonian and Hamilton's equations is derived. The derivation of the map in quantum mechanics is also presented.

Chapter 4 gives the new findings on the local Lyapunov exponent of the classical kicked rotor. Trajectory simulation from a numerical approach and an analytical study of the upper bound of the two adjacent trajectories are reported. The Lyapunov exponents as a function of the classical control parameter K are computed based on Benettin *et al.* approach [28]. Stability regions in the chaotic sea are discovered numerically and analyzed.

Chapter 5 reports the study of momentum diffusion of the classical kicked rotor. Fifteen anomalous diffusion regions are found for the control parameter K from 0 to 100. The numerical data for momentum diffusion is well fitted by a power law $D(K)N^{\beta(K)}$. The corresponding exponents $\beta(K)$ and coefficients $D(K)$ are obtained numerically. The relation of the regions to the classical accelerator mode islands is studied.

Chapter 6 reports the chaos study on quantum kicked rotor. The map of Bohmian trajectories is similar to the classical map at quantum resonance. It is derived first and then the Benettin *et al.*

approach for the Lyapunov exponent is applied. Quantum chaos is found for Bohmian trajectories from that approach. Stability regions in the chaotic sea with a period π are discovered numerically.

Chapter 7 reports our results for the quantum momentum diffusion of the kicked rotor in standard quantum mechanics. The comparison of the numerical results to that of experimental and analytical results is made and they are consistent.

Chapter 8 reports our results for the quantum momentum diffusion of the kicked rotor in the de Broglie-Bohm quantum mechanics approach. For correct momentum diffusion results, the quantum potential should be included as part of the kinetic energy instead of taking it as a potential energy.

Chapter 9 is the summary of the dissertation.

Appendix A gives mathematics details for some of the analytical approach in this dissertation.

Appendix B gives auxiliary figures of Chapter 4 for more numerical study of classical kicked rotor on stability regions in the chaotic sea for the Benettin *et al.* approach of Lyapunov exponents.

Appendix C gives auxiliary figures of Chapter 5 for more numerical study of the anomalous momentum diffusion regarding the exponents $\beta(K)$ and coefficients $D(K)$.

Appendix D gives auxiliary figures of Chapter 6 for more numerical study of quantum kicked rotor on stability regions in the chaotic sea for the Benettin *et al.* approach to Lyapunov exponents.

CHAPTER 2

DEFINITION OF CLASSICAL AND QUANTUM CHAOS

2.1 Classical Deterministic Chaos

The Lyapunov exponent is the measure of chaos for a classically chaotic system. If the Lyapunov exponent $\lambda > 0$, then the regime is chaotic where λ is [9, 14, 28, 29]

$$\lambda = \lim_{d(0)\to 0_{t\to\infty}} \frac{1}{t} ln[d(t)/d(0)] \tag{2.1}$$

where $d(t)$ is the separation distance at time t between two trajectories, $d(0)$ is the initial distance between the two trajectories, and λ is the Lyapunov exponent.

In many cases, analytical solutions of Eq. (2.1) are difficult to obtain so that numerical study is essential. Indeed, additional considerations are needed for the numerical study of the exponential departure of two trajectories and the double limit to obtain the Lyapunov exponent.

It is assumed that the distance between two trajectories grows exponentially by having positive Lyapunov exponent defined in Eq. (2.1). Mathematically we are looking for expression of $d(t)$ and $d(0)$ as $d(t) = d(0)e^{\lambda t}$, with λ a positive constant. For most cases this ideal behavior does not occur. As indicated in reference [30, 31], the function $d(t)$ turns out to be rather irregular and possible saturation of initial exponential separation occurs. To resolve this difficulty, Benettin *et al.* define the quantity $\lambda_N(\tau, x, d(0))$ as [28, 30, 31]

$$\lambda_N(\tau, x, d(0)) = \frac{1}{N}\sum_{i=1}^{N}\frac{1}{\tau} ln\frac{|d_i|}{|d(0)|} \tag{2.2}$$

Here, $d(0)$ is the initial small distance. d_i is the distance of the two trajectories at time τ thereafter. One trajectory is taking as the reference. Let's define them recursively. The reference trajectory takes the initial position x_0. Then $y_0 = x_0 + d(0)$, $x_i = M(\tau)x_{i-1}$, $y_i' = M(\tau)y_{i-1}$, $d_i = y_i' - x_i$ and $y_i = x_i + \frac{d_i}{|d_i|}d(0)$. $M(\tau)$ is the map of the point from initial to final in time τ. The summation actually gives the average of the section Lyapunov exponents in time τ.

Three conclusions were drawn in reference [30]: (i) "The limit $lim_{N\to\infty}\lambda_N(\tau, x, d(0)) = \lambda(\tau, x, d(0))$ seems to exist; (ii) $\lambda(\tau, x, d(0))$ is independent of τ. (iii) $\lambda(\tau, x, d(0))$ is independent of d(0)." However, no method is ideal [32].

2.2 Quantum Theory of Motion

In quantum mechanics, the wave function is the solution of Schrödinger equation.

$$i\hbar\frac{\partial\Psi}{\partial t} = (-\frac{\hbar^2}{2m}\nabla^2 + V)\Psi \tag{2.3}$$

where Ψ is the wave function, $\hbar$ is Planck's constant divided by 2π, V is the potential and m is the mass of the particle.

In order to introduce the trajectory concept into quantum mechanics, the de Broglie and Bohm expressed the wave function in polar form: [12]

$$\Psi = R\, e^{iS/\hbar} \tag{2.4}$$

Inserting Eq. (2.4) into Eq. (2.3) and separating real and imaginary parts, we obtain the following equations for the fields R and S. The real part gives [12]

$$\frac{\partial S}{\partial t} + \frac{(\nabla S)^2}{2m} + Q + V = 0 \tag{2.5}$$

where the quantum potential is defined as [12]

$$Q(\mathbf{x},t) = -\frac{\hbar^2}{2m}\frac{\nabla^2 R}{R} \tag{2.6}$$

The imaginary part has the form [12]

$$\frac{\partial R^2}{\partial t} + \nabla \cdot (\frac{R^2 \nabla S}{m}) = 0 \tag{2.7}$$

Comparing Eq. (2.5) with the classical Hamilton-Jacobi equation for the action, we see that it has the same form but with the additional term Q [12]

Recognizing ∇S as momentum and $\nabla S/m$ as the velocity, we see that Eq. (2.7) is the continuity equation relating the particle probability density $\rho = R^2$ and current density $\mathbf{j} = R^2 \nabla S/m$ [12].

From Eq. (2.5) and (2.7), in comparison with classical theory, de Broglie-Bohm made the basic postulates that follow [12]:

(1) “An individual physical system comprises a wave propagating in space and time together with a point particle that moves continuously under the guidance of the wave.”

(2) “The wave is mathematically described by $\Psi(\mathbf{x},t)$, a solution to Schrödinger’s wave equation.”

(3) “The particle motion is obtained as the solution $\mathbf{x}(t)$ to the equation

$$\dot{\mathbf{x}} = (1/m)\nabla S(\mathbf{x},t)\mid_{\mathbf{x}=\mathbf{x}(t)} \tag{2.8}$$

where S is the phase of Ψ. To solve this equation we have to specify the initial condition $\mathbf{x}(0) = \mathbf{x}_0$ while the initial velocity has already been defined. The initial position constitutes the only extra information introduced by the theory that is not contained in $\Psi(\mathbf{x},t)$. An ensemble of possible motions associated with the same wave is generated by varying $\mathbf{x}_0$.”

(4) The probability that a particle in the ensemble lies in an element of volume d^3x at x at time t is given by

$$R^2(\mathbf{x},t)d^3x \tag{2.9}$$

where $R^2 =\mid \Psi \mid^2$.

From the above postulates, the momentum of the particle is $\mathbf{p} = \nabla S$ and the velocity of the particle is $\mathbf{v} = (1/m)\nabla S$. By applying the operator ∇ to Eq. (2.5) and rearranging, the equation of motion has the same form as Newton’s second law. It is [12]

$$\frac{d}{dt}(m\dot{\mathbf{x}}) = -\nabla(V+Q)\mid_{\mathbf{x}=\mathbf{x}(t)} \tag{2.10}$$

where

$$d/dt = \partial/\partial t + \dot{\mathbf{x}}\cdot\nabla \tag{2.11}$$

or simply

$$m\ddot{\mathbf{x}} = -\nabla(V+Q)\mid_{\mathbf{x}=\mathbf{x}(t)} \tag{2.12}$$

We see that what is new in the quantum equation of motion is the quantum potential and consequently the quantum force in Newton's second law, a second order differential equation. However this equation is a formal derivation. It is pointed out in this dissertation that the quantum potential is actually part of the quantum kinetic energy, and therefore the quantum potential is a fictitious potential. The quantum force is also a fictitious force.

2.3 Quantum Lyapunov Exponent

Quantum chaos is a field largely unsettled. Classical chaos is defined as a system with exponential sensitivity to the initial conditions. Positive Lyapnov exponents are the signature of chaos in classical mechanics. We take this condition as a criterion for chaos in quantum systems with Bohmian trajectories [7, 13, 14]. Increasing attention is given to the de Broglie-Bohm approach

since its first application to quantum chaos [1, 5].

More generally, the distance in phase space for the Lyapnov exponents may be used in the definition of chaos. The Lyapunov exponent Λ can be defined as [14].

$$\Lambda = \lim_{d(0)\to 0_{t\to\infty}} \frac{1}{t} ln \frac{d(t)}{d(0)} \tag{2.13}$$

where $d(t)$ is the distance of the two trajectories in phase space at time t and $d(0)$ is at time $t = 0$. Mathematically $d(t)$ is

$$d(t) = \sqrt{\sum_i \{[x_{i2}(t) - x_{i1}(t)]^2 + [p_{i2}(t) - p_{i1}(t)]^2\}} \tag{2.14}$$

The largest number describes the asymptotic rate of separation. If Λ_{max} is positive, then the system is chaotic.

CHAPTER 3

THE KICKED ROTOR MODEL

3.1 Introduction

The kicked rotor, also called the standard map, is the prime model for the study of both classical and quantum chaos. The classical kicked rotor models a pendulum in the absence of a gravitational field that is kicked periodically by an external $\delta-$function force. It is an example of a one-dimensional Hamiltonian system that exhibits classical chaos.The Hamiltonian is composed of the kinetic energy term, which gives free evolution, and the time-dependent potential with the δ-kick, which is periodic with a strength that depends on the sine function of the coordinate.

In 1995 the quantum kicked rotor became available for experimental study. Moore *et al.* [33] reported for the first time on the "Atom Optics Realization of the Quantum δ-Kicked Rotor." Since then, much work has been done both experimentally and theoretically [20, 33, 34, 35, 36, 37, 38, 39, 40, 41]. The atom optics kicked rotor is actually a kicked particle. The momentum is the linear momentum of the atom and the coordinate is the position of the atom. The kick is not an exact $\delta-$ function, but a function of narrow width that approximates it. For the traditional kicked rotor the momentum is the angular momentum and the coordinate is the angle. The angular coordinate is periodic with period 2π.

The experimental realization of the kicked rotor enables the theory to be verified. The combination of theoretical and experimental work enables progress to be made in many aspects in the field such as chaos, momentum diffusion and quantum to classical correspondence.

This chapter gives a brief survey of the kicked rotor model.

3.2 Classical Kicked Rotor

3.2.1 Simple Pendulum Model

The oscillation of a pendulum is one of the oldest examples of nonlinear phenomena. The Hamiltonian for free oscillation of a pendulum is [16]

$$H(p,x) = \frac{p^2}{2M} - U_0 cosx \tag{3.1}$$

Where x is the angle of the pendulum displacement from the lower (stable) position of pendulum; $p = M\dot{x}$ stands for the pendulum angular momentum; $M = ml^2$ is the moment of inertia. The frequency of small oscillations ($\dot{x}$) is related to the amplitude of the potential energy U_0 by $\dot{x}^2 = U_0/M$.

3.2.2 Hamiltonian of Classical Kicked Rotor

Assume that the pendulum is kicked by periodic $\delta-$ kicks and that the potential part is replaced by the $\delta-$ kick function with period T. The Hamiltonian for the $\delta-$ kicked rotor is [16]

$$H(p,x) = \frac{p^2}{2M} + Kcosx \sum_{n=-\infty}^{\infty} \delta(t - nT) \tag{3.2}$$

This model of the classical kicked rotor is also called the standard model and is one examples of one-dimensional Hamiltonian chaos because it is time dependent.

The dimensionless form of the Hamiltonian is [16]

$$H(p,x) = \frac{p^2}{2} + Kcosx \sum_{n=-\infty}^{\infty} \delta(t - n) \tag{3.3}$$

The realistic model is shown in Fig. 3.1 (a). The simple pendulum has a force which is $-mgsinx$, where x is the angle from the vertical, so the potential of the pendulum is $-mgcosx$. We now assume that there is no gravity, but the pendulum is blown by a periodically varying $\delta-$ function wind as illustrated by Fig. 3.1 (b). This is one example of pendulum kicked by a "$\delta-$ kick force" (Discussion with Dr. M. O. Scully).

3.2.3 Mapping of the Classical Kicked Rotor

The mapping of the standard model is as following [16]

$$x_{n+1} = x_n + p_{n+1} \quad p_{n+1} = p_n + Ksin(x_n) \tag{3.4}$$

The momentum is injected by the $\delta-$ kick with strength $Ksin(x_n)$ at time $t = n$ and followed by free evolution for a unit time, where the dimensionless time is in units of time per period.

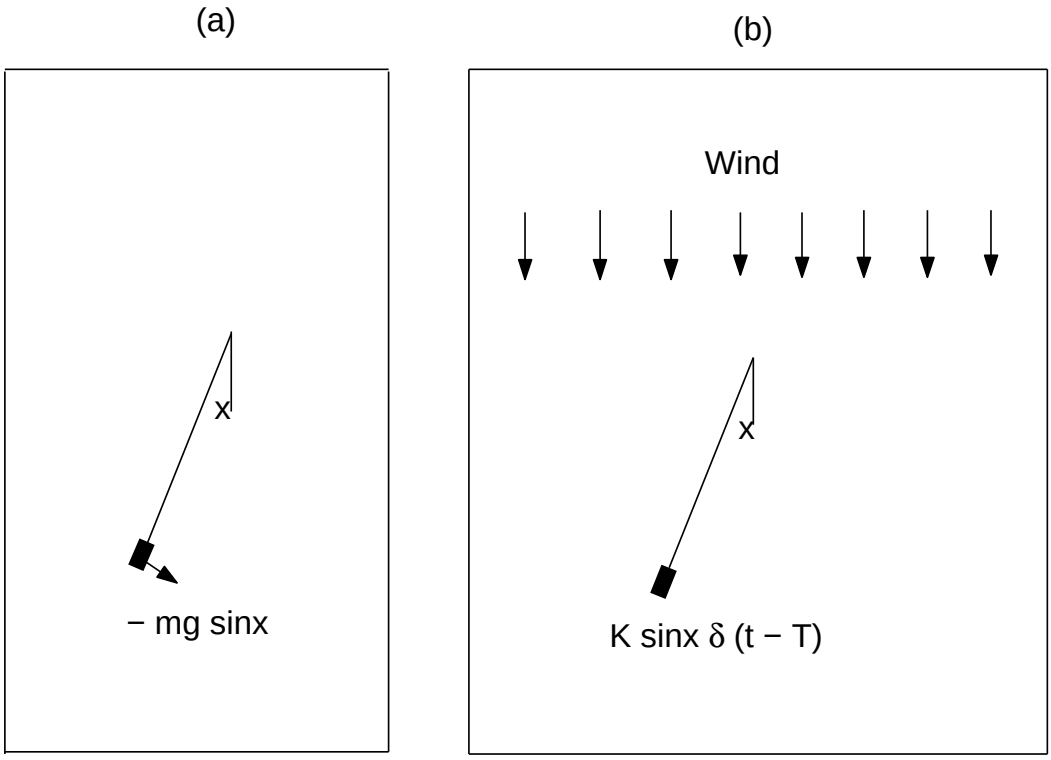

Figure 3.1: Illustration of classical kicked rotor with x the angle from vertical. (a) simple pendulum. (b) one example of classical kicked rotor.

3.3 Quantum Kicked Rotor

For the quantum kicked rotor, the Hamiltonian is the same as the classical, but the coordinate and momentum are operators. The dimensionless form of the Hamiltonian is [42]

$$H(\hat{p},\hat{x}) = \frac{\hat{p}^2}{2} + Kcos\hat{x}\sum_{n=-\infty}^{\infty}\delta(t-n) \tag{3.5}$$

The dimensionless Schrödinger equation is [42]

$$i\bar{h}\frac{\partial}{\partial t} \mid \psi\rangle = \hat{H} \mid \psi\rangle \tag{3.6}$$

where the scaled Planck's constant is $\bar{h} \equiv hk_0^2T/(2\pi M)$. Here h is the Planck's constant, k_0^2 is the wave number of the periodic potential function, T is the period of the kicks and M is the mass of the kicked rotor.

The time evolution of the particle can be viewed as a $\delta-$ kick followed by free evolution [42].

For integer values of t, the potential dominates the kinetic energy and we can neglect the latter [42]. The state $\mid \psi(t_n)\rangle$ immediately after a δ-function kick is related to the state $\mid \psi'(t_n)\rangle$ just before the kick by [42]

$$\mid \psi'(t_n)\rangle = \hat{U}_{kick}(\hat{x}) \mid \psi(t_n)\rangle \equiv exp[-i\frac{K}{k}V(\hat{x})] \mid \psi(t_n)\rangle \tag{3.7}$$

Between the two states of one time unit the state $\mid \psi'(t_n)\rangle$ evolves freely according to [42]

$$| \psi(t_{n+1})\rangle = \hat{U}_{free}(\hat{p}) \, | \psi'(t_n)\rangle \equiv exp[-i\frac{\hat{p}^2}{2k}] \, | \psi'(t_n) \tag{3.8}$$

Therefore, the complete time evolution over one period starting from the state at $t = t_n$ before the kick and ending at the state at $t = t_{n+1}$ before the kick is [42]

$$| \psi(t_{n+1})\rangle = \hat{U}_{free}(\hat{p})\hat{U}_{kick}(\hat{x}) \, | \psi(t_n)\rangle \tag{3.9}$$

and maps the state $| \psi(t_n)\rangle$ onto $| \psi(t_{n+1})\rangle$.

We define the time evolution operator as [42]

$$\hat{U}(\hat{x}, \hat{p}) \equiv \hat{U}_{free}(\hat{p})\hat{U}_{kick}(\hat{x}) \tag{3.10}$$

Then the quantum state $| \psi(t_n)\rangle$ after n kicks is obtained by applying the time evolution operator onto the initial state $| \psi(t_0)\rangle$ that is [42]

$$| \psi(t_n)\rangle = (\hat{U}(\hat{x}, \hat{p}))^n \, | \psi(t_0)\rangle \tag{3.11}$$

If we know the initial state of the wave function, we know the wave function at any time by iteration.

3.4 Atom Optics Kicked Rotor

Let us begin with a two-level atom with an energy difference equal to Planck's constant time a transition frequency ω_0 that interacts with a standing wave of near-resonant light. If the standing wave is composed of two counter propagating beams, each with field amplitude E_0 and wave number $k_L = 2\pi/\lambda_L = \omega_L/c$, then the atom is exposed to an electric field of the form $\vec{E}(x,t) = \hat{y}[E_0 cos(k_L x)e^{-i\omega_L t} + c.c.]$. The Hamiltonian of this atom in the rotating-wave approximation is given by [37]

$$H(x,p,t) = \frac{p^2}{2M} + \hbar\omega_0 \mid e\rangle\langle e \mid + \left[\mu E_0 cos(k_L x)e^{-i\omega_L t} \mid e\rangle\langle g \mid + H.c.\right] \tag{3.12}$$

Here $\mid g\rangle$ and $\mid e\rangle$ are the ground and excited internal states of the atoms, x and p are its center of mass position and momentum, M is its mass, and μ is the dipole moment coupling the internal states.

Using standard techniques, we obtain two coupled Schrödinger equations for the ground, $\psi_g(x,t)$, and excited, $\psi_e(x,t)$, state amplitude [37]

$$i\hbar\frac{\partial\psi_g(x,t)}{\partial t} = -\frac{\hbar^2}{2M}\frac{\partial^2}{\partial x^2}\psi_g(x,t) + \frac{\hbar\Omega}{2}cos(k_L x)\psi_e(x,t) \tag{3.13}$$

$$i\hbar\frac{\partial\psi_e(x,t)}{\partial t} = -\frac{\hbar^2}{2M}\frac{\partial^2}{\partial x^2}\psi_e(x,t) + \frac{\hbar\Omega}{2}cos(k_L x)\psi_g(x,t) + \hbar\delta_L\psi_e(x,t) \tag{3.14}$$

where $\Omega/2 \equiv \mu E_0/\hbar$ is the Rabi frequency of an atom interacting with just one of the light beams. The spontaneous emission from the excited state is neglected. This approximation is valid for the case of large detuning $\delta_L \equiv \omega_0 - \omega_L$ from the atomic resonance.

From Eq. (3.14), we have [37]

$$\psi_e(x,t) = -\frac{\Omega}{2\delta_L} cos(k_L x)\psi_g(x,t) + \frac{\hbar}{2M\delta_L}\frac{\partial^2}{\partial x^2}\psi_e(x,t) + \frac{i}{\delta_L}\frac{\partial \psi_e(x,t)}{\partial t} \tag{3.15}$$

The large detuning permits an adiabatic elimination of the excited state amplitude and results in the following equation for the ground state amplitude by substituting Eq. (3.15) into Eq. (3.13) [37]

$$i\hbar\frac{\partial \psi_g}{\partial t} = -\frac{\hbar^2}{2M}\frac{\partial^2}{\partial x^2}\psi_g - \frac{\hbar\Omega^2}{4\delta_L} cos^2(k_L x)\psi_g \tag{3.16}$$

The wave function of the “structureless” atom now obeys a Schrödinger equation with a one-dimensional Hamiltonian [37]

$$H(x,p,t) = \frac{p^2}{2M} - V_0 cos 2k_L x \tag{3.17}$$

Here $V_0 \equiv \hbar\Omega^2/8\delta_L$ since $cos^2(k_L x) \equiv (cos(2k_l x) + 1)/2$ and the constant part is dropped in the Hamiltonian without loss the generality.

The potential has a period of one-half the optical wavelength and the amplitude V_0 is [37]

$$V_0 = \frac{\hbar\Omega^2}{8\delta_L} \tag{3.18}$$

$$= \frac{2\hbar(\Gamma/2)^2}{3\delta_L}\frac{I}{I_{sat}} \tag{3.19}$$

Here Γ is the line width of the transition. I is the intensity of each of the beams comprising the standing wave and $I_{sat} \equiv \pi\hbar\omega_0\Gamma/3\lambda_L^2$ is the saturation intensity for the transition ($I_{sat} = 6mW/cm^2$ for the case of sodium atoms). Equation (3.19) was derived for a standing wave composed of two counter propagating beams of equal intensities. If the two beams are not perfectly matched, the potential amplitude are still given by this equation, with I taken as the geometric mean of the two intensities.

For the experimental realization of the atom optics kicked rotor, the standing waves are coming as pulses with period T and duration τ_p. The generic time-dependent potential for each laser pulse is

$$v(x,t) = V_0 F(t) cos(2k_L x) \tag{3.20}$$

Then the Hamiltonian now takes the form [37]

$$H(x,p,t) = \frac{p^2}{2M} + V_0 cos(2k_L x)\sum_{n=1}^{N} F(t-nT) \tag{3.21}$$

This is the Hamiltonian of the kicked rotor with finite duration of the pulses instead of having $\delta-$ kicks. The angle and angular momentum are replaced by position and momentum of atoms here. Strictly speaking, this system is one of kicked particles.

The dimensionless Hamiltonian is [34, 37]

$$H' = \frac{\rho^2}{2} + K cos\phi \sum_{n=1}^{N} f(\tau - n) \tag{3.22}$$

where ρ is the momentum of the atom in units of $2\hbar k_L/\bar{k}$, $K \equiv 8V_0\alpha T t_p \omega_r/\bar{h}$, $\bar{k} = 8\omega_r T$, $\tau = t/T$, and $\phi = 2k_L x$ is a measure of an atom's displacement along the standing wave axis.

A series of normalized pulses for the realistic case replaces the $\delta-$ functions, where [37]

$$f(\tau - n) = \frac{F(\tau T)}{\int_{-\infty}^{\infty} F(\tau T) d\tau} \tag{3.23}$$

The function $f(t)$ is defined as $f(t) = 1$ for $0 < t < \tau_p$ and zero otherwise. In the limit where $\tau_p \to 0$, we have the quantum $\delta-$ kicked rotor.

3.5 Experimental Realization of Atom Optics Kicked Rotor

The illustration of the core part of the experiment is given in Fig. (3.2). In the vacuum chamber, the atoms are rarified (very low pressure, below 10^{-10} torr [37]) so that collision between atoms is negligible inside the chamber. Six beams (three pairs of counter-propagating, circular polarized laser beams) are provided in three dimensions for the laser cooling of atoms. For trapping the

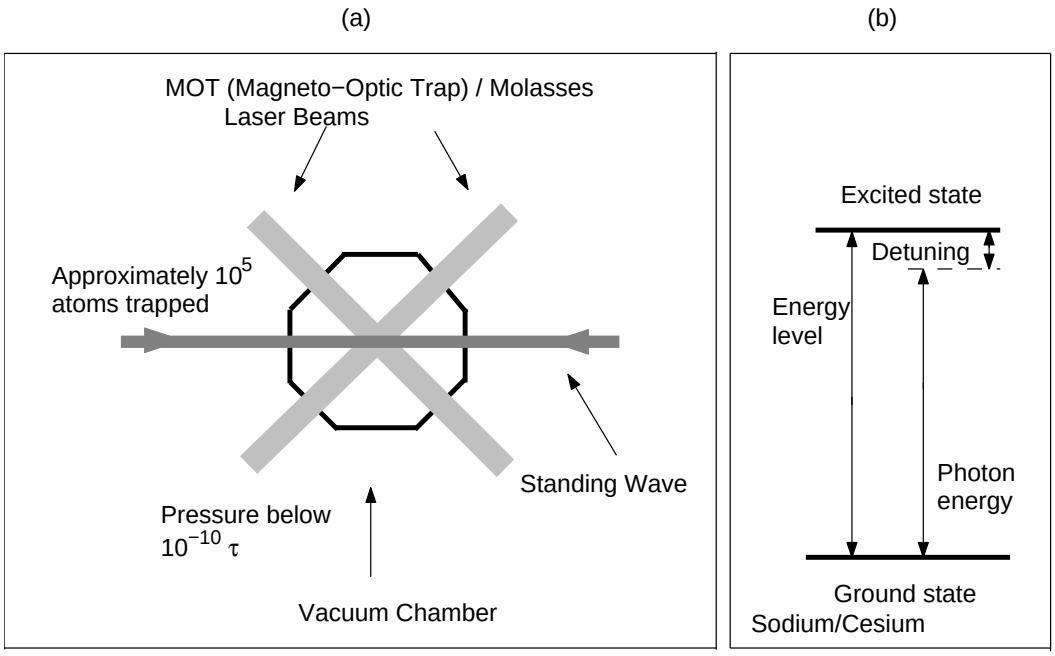

Figure 3.2: Illustration of experimental realization of atom optics kicked rotor. (a) is the core part of the experimental setup while (b) is the illustration of two level atom in standing wave potential.

atoms a magnetic field gradient of $10G/cm$ is provided by anti-Helmholtz coils. The extremely low pressure, temperature and the Magneto-Optic Trap (MOT) are for the purpose of preparing an initial condition that is collision free with near zero speed of the atoms. Before turning the kick fields on, the MOT should be turned off to set the atoms free to be kicked. Any residual magnetic fields after turning off the MOT are annuled by three-axis Helmholtz coils which surrounds the quartz envelop [33, 37]. The two beams propagating in opposite directions are turned on to generate the standing wave, which is the “kick field” acting on atoms.

Approximately 10^5 atoms are trapped in a cloud that has a root mean square (RMS) size of $0.15mm$, with an RMS momentum spread of $4.6\hbar k_L$ [37]. The laser beams for the standing wave

are turned on and off with period T. The pulse duration is t_p, which provides the potential of the kicked rotor. These beams are space filtered to be spatially uniform at the intersection region. The profile of the laser pulses is Gaussian distribution in time.

Usually sodium or cesium atom is used [33, 37, 44]. The momentum distribution of atoms is measured via the atom fluorescence detected by a CCD camera upon a fixed time duration. The entire sequence of the experiment is computer controlled.

CHAPTER 4

CLASSICAL CHAOS OF THE KICKED ROTOR

4.1 Introduction

We defined local Lyapunov exponent [1]. Numerical computation shows that for the kicked rotor it is constant for a duration that depends on the initial separation between two trajectories, but then decreases asymptotically as $O(t^{-1}lnt)$. This behavior is consistent with an upper bound that is determined analytically [22]. The Lyapunov exponent for bounded system should be calculated by the Benettin *et al.* method [28, 30]. The computation results of the Lyapunov exponent for the Benettin *et al.* approach for the classical kicked rotor shows the transition from non-chaotic to chaotic and gives stability regions in the chaotic sea which separates into two groups. The even multiples of π group corresponds to accelerator modes, while the odd multiples of π group corresponds to oscillator modes [43].

The classical kicked rotor or "standard map" or Chirikov-Taylor map [16] is often used to test techniques and methods in nonlinear analysis [28, 29, 45, 46], since it is a simple model that exhibits complex behavior. This behavior includes both chaotic and nonchaotic regimes. The characterization of classical chaos is the strong sensitivity to initial conditions [9, 28, 45, 46]. If two adjacent trajectories with initial values very close to each other depart exponentially in time, the position of

[1] Majority part of Section 4.1, Section 4.2 - 4.4, majority part of Section 4.6 and Figures 4.1 - 4.4 are reproduced with the permission of ELSEVIER (rights retained for author) from paper [22]

a particle cannot be reliably calculated after a sufficiently long time because of the uncertainty in the initial position. The coefficient of time in the exponential separation of adjacent trajectories is called the *global* Lyapunov exponent and is used as a criterion of chaos. Strictly speaking, the global Lyapunov exponent is defined only in the limit as the initial separation distance between the two trajectories goes to zero and time goes to infinity. Since mathematical limits cannot be attained by numerical methods, other definitions have been proposed for a *local* Lyapunov exponent to characterize chaos [30, 31, 47, 48, 49, 50].

In this chapter we define a *local* Lyapunov exponent that approaches a global Lyapunov in the limit as the separation distance approaches zero and time approaches infinity. Using our m-file programs in Matlab [51], we solve the classical kicked rotor in both chaotic and nonchaotic regimes. In the chaotic regime the local Lyapunov exponent is calculated as a function of separation distance and time. Our computations show that for sufficiently long times two adjacent trajectories in the chaotic regime depart polynomially, instead of exponentially. This behavior is confirmed analytically by showing that an upper bound to the departure of two adjacent trajectories is also a polynomial. The corresponding bound on the local Lyapunov exponent decreases asymptotically as $O(N^{-1}\ln N)$. However, in the beginning stage of time development exponential departure of two adjacent trajectories does occur and extends for a longer time as the initial separation distance decreases.

Chaotic regime is characterized by strong sensitivity to the initial conditions. If the two trajectories with initial very small distance depart exponentially, then the trajectory description of the

particle is no more making any sense, because there is always uncertainty in the initial position measurement. Mathematically, it is characterized by Lyapunov exponent.

If the Lyapunov exponent $\lambda > 0$, then the regime is chaotic where λ is expressed in Eq. (2.1)

For bounded systems, the quantity defined in Eq. (2.1) can be expected to saturate after a finite time [28]. Thus Benettin *et al.* [30] introduced a slightly different procedure for the Lyapunov exponent of those regimes. The quantity $\lambda_N(\tau, x, d(0))$ is defined as Eq. (2.2)

The limit of this λ_N at $N \to \infty$ is called the Lyapunov exponent for bounded systems [28]. If it is positive, the regime is chaotic and if it is less or equals to zero, the regime is non-chaotic. The Lyapunov exponent of the kicked rotor is computed from this approach and it matches the poincare phase space analysis of the kicked rotor in general picture [16]. However, lots more details and new discoveries are presented here.

4.2 Local Lyapunov Exponent

We use a local Lyapunov exponent because numerically only finite separation distances and times are possible. The trajectories have initial displacements $\mathbf{x}_1(0) = (x_1(0), p_1(0)) = (x_0, p_0)$ and $\mathbf{x}_2(0) = (x_2(0), p_2(0))$ in phase space, and their initial separation in phase space is $\mathbf{d}(0)$. We define a *local* Lyapunov exponent $L(x_0, d(0), t)$ as

$$L(\mathbf{x}_0, d(0), t) \equiv \frac{1}{t} \ln \left[\frac{d(t)}{d(0)} \right] \to \lambda \text{ as } d(0) \to 0,\ t \to \infty, \tag{4.1}$$

where $L(\mathbf{x}_0, d(0), t)$ depends in general on the initial displacement in phase space $\mathbf{x}_0 = \mathbf{x}_1(0) = (x_0, p_0)$, the initial separation distance $d(0) = |\mathbf{d}(0)|$, and time t. The modulus of the displacement in phase space at time t is $d(t) = |\ \mathbf{d}(t)|$. The double limit of the *local* Lyapunov exponent as the initial separation distance $d(0)$ approaches zero and time t approaches infinity is defined as the *global* Lyapunov exponent λ [28], which in general does not depend on the initial point $\mathbf{x}_0$ in phase space because of ergodicity[52, 53]. The value of the *global* Lyapunov exponent in Eq. (4.1) may depend on how the double limit is taken.

4.3 Numerical Calculations for Trajectories of the Kicked Rotor

The dynamics of the classical kicked rotor are given by the standard map

$$p(N+1) = p(N) + K\ \sin[x(N)], \quad x(N+1) = x(N) +\ p(N+1), \tag{4.2}$$

where N is the number of kicks. However, in general we measure time t in units of the period T of the kicks, so $t = N$ is a continuous variable. The context shows whether N is an integer or not. The only parameter in Eq. (4.2) $K = k\ T$, the product of the kick strength k and the period T, is called the control parameter. The displacement $x(N)$ is in radians, while the momentum $p(N)$ is in radians per unit time. For our calculations we chose $p_1(0) = p_2(0) = 0$, so the initial separation distance $d(0)$ in phase space is equal to the initial separation distance in coordinate space $x_2(0) - x_1(0) > 0$.

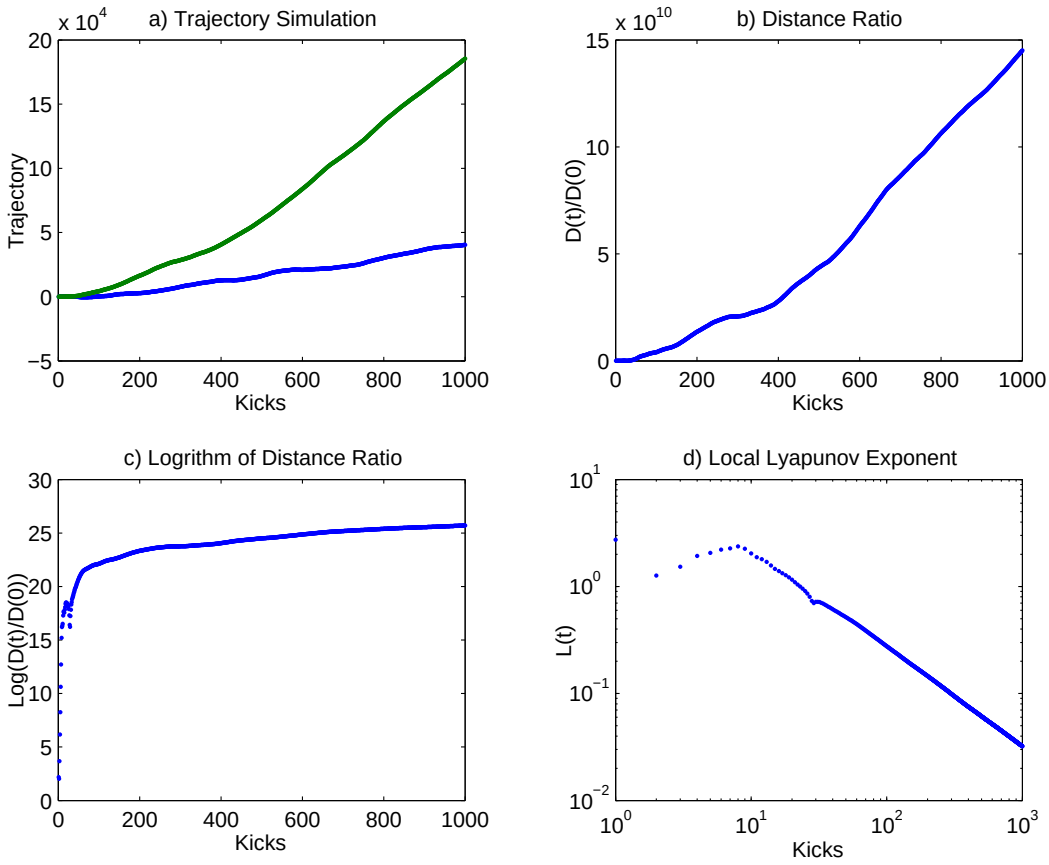

Figure 4.1: Trajectory simulation and Lyapunov exponent in the chaotic regime with $K = 10$ as a function of time N. (a) Simulation of two adjacent trajectories in coordinate space with initial separation distance $d(0) = 10^{-6}$ and $x_0 = 3$. (b) Ratio $d(N)/d(0)$ of distances in phase space as a function of time N. (c) Logarithm of $d(N)/d(0)$. (d) Corresponding local Lyapunov exponent L in Eq. (4.1).

Figure 4.1 shows the numerical solution of Eq. (4.2) in the chaotic regime with $K = 10$. The other parameters chosen are the initial displacement $x_0 = 3$, the initial separation distance $d(0) = 10^{-6}$, and the initial momenta $p_1(0) = p_2(0) = 0$. The number of kicks N (or time) goes from 0 to 1000. Subgraph (a) shows the displacement of the two trajectories in coordinate space without restricting the displacement to be from 0 to 2π. The coordinate space separation of the two trajectories increases with time, but not exponentially. Subgraph (b) shows the phase space separation distance ratio $d(t)/d(0)$. Subgraph (c) is the logarithm of the separation distance ratio, $\ln[d(t)/d(0)]$ and Subgraph (d) shows the corresponding local Lyapunov exponent in Eq. (4.1). The local Lyapunov exponent in this loglog plot is obviously approaching zero as the time or number of kicks increases beyond about 10.

Figure 4.2 studies the dependence of the local Lyapunov exponent on the initial separation distance $d(0)$ as the separation distance is reduced. The values of the separation distances are $d(0) = 10^{-6}, 10^{-8}, 10^{-10}$, and 10^{-12} for $x_0 = 3$. For a global Lyapunov exponent to exist, Eq. (4.1) shows that the local Lyapunov exponent must approach a constant in the double limit as $d(0) \to 0$ and time $N \to \infty$. We see in Fig. 4.2 that the local Lyapunov exponent is essentially constant in a plateau region that widens as $d(0)$ is reduced. For sufficiently large times, however, all the curves show an asymptotic approach to zero. An upper bound to the local Lyapunov exponents is $20N^{-1}\ln N$, the dotted line in Fig. 4.2. According to our analysis in Sec. 4.4 all the curves of local Lyapunov exponents for fixed $d(0)$ approach zero asymptotically faster than $O(N^{-1}\ln N)$. For the parameters and units chosen here the value of the local Lyapunov exponent is about 2.5.

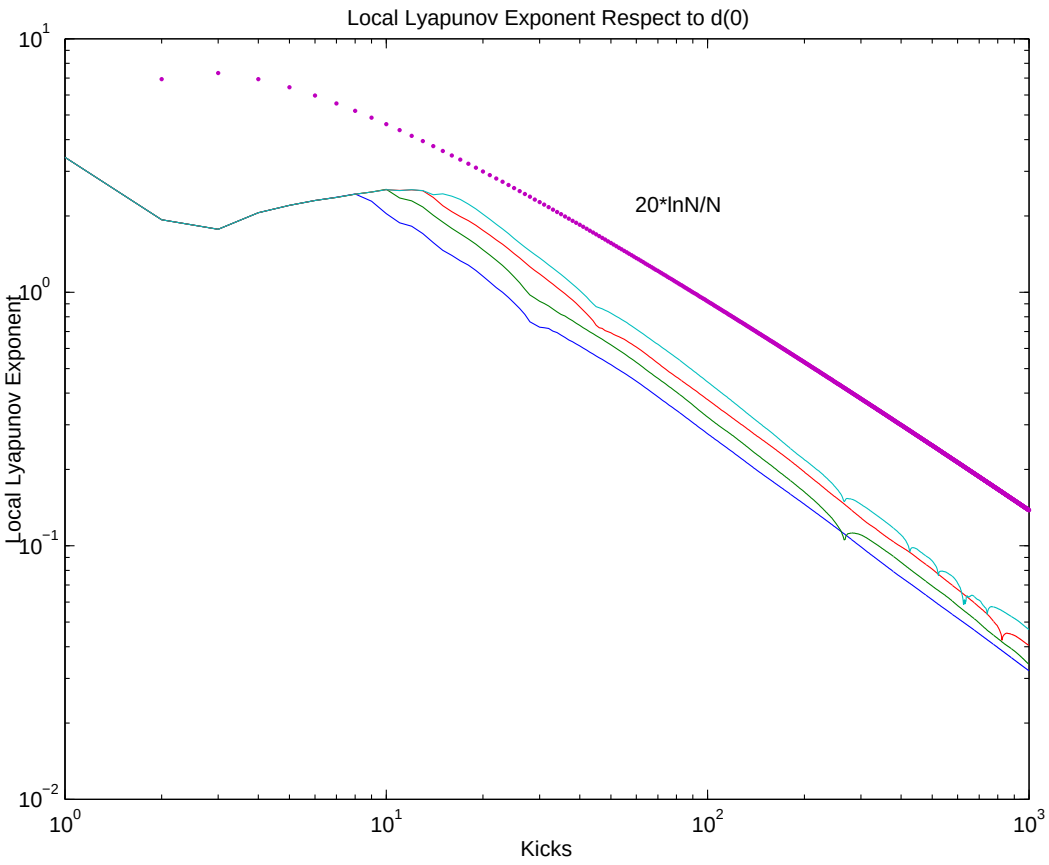

Figure 4.2: Local Lyapunov exponent L as a function of time N for $K = 10$, $x_0 = 3$ and different values of $d(0)$. From left to right $d(0) = 10^{-6}, 10^{-8}, 10^{-10}$, and 10^{-12}, respectively.

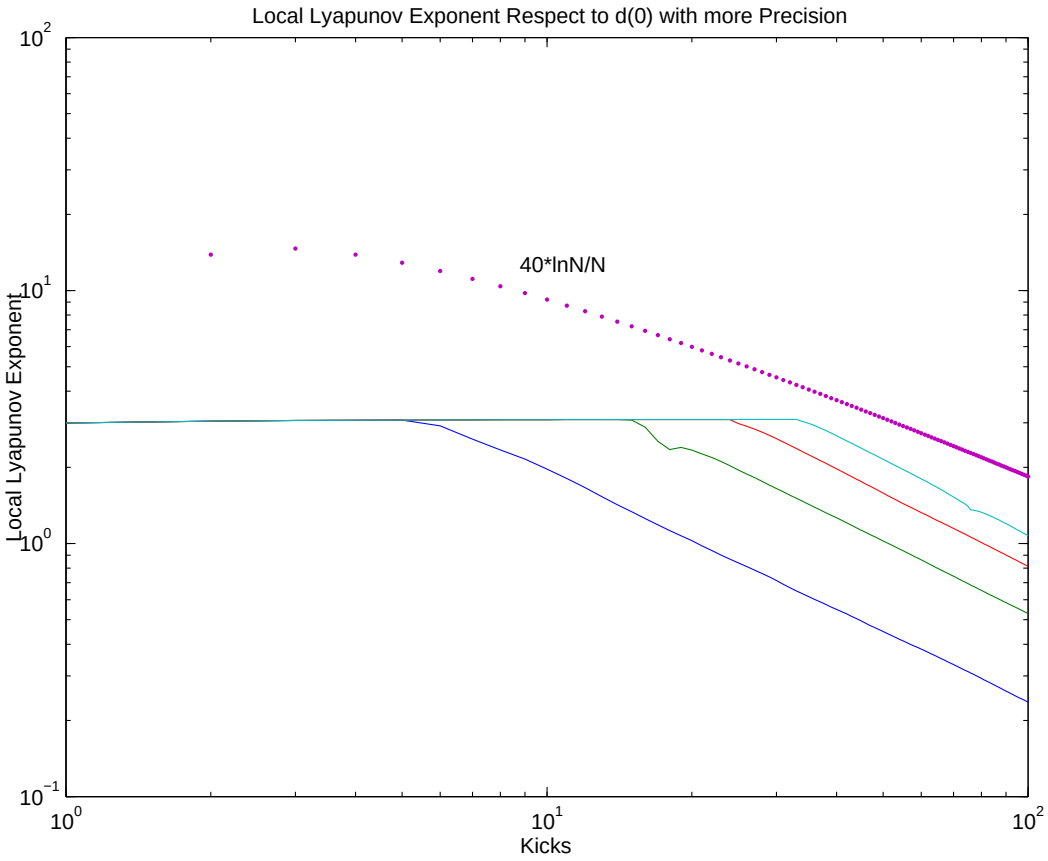

Figure 4.3: Local Lyapunov exponent L as a function of time N for $K = 10$, $x_0 = 0$ and different values of $d(0)$. From left to right $d(0) = 10^{-5}, 10^{-15}, 10^{-25}$, and 10^{-35}, respectively.

To investigate further the behavior of the local Lyapunov exponent on the separation distance $d(0)$, we used Matlab [51] variable precision arithmetic with 40 significant figures. In Fig. 4.3 the initial value of one trajectory is $x_1(0) = x_0 = 0$ and the other is $x_2(0) = d(0)$. The initial separation distances are taken to be $d(0) = 10^{-5}, 10^{-15}, 10^{-25}$ and 10^{-35}. The time or number of kick goes from 0 to 100. The plateau in Fig. 4.3 extends for longer times as $d(0)$ decreases. The dotted line in Fig. 4.3 is $40N^{-1}\ln N$, which is an upper bound to the local Lyapunov exponents. Here also, all the local Lyapunov exponents approach zero faster than $O(N^{-1}\ln N)$. For the parameters and units chosen here the value of the local Lyapunov exponent is about 3.

Figure 4.4 shows two trajectories for a parameter $K = 0.96$ with $x_0 = 3$ and $d(0) = 10^{-6}$ from a time N going from 0 to 20. On the scale used in Fig. 4.4 the two trajectories have such a small separation that they appear to overlap each other. The trajectories are bounded between about 3.0 and 3.3, and are somewhat periodic. This behavior continues for times as large as $N = 1000$. The line shown is only a guide for the eye. Because there is no significant separation of the trajectories for the parameters chosen, the system is nonchaotic in this case. This behavior is qualitatively different from the trajectories in Fig. 4.1 for $K = 10$ in the chaotic regime. In the chaotic regime the trajectories and their separation are constantly increasing, while in the nonchaotic regime the trajectories are confined to a very narrow region with little separation.

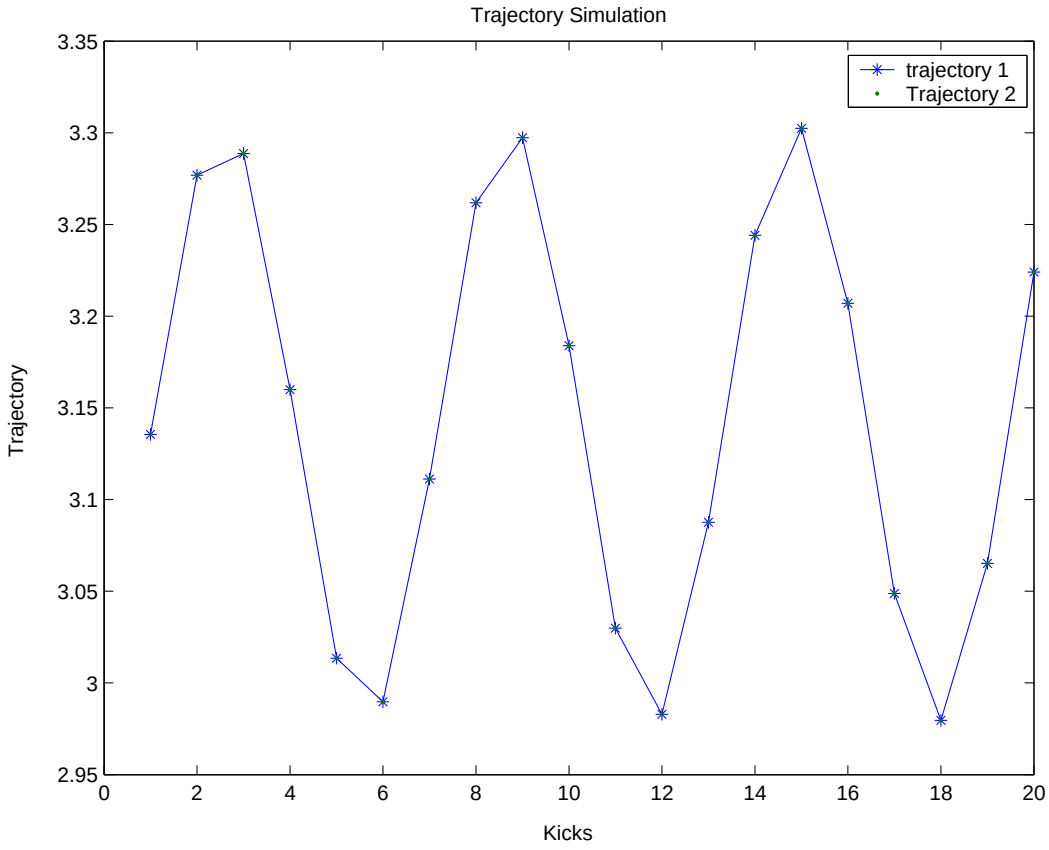

Figure 4.4: Trajectory simulation in the nonchaotic regime for $K = 0.96, x_0 = 3$ and $d(0) = 10^{-6}$. On the scale shown the two trajectories overlap each other. The dashed line is only a guide for the eye.

4.4 Upper Bound for Local Lyapunov Exponents

From the map in Eq. (4.2) we can analytically obtain an upper bound for the local Lyapunov exponents for fixed values of $d(0)$. This "worst case scenario" for their asymptotic behavior substantiates the numerical calculations in Figs. 4.1, 4.2, and 4.3 for large times.

For the upper bound we consider two trajectories initially at $\mathbf{x}_1(0) = (\, x_1(0), p_1(0))$ and $\mathbf{x}_2(0) = (x_2(0), p_2(0))$, where $d(0)$ is the separation distance in phase space. Since the sine function in Eq. (4.2) is no less than -1, the momentum $p_1(1)$ satisfies the inequality

$$p_1(1) = p_1(0) + K\sin[x_1(0)] \geq p_1(0) - K. \tag{4.3}$$

Assuming that

$$p_1(N-1) \geq p_1(0) - (N-1)K, \tag{4.4}$$

we prove by mathematical induction that the momentum for the first trajectory satisfies the inequality

$$p_1(N) \geq p_1(0) - NK, \tag{4.5}$$

for all $N = 0, 1, 2....$

Since the sine function in Eq. (4.2) is no more than $+1$, we can also prove by mathematical

induction that the momentum for the second trajectory satisfies the inequality

$$p_2(N) \leq p_2(0) + NK, \tag{4.6}$$

for all $N = 0, 1, 2....$

Likewise we can also prove by mathematical induction from Eq. (4.2) that the coordinate $x_1(N)$ of the first trajectory satisfies the inequality

$$x_1(N) \geq x_1(0) + Np_1(0) - \frac{1}{2}N(N+1)K, \tag{4.7}$$

and that the coordinate $x_2(N)$ of the second trajectory satisfies the inequality

$$x_2(N) \leq x_2(0) + Np_2(0) + \frac{1}{2}N(N+1)K, \tag{4.8}$$

for all $N = 0, 1, 2....$ From Eqs. (4.5) - (4.8) an upper bound on the separation distance $d(N)$ in phase space after *N* kicks is

$$\begin{aligned} d(N) &\equiv \left\{ \left[x_2(N) - x_1(N)\right]^2 + \left[p_2(N) - p_1(N)\right]^2 \right\}^{1/2} \\ &\leq \left\{ \left[x_2(0) - x_1(0) + N(p_2(0) - p_1(0)) + N(N+1)K\right]^2 + \left[p_2(0) - p_1(0) + 2Nk\right]^2 \right\}^{1/2} \\ &\rightarrow KN^2 \text{ as } N \rightarrow \infty, \end{aligned} \tag{4.9}$$

so two trajectories initially very close in phase space depart asymptotically like $O(N^2)$. If $p_2(0) = p_1(0)$ the initial separation distance in phase space $d(0)$ is also the initial separation distance in coordinate space

$$d(0) \equiv \left\{ \left[x_2(0) - x_1(0)\right]^2 + \left[p_2(0) - p_1(0)\right]^2 \right\}^{1/2} = x_2(0) - x_1(0) > 0. \tag{4.10}$$

We have chosen the condition $p_2(0) = p_1(0) = 0$ for our calculations in this paper, but for the sake of generality have not made this choice in this section.

From Eq. (4.9) the local Lyapunov exponent in Eq. (4.1) for time N satisfies the inequality

$$\begin{aligned} & L(\mathbf{x}_0, d(0), N) \leq \frac{1}{2N} \times \\ & \ln \left\{ \frac{1}{d(0)^2} \{ [x_2(0) - x_1(0) + N(p_2(0) - p_1(0)) + N(N+1)K]^2 + [p_2(0) - p_1(0) + 2NK]^2 \} \right\} \\ \rightarrow \quad & 2N^{-1} \ln N \text{ as } N \rightarrow \infty, \end{aligned} \tag{4.11}$$

so asymptotically the local Lyapunov exponent is $O(N^{-1} \ln N)$. That is, it approaches zero no slower than a constant times $N^{-1} \ln N$ as the time N approaches infinity in agreement with our numerical results.

4.5 Lyapunov Exponent of the Kicked Rotor

Figure 4.5 gives the Lyaponov exponents corresponding to control parameter K. From the large profile, there are two regimes of the classical kicked rotor. The transition from non-chaotic to chaotic happens at about $K = 3.5$ to 4.0. However, non-chaotic still exists for $K > 4.0$. For $K > 4.0$, the non-chaotic regime repeats at period of π. Negative Lyapunov values are always reached for all those regions for some of the K values.

Originally from Chirikov [16], the Poincaré map of the kicked rotor gives control parameter described as follow [2, 46]:

1) "For $K = 0.2$, the motion is on invariant tori for most initial conditions."

2) "For $K = 0.9716$, the last invariant torus is just destroyed, and unlimited diffusion becomes possible."

3) "For $K = 5$, the phase space has become chaotic, apart from some surviving stable islands."

The Lyapunov exponents presented here in general match this description. However the Poincaré approach was just trying on few individual values of control parameter K. It just provided the big stages of evolution from non-chaotic to chaotic on K. Here, with scanning on K for the Lyapunov exponents, more details are revealed.

The simplest regular motion [16] of the kicked rotor are the fundamental accelerator mode islands for which $K \sin\theta = 2\pi l$, where l is any integer and θ is some angle between 0 and 2π. In this case, with $p_0 = 0$ and $x(n) = \theta$, modulo 2π, the particle repeats its angle at each kick. This condition combined with the stability condition of $-4 < K\cos\theta < 0$ [16] gives the width of the fundamental

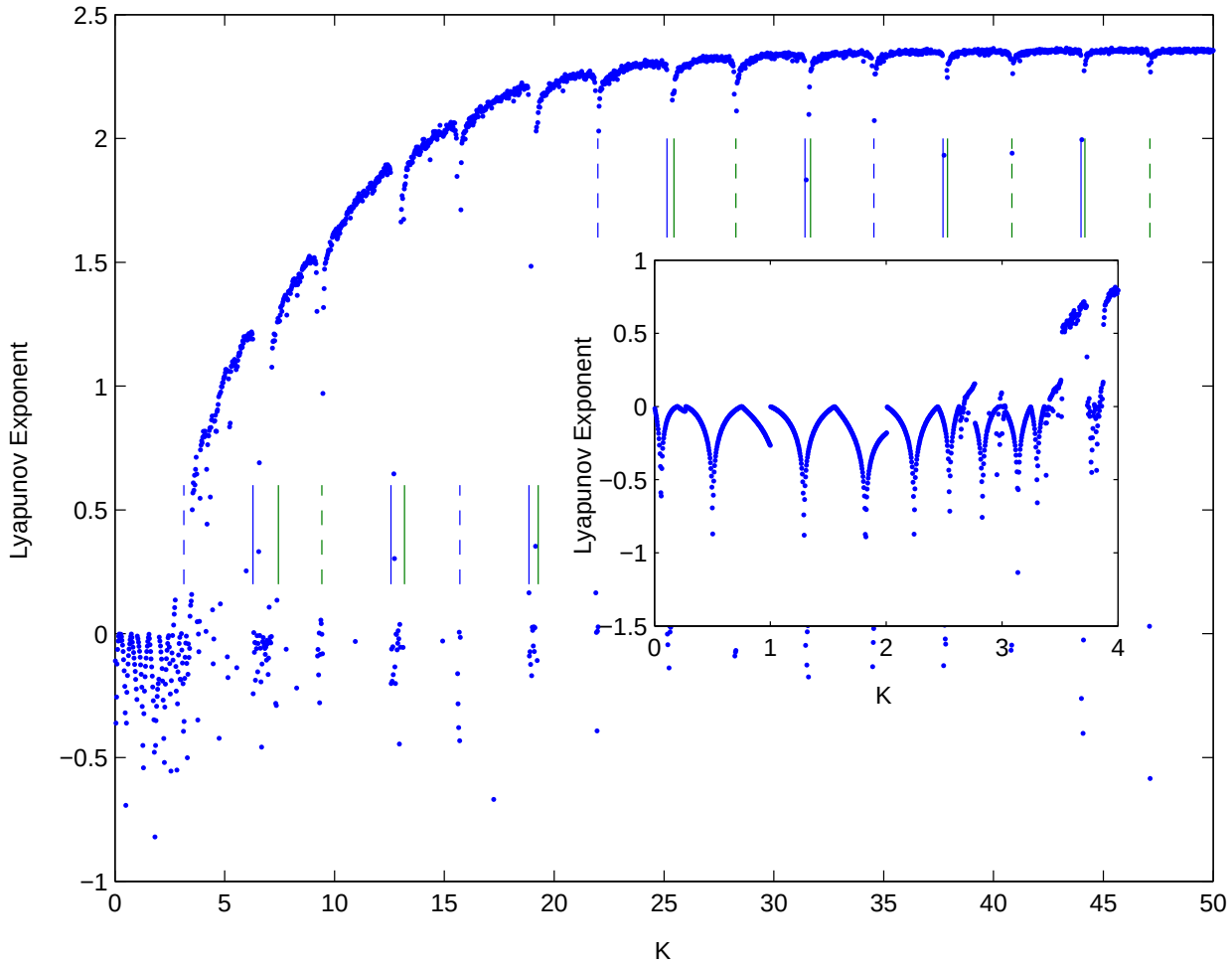

Figure 4.5: Lyapunov exponent of the classical trajectories from Benettin *et al.* approach with respect to K. 2000 points were evenly sampled on K. The inset shows the transition from the non-chaotic to chaotic regimes. 1000 points were sampled on K.

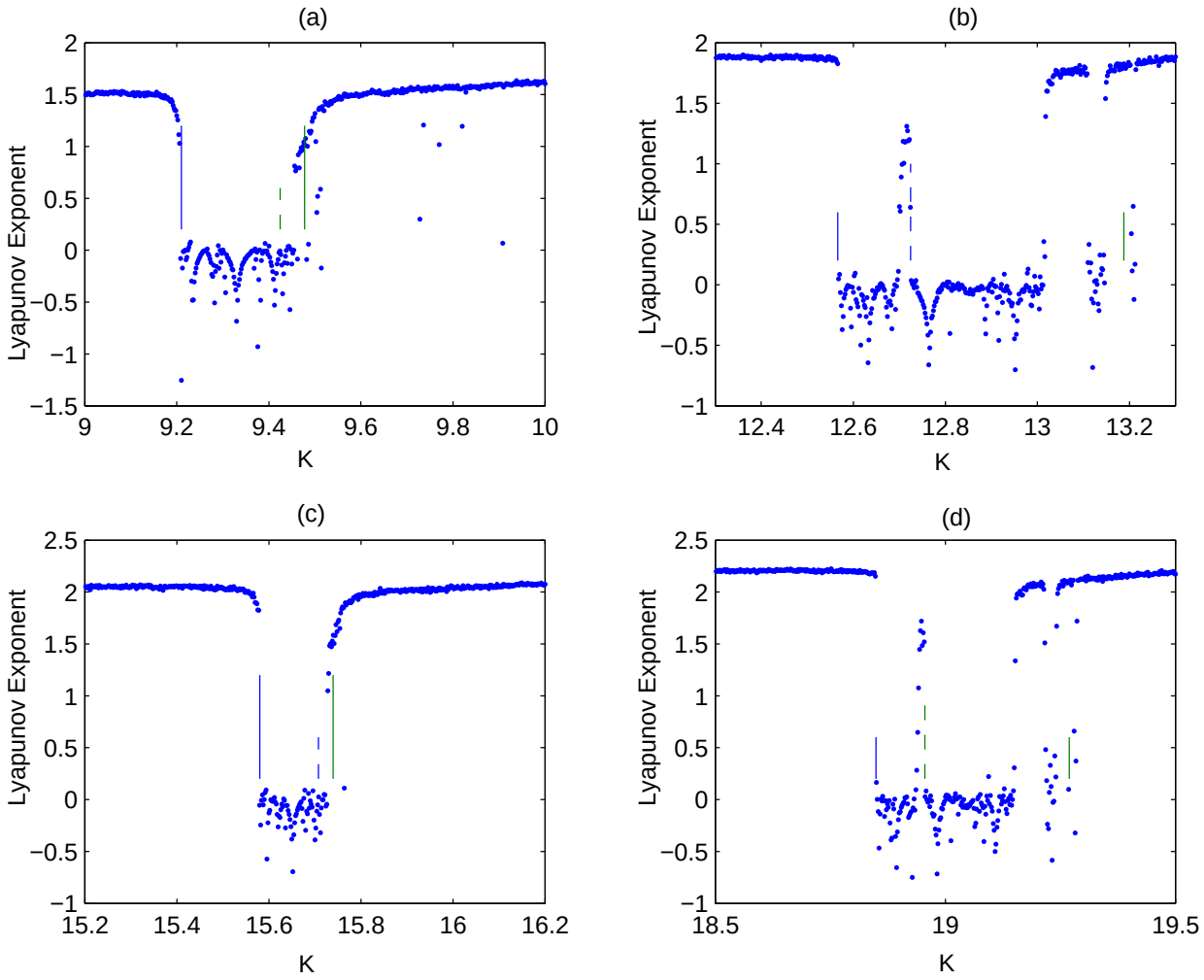

Figure 4.6: Higher resolution on K for the Lyapunov exponent of the classical trajectories at Benettin *et al.* approach. $\Delta K = 0.002$ (a) $K = 3\pi$ region. Dashed line points to $K = 3\pi$ and solid lines illustrate region of Eq. (4.13) (b) $K = 4\pi$ region. Solid lines illustrate region of Eq. (4.12) while the dashed line is the right boundary of the second accelerator mode islands(c) $K = 5\pi$ region. Dashed line points to $K = 5\pi$ and solid lines illustrate region of Eq. (4.13) (d) $K = 6\pi$ region. Solid lines illustrate region of Eq. (4.12) and the dashed line is the right edge of the second accelerator mode islands.

accelerator mode islands as

$$2\pi l < K < [(2\pi l)^2 + 4^2]^{1/2}. \tag{4.12}$$

In Fig. 4.6 (b) and (d) the pair of solid bars for even multiples of π group has stable regions whose width is essentially given by Eq. (4.12). We have also made additional calculations for other multiples of π from $l = 2$ to 16 that show similar behavior. The dashed line in these figures is the right side of a period two accelerator modes [16] whose width is given by $2\pi l < K < [(2\pi l)^2 + 2^2]^{1/2}$. This value is very close to the peaks in Fig. 4.6 (b) and (d) that may indicate the end of the period two accelerator mode.

The regions near the odd multiples of π are due to oscillator modes. We consider the condition $K\sin\theta = m\pi$ for odd m and find stable modes that oscillate. For an initial condition $p_0 = 0$, there are only two possibilities for the angle, which are $x(N) = \theta$ or $x(N) = \theta \pm \pi$. For $\theta < \pi$, we take the positive sign, but otherwise the negative sign. If we define $\theta' = \theta \pm \pi$, then $K\sin\theta' = -K\sin\theta$. Table 4.1 gives the evolution of the momentum and angle, which is an oscillating mode because it repeats after four kicks. We show by both numerical simulation and mathematical induction that this mode continues to be periodic.

n	0	1	2	3	4	5	6	...
p	0	$m\pi$	0	$-m\pi$	0	$m\pi$	0	...
x	θ	θ'	θ'	θ	θ	θ'	θ'	...

Table 4.1: Classical evolution of the momentum and angle for $m\pi$ group with m odd.

To investigate the stability of the oscillator mode we make a small deviation δ from $m\pi$ for odd m, so our new condition is $K\sin\theta = m\pi + \delta$. Iterating for some kicks with $p_0 = 0$ shows no instability. This mode still oscillates with a small deviation from $m\pi$ for m odd. From trajectory simulation we also have shown the stability of this oscillator mode [43]. The stability of these modes explains the finite width of the region around $m\pi$. An empirical formula for the width of the regions with an odd multiples m of π that fits the numerical simulation very well for seven regions is

$$[(m\pi)^2 - 2^2]^{1/2} < K < [(m\pi)^2 + 1]^{1/2}. \tag{4.13}$$

However, we have not been able to derive this formula from first principles.

To visualize the motion, trajectory simulations are presented here on both accelerator and oscillator modes. Fig. 4.7 (a) shows the trajectory simulation of the two adjacent trajectories at $K = 4\pi$, which is at the accelerator mode. Without perform modulo 2π, the trajectories glow 4π at each kick but the two trajectories stay together. Fig. 4.7 (b) takes $K = 9.2643$, which is $\sqrt{(3\pi)^2 - 3}$ within the region of 3π stability region. The motion is oscillating with two adjacent trajectories stay together. Fig. 4.7 (c) takes exactly $K = 3\pi$. We can see that the two trajectories stay together and the trajectories are oscillating. Fig. 4.7 (d) presents the trajectory simulation at the chaotic region with $K = 9.6$. We can see that the two trajectories are eventually separating substantially.

The classical kicked rotor is found to have chaos for $K = 3.5$ to 4 in agreement with Ref. [16]. For even multiples of π the classical kicked rotor has stable accelerator mode islands. For odd multiples of π we find stable oscillator modes. The details of the stable regions for the control parameter near

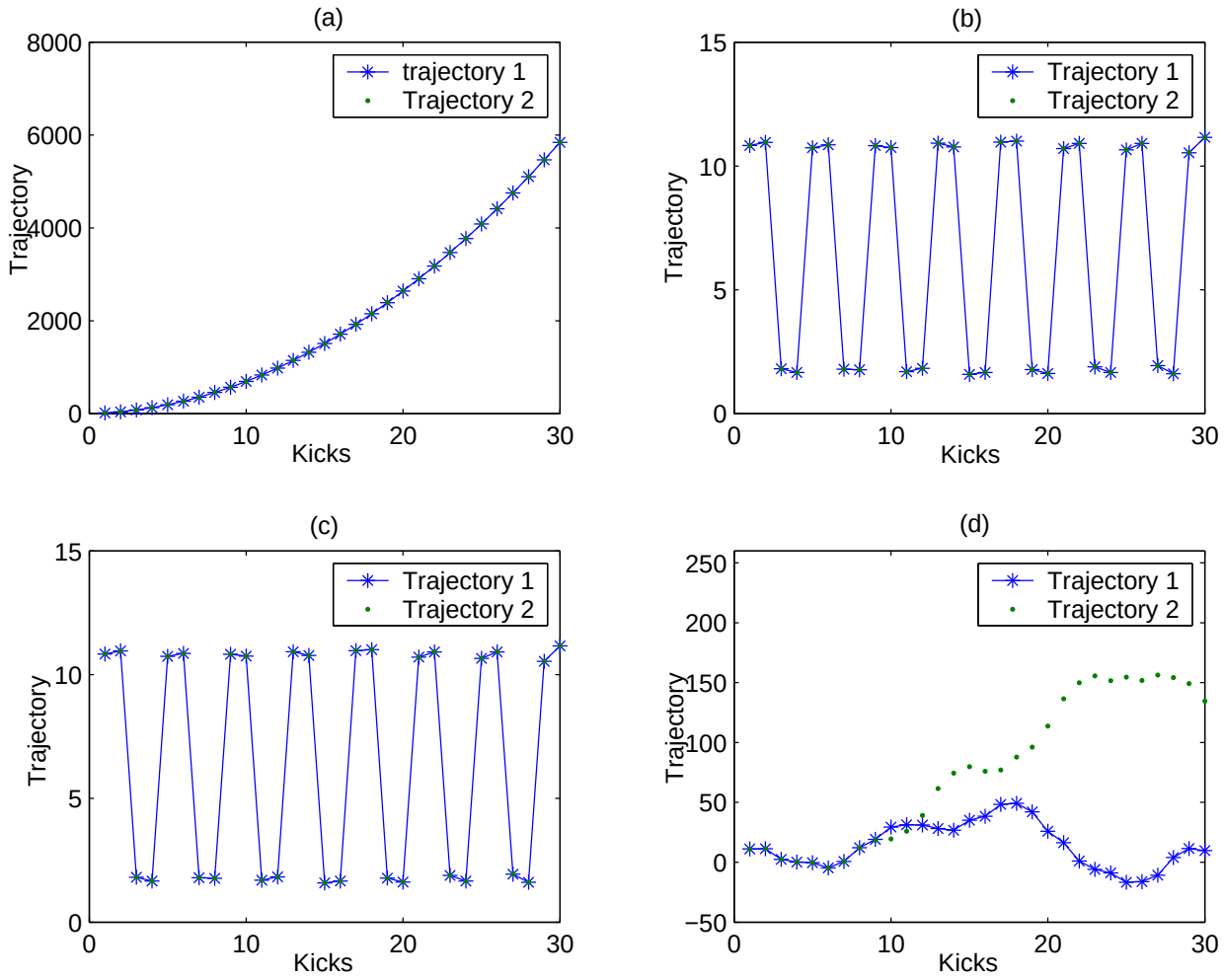

Figure 4.7: Trajectory simulation for the illustration of the chaotic and two types of non-chaotic. The initial distance for the two trajectories in each subgraph is $d_0 = 10^{-6}$, the initial momentum is $p_0 = 0$, and the initial position is $x_0 = \pi/2$. (a) $K = 4\pi$. (b) $K = 9.2643$. (c) $K = 3\pi$. (d) $K = 9.6$.

odd multiples of π remain to be explained.

4.6 Conclusion

In the chaotic region two adjacent trajectories separate exponentially for a duration that depends on the initial separation distance $d(0)$. The smaller the initial separation distance $d(0)$, the longer is the length of time that the local Lyapunov exponent is essentially constant. For sufficiently long times, however, we can see from Figs. 4.1, 4.2, and 4.3 that all curves decrease asymptotically more rapidly than $O(N^{-1}\ln N)$. This upper bound on the asymptotic behavior of the Lyapunov exponents is obtained analytically. In general, for any polynomial separation distance between adjacent trajectories, the corresponding local Lyapunov exponent decreases asymptotically as $O(N^{-1}\ln N)$.

In the non-chaotic regime, two adjacent trajectories remain extremely close to each other and are limited to a very narrow range of coordinates. This behavior is qualitatively different from the chaotic regime.

Stability regions repeated periodically in the chaotic sea with period π. The even multiples of π group is related to the accelerator modes while the odd multiples of π group is related to new oscillator modes. The onset for the classical non-chaotic to chaotic transition is about $K = 3.5$ to 4.

CHAPTER 5

MOMENTUM DIFFUSION IN THE CLASSICAL KICKED ROTOR

5.1 Introduction

The common expression of the momentum diffusion of the classical kicked rotor is $(K^2/2)N$, derived by neglecting the correlation between kicks, where K is the control parameter and N is the number of kicks [2, 28]. However this expression is only approximate and valid for normal momentum diffusion [46]. Anomalous momentum diffusion and a more precise description of normal momentum diffusion for the classical kicked rotor are studied and presented here. Numerical simulation for the classical kicked rotor is used to obtain the momentum diffusion over a region of the control parameter K from 0 to 100 that covers fifteen fundamental accelerator modes. The numerical data for momentum diffusion is well fit by a power law DN^{β} in the number of kicks N.

The kicked rotor or standard map plays an important role in the study of classical and quantum chaos. Even for this simple map analytical results are in general difficult to obtain and involve many approximations whose validity are sometimes difficult to assess. Numerical simulation is very helpful to go beyond analytical solutions and give guidance to experiments. Since the first atom optics realization of the quantum δ-kicked rotor experimentally, the study of momentum diffusion has been important in understanding the behavior of the kicked rotor [20, 33, 34, 35, 54].

In this chapter we study momentum diffusion $\left\langle (\Delta p)^2 \right\rangle$ in the classical kicked rotor as a function

of the control parameter K using numerical simulation. The well-known linear (in time) diffusion rate $K^2/2$ obtained by neglecting correlations [16, 28, 37] is generally not satisfied. Correlation effects are important and have been considered by Rechester and White [15, 46] and Meiss, *et al.* [55].

We consider the control parameter K over a range from 0 to 100 that covers fifteen fundamental accelerator mode regions [16]. Using a power law dependence DN^{β} for the anomalous momentum diffusion, we find the behavior of the exponent $\beta(K)$ and the coefficient $D(K)$ as a function of the control parameter over the corresponding accelerator island regions. The anomalous diffusion in these regions is slightly less than quadratic, except for a small dip. This behavior is consistent with our upper bound for momentum diffusion of $(K^2/2)N^2$. Outside these accelerator mode regions the diffusion is essentially linear, but the diffusion rate is not generally $K^2/2$. The coefficient $D(K)$ has three distinct sections within the fundamental accelerator mode regions, possibly due to higher period accelerator modes. Our numerical diffusion rates are computed using m-file in Matlab [51].

5.2 Equations for Momentum Diffusion

By mathematical induction from Eq. (4.2), we obtain

$$p(N) - p(0) = K \sum_{i=0}^{N-1} \sin[x(i)]. \tag{5.1}$$

When Eq. (5.1) is squared and averaged over the initial displacement, we obtain

$$\left\langle (\Delta p)^2 \right\rangle = \left\langle [p(N) - p(0)]^2 \right\rangle = K^2 \sum_{i=0}^{N-1} \left\langle \sin^2[x(i)] \right\rangle + K^2 \sum_{i \neq j} \left\langle \sin[x(i)] \sin[x(j)] \right\rangle . \qquad (5.2)$$

If the second term on the right-hand side of Eq. (5.2) is neglected because the spatial variables $x(i)$ at different times are assumed uncorrelated and the average of the first term is taken to be $1/2$, the momentum diffusion becomes $\left\langle (\Delta p)^2 \right\rangle_0 = (K^2/2)N$ [16, 28, 37]. Our numerical study shows that these assumptions are not in general valid and that correlation effects are usually very significant.

An upper bound to the momentum diffusion can be obtained by observing that the maximum value of all the averages on the right-hand side of Eq. (5.2) is $1/2$. Since there are altogether N^2 terms, an upper bound to the momentum diffusion is $\left\langle (\Delta p)^2 \right\rangle \leq (K^2/2)N^2$, which is quadratic in time (or kicks) N.

For a single trajectory, the value of $(\Delta p(N))^2$ can be quadratic in time N with a coefficient D that can exceed $K^2/2$. If we choose the initial values to be

$$K \sin[x(0)] = 2\pi n, \quad p(0) = 0, \qquad (5.3)$$

where *n* is an integer, then $x(N) = x(0)$ modulo 2π, then by mathematical induction the momentum at the N^{th} kick is

$$p(N) = N 2\pi n = NK \sin[x(0)]. \qquad (5.4)$$

For this class of trajectories we have

$$(\Delta p(N))^2 = \sin^2[x(0)]K^2N^2 \leq K^2N^2, \tag{5.5}$$

so for some individual trajectories the upper bound to $(\Delta p(N))^2$ is K^2N^2. References [16, 56] mention that the momentum grows quadratic in time only for those trajectories in accelerator modes. Since only a few points from 0 to 2π can satisfy Eq. (5.3), the average momentum diffusion is expected somewhat less than quadratic. Our numerical results that follow are consistent with this analysis.

5.3 Calculation of Momentum Diffusion

To obtain the momentum diffusion in Eq. (5.2) for a given K we solve Eq. (4.2) numerically for initial values $x(0)$ and $p(0) = 0$ and obtain the momentum difference $\Delta p = p(N) - p(0)$ at each value of time N from 0 to 100 kicks. To compute the average value of the momentum squared to get the momentum diffusion $\left\langle (\Delta p)^2 \right\rangle$, we have used 1000 values of $x(0)$ evenly spaced between 0 and 2π.

Figure 5.1 shows our calculated linear diffusion rate D_L divided by $K^2/2 = \left\langle (\Delta p)^2 \right\rangle_0 / N$, the diffusion rate in the absence of correlation effects [16, 28, 37], as a function of the control parameter K. The linear diffusion rate D_L was calculated by a least squares fit of $D_L N$ to the numerical data for $\left\langle (\Delta p)^2 \right\rangle$ for N from 0 to 100. Figure 5.1 covers the range of control parameter K between 0 to

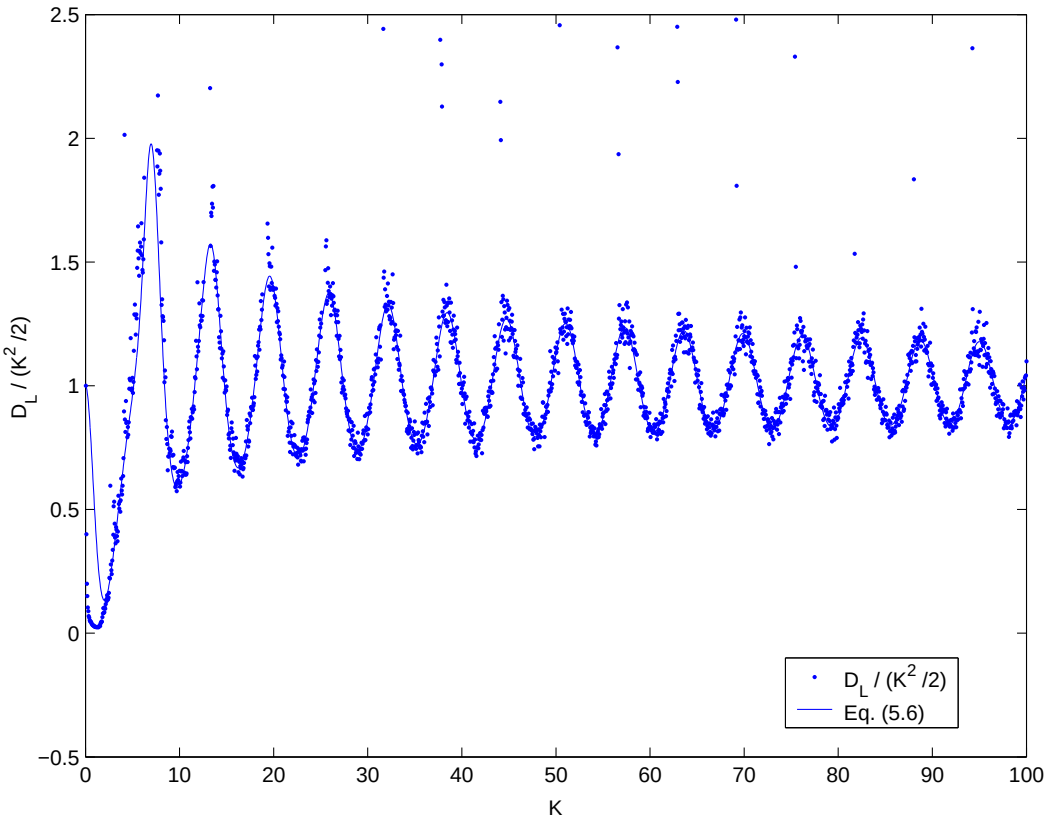

Figure 5.1: Linear diffusion rate D_L divided by $K^2/2$ for K from 0 to 100. The solid line is eq. (5.6).

100, respectively. Only for this general profile we used the rather coarse resolution of 2000 values of K evenly spaced between 0 and 100.

The solid curve in Fig. 5.1 is from Meiss, *et al*. [55],

$$\frac{D_L}{K^2/2} = \frac{1 - 2J_1^2(K) - J_2^2(K) + 2J_3^2(K)}{[1 + J_2(K)]^2}, \tag{5.6}$$

where J_n is a Bessel function of order n. It generally fits the numerical data well for the control parameter K from 2 to 100, except for (almost) periodic large deviations due to accelerator modes. This equation takes into account more correlation terms than the equation of Rechester and White [15] and extends the fit to the data for down to $K \approx 2$. Ichikawa, *et al.* [57] have made a careful study of the region $0.9716 \leq K \leq 6.2832$ and show that this formula fits the data qualitatively down to $K \approx 1.8$, but it does not take into account the resonances due to accelerator modes.

Rechester and White [15] in their Fig. 1, reproduced as Fig. 7.17 in Ott [46], show the momentum diffusion from $K = 0$ to 50. They state on the basis of their Eq. (21) that in the limit of "large" K the momentum diffusion ratio D_L to $K^2/2$ approaches unity. Equation (5.6) shows that for $K = 95$ the maximum linear diffusion ratio is about 18% greater than one. Even for $K = 100,000$ the ratio still deviates from unity by 0.5%. Figure 1 of Rechester and White [15] does not show the full extent of resonances near the maxima. Oscillations about unity in the linear diffusion ratio were first found by Chirikov [16].

5.4 Anomalous Momentum Diffusion

Figure 5.1 is obtained based on the assumption that momentum diffusion is linear and for K from 0 to 100 shows fifteen regions of anomalous momentum diffusion. Rather than linear, the momentum diffusion should be expressed more generally as

$$\left\langle (\Delta p)^2 \right\rangle = DN^{\beta} \text{ for } 1 \leq \beta(K) \leq 2, \tag{5.7}$$

for $D = D(K)$ and $1 \leq \beta = \beta(K) \leq 2$. We have used this relation to analyze the regions of anomalous momentum diffusion in Fig. 5.1. Accelerator islands are responsible for anomalous momentum diffusion, but we consider only the period one, step l islands, called the fundamental accelerator modes. The range of the control parameter K for the fundamental accelerator modes is given by the inequalities [16]

$$2\pi l \leq K \leq [(2\pi l)^2 + 4^2]^{1/2} \text{ for } l = 1, 2, \ldots \tag{5.8}$$

Figure 5.2 shows a plot of $\beta(K)$ in Eq. (5.7) *vs.* the control parameter K for four typical resonance regions with $l = 1, 4, 8$, and 12. We see that in these cases and also in all the others there are essentially two regimes - a linear regime outside of the resonance region and an approximately quadratic regime with a dip at about the center inside each resonance region. The profile of $\beta(K)$ is almost a step function for all peaks. For this figure and in all the other cases we used 10^4 values of $x(0)$ evenly space between 0 to 2π. The two vertical solid lines in each of the subgraphs of Fig. 5.2

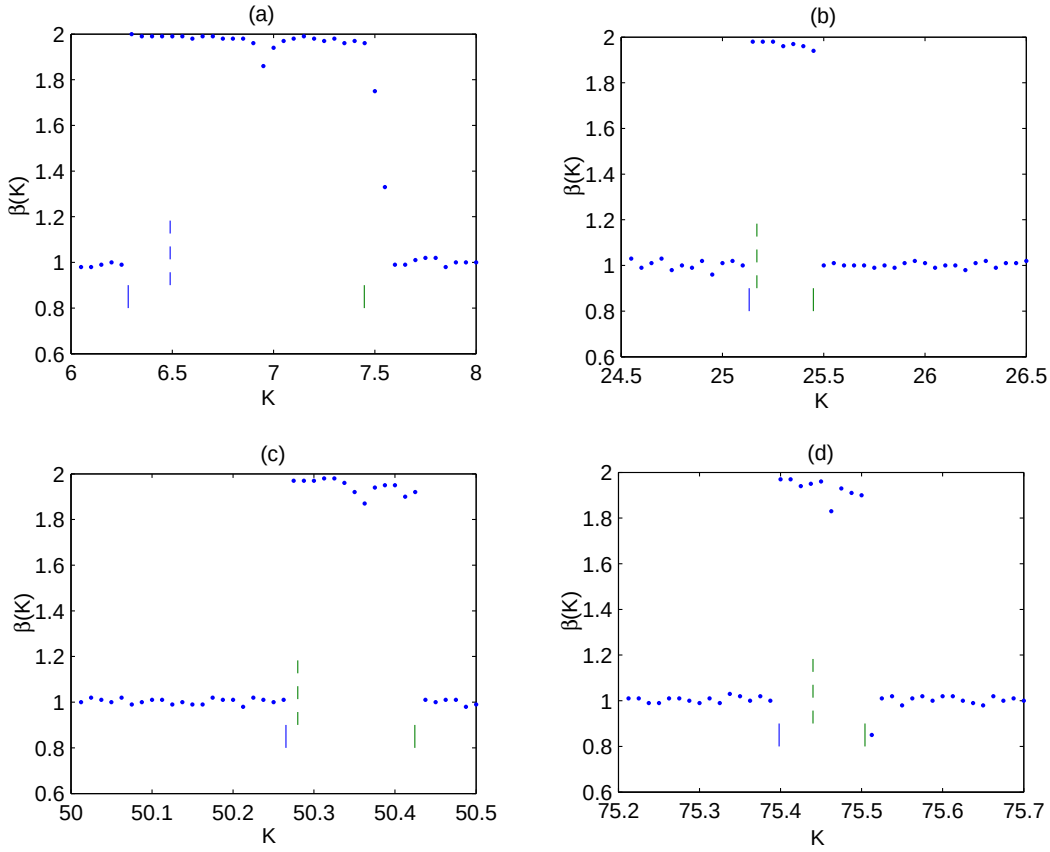

Figure 5.2: Values of exponent $\beta(K)$ in Eq. (5.7) around nonlinear regions of anomalous diffusion for (a) $K_1 = 6.49$, (b) $K_4 = 25.17$, (c) $K_8 = 50.28$ and (d) $K_{12} = 75.44$. The increment in K used for computation is $1/20$ for (a) and (b), while it is $1/80$ for (c) and (d).

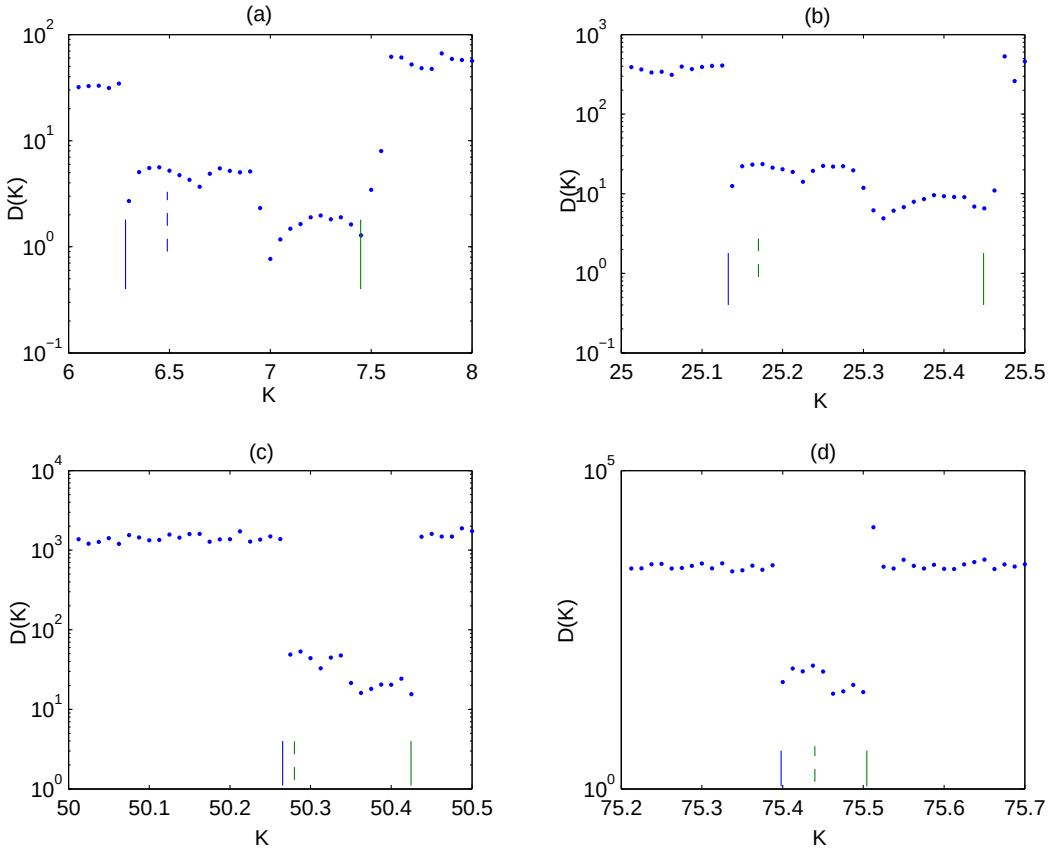

Figure 5.3: Values of coefficient $D(K)$ in Eq. (5.7) around nonlinear regions of diffusion for (a) $K_1 = 6.49$, (b) $K_4 = 25.17$, (c) $K_8 = 50.28$ and (d) $K_{12} = 75.44$. The increment in K used for computation is $1/20$ for (a), while it is $1/80$ for (b), (c) and (d).

show the range of control parameters in Eq. (5.8) for the fundamental accelerator modes $l = 1, 4, 8,$ and 12. The calculated regions of anomalous diffusion are in good agreement with these ranges. The dashed vertical line shows the control parameter K_l for the maximum value of the momentum diffusion $\left\langle (\Delta p)^2 \right\rangle$ in these regions.

For a control parameter $K = 6.9115$ Ishizaki, *et al.* [58] calculated the exponent of N to be $\beta \cong 4/3$. For this value of K we find $\beta = 1.89$ in the asymptotic region for N between 1000 and 5000 kicks with a fitting error of 0.88%. In this case we also used 10^5 initial values of $x(0)$ between 0 and 2π.

Figure 5.3 shows a plot of the coefficients $D(K)$ in Eq. (5.7) *vs*. the control parameter K for the same four typical resonance regions with $l = 1, 4, 8,$ and 12. Again, the two vertical solid lines in each of the subgraphs in Fig. 5.3 show the range of the control parameters in Eq. (5.8) for the fundamental accelerator modes $l = 1, 4, 8,$ and 12. The calculated regions of anomalous diffusion are in good agreement with these ranges. The dashed vertical line again shows the control parameter K_l for the maximum value of the momentum diffusion $\left\langle (\Delta p)^2 \right\rangle$ in these regions. Since the values of β are essentially constant in these regions, K_l occurs essentially at the maximum value of $D(K)$. For $D(K)$ there are also two regimes - a linear regime outside of the resonance region and an anomalous region inside. The anomalous region consists of three different sections similar to those found by Zasalavsky, *et al.* [59] that may perhaps be due to higher period accelerator modes [60].

The values of $\beta(K)$ in Fig. 5.2 are obtained by a least squares fit to the slope of a log-log plot of

the numerical data for $\left\langle (\Delta p)^2 \right\rangle$ *vs.* N in the asymptotic region from $N = 1000$ to 5000 kicks. Then the values of $D(K)$ in Fig. 5.3 are obtained from the original momentum diffusion data. In this way the two parameters were calculated independently. The resolution for the control parameter K was 10^{-2} to obtain three significant figure precision for both $\beta(K)$ and $D(K)$.

Mode l	1	2	3	4	5	6	7
K_l	6.49	12.65	18.90	25.17	31.50	37.79	44.01
$K_l - K_{l-1}$	–	6.16	6.25	6.27	6.33	6.29	6.22
Nonlinear region	6.30 7.60	12.55 13.20	18.80 19.25	25.10 25.45	31.40 31.65	37.65 37.90	43.95 44.15
Nonlinear width	1.30	0.65	0.45	0.35	0.25	0.25	0.20
β_l	1.98	1.98	1.99	1.99	1.99	1.99	1.95
D_l	5.73	12.00	16.33	21.56	24.42	29.91	52.19
Fitting error	0.26 %	0.28 %	0.084 %	0.15 %	0.11 %	0.18 %	0.22 %

Table 5.1: Properties of anomalous diffusion modes for K between 0 and 50.

Mode l	8	9	10	11	12	13	14	15
K_l	50.28	56.56	62.85	69.13	75.44	81.69	88.00	94.25
$K_l - K_{l-1}$	6.27	6.28	6.29	6.28	6.31	6.25	6.31	6.25
Nonlinear region	50.263 50.425	56.538 56.688	62.825 62.963	69.123 69.248	75.388 75.501	81.675 81.775	87.963 88.051	94.238 94.326
Nonlinear width	0.163	0.150	0.138	0.125	0.113	0.100	0.0875	0.0875
β_l	1.98	1.97	1.95	1.97	1.98	1.94	1.95	1.96
D_l	48.54	57.70	75.52	72.69	65.46	109.34	96.13	76.10
Fitting error	0.22 %	0.23 %	0.36 %	0.28 %	0.24 %	0.37 %	0.38 %	0.34 %

Table 5.2: Properties of anomalous diffusion modes for K between 50 and 100.

Tables 5.1 and 5.2 give the properties of the anomalous momentum regions. The first row gives the number of the fundamental mode from $l = 1$ to 15. The second row gives the control parameters

K_l corresponding to the maximum diffusion in that region of anomalous momentum diffusion. The third row gives the difference in control parameters between adjacent resonances $K_l - K_{l-1}$. These differences deviate from 2π by $\pm 2.\%$ or less. The fourth row gives the range of the nonlinear region, which is in good agreement with Eq. (5.8), and the fifth row gives the width of the region. The sixth and seventh rows gives the values of $\beta_l = \beta(K_l)$ and $D_l = D(K_l)$ for the values of the exponent and the coefficient, respectively, in Eq. (5.7) at the value of the control parameter K_l corresponding to the maximum momentum diffusion in accelerator mode region l. Finally, row eight gives the percent fitting error of Eq. (5.7) to the numerical data.

Figures 5.4 (a) and (b) are plots of the momentum diffusion *vs.* the time N in kicks for three values of K in the region near K_1 and near K_8, respectively. All the curves show nonlinear behavior. The least square fit of Eq. (5.7) to the numerical data in the asymptotic region from $N = 1000$ to 5000 kicks is shown for each case. The fitted curves are inside the numerical data curves.

5.5 Linear Momentum Diffusion

Figure 5.5 shows the numerical data for the momentum diffusion $\left\langle (\Delta p)^2 \right\rangle$ for the control parameter $K = 10$ in the linear region as a function of time (or kicks) from $N = 1$ to 5000 kicks. The solid line is the least squares fit of $D_L N$ to the numerical data for the momentum diffusion $\left\langle (\Delta p)^2 \right\rangle$ for N from 1 to 5000. The value obtained for the linear diffusion rate $D_L = 32.92$ deviates from the numerical data by an average of 0.32%. The momentum diffusion without correlations $\left\langle (\Delta p)^2 \right\rangle_0 = (K^2/2)N$ is shown as the dashed line. The value of $K^2/2$ deviates from D_L by 51.9%.

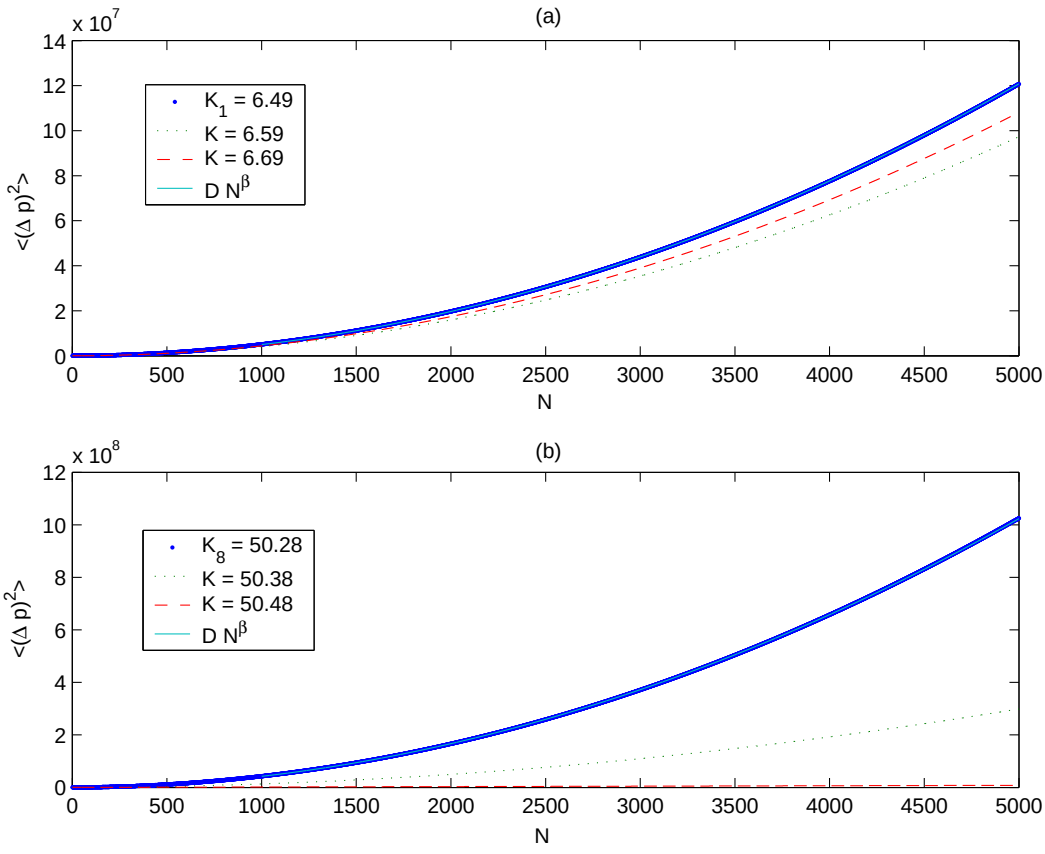

Figure 5.4: Momentum diffusion for several values of the control parameter K near modes 1 and 8 and the least squares fit to eq. (5.7) for K_1 and K_8 using data between kicks from 1000 to 5000.

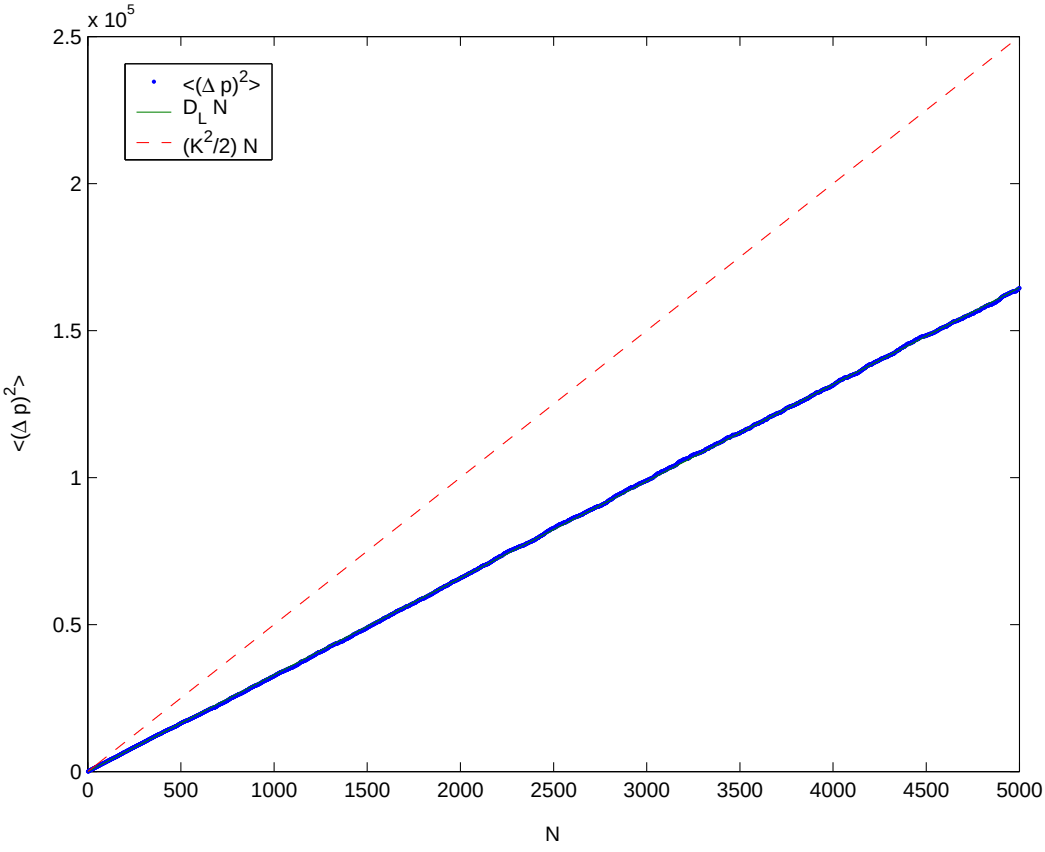

Figure 5.5: Linear fit to the diffusion for $K = 10$.

The values of D_L used in Fig. 5.1 are calculated in a similar way, but with N going from 1 to 1000 for the 2000 values of K used between 0 and 100.

For the sake of comparison, Ishizaki, *et al.* [58] calculated the diffusion rate for $K = 10.053$ and obtained $D_L \simeq (0.41) \times (2\pi)^2 \times (2) = 32.72$ in our units. For the same value of K we obtained $D_L = 32.63$ from a least squares fit with N going from 0 to $10,000$, which fit our numerical data to 0.97% error. Ishizaki, *et al.* [58] also calculated the diffusion rate for $K = 3.86$ and obtained $D_L \simeq (0.056) \times (2\pi)^2 \times (2) = 4.42$ in our units. For the same value of K we obtained $D_L = 3.73$ from a least squares fit with N again going from 0 to $10,000$, which fit our numerical data to 0.72% error.

5.6 Conclusion

We have made numerical computations for the momentum diffusion of the kicked rotor over a range of control parameter K from 0 to 100. In this range we find the fifteen regions of anomalous diffusion due to fundamental accelerator modes. These anomalous diffusion regions are further investigated to find their properties, such as width and time dependence. The anomalous momentum diffusion has a power law dependence with an exponent β in Fig. 5.2 that is a little less than quadratic in agreement with the upper bound of $(K^2/2)N^2$. The coefficient of the time dependence D in Fig. 5.3 shows three sections in the anomalous region, possibly due to higher period accelerator islands. The figures for $D(K)$ and $\beta(K)$ as functions of K in the anomalous diffusion regions near K_l for all l from 1 to 15 are given as auxiliary material in appendix C. Because of the complexity

of the equations involved, numerical simulation is essential for investigating momentum diffusion.

CHAPTER 6

QUANTUM CHAOS OF THE KICKED ROTOR:

DE BROGLIE-BOHM APPROACH

6.1 Introduction

Quantum chaos of the kicked rotor is found for the first time. The dependence of the Lyapunov exponents corresponding to the classical control parameter K for K from 0 to 50 is shown. Stability regions repeated with period π in the chaotic sea is similar to the classical case.

Classical deterministic chaos is characterized by strong sensitivity to the initial conditions of trajectories. For quantum chaos, directly applying this concept to standard quantum mechanics will lead to the result of no chaos in quantum mechanics because of the linear property of the Schrödinger equation [1]. However, the de Broglie-Bohm approach [10, 11, 12] of trajectories for quantum mechanics made it possible to study quantum chaos in analogy to classical mechanics. Positive quantum Lyapunov exponent is taken as the signature of quantum chaos [14].

For bounded systems, the Benettin *et al.* approach in Eq. (2.2) should be used for the Lyapunov exponents. This can be applied to Bohmian quantum trajectories of the kicked rotor since the angle is limited from 0 to 2π.

Results of the numerical computation using the Benettin *et al.* approach for the kicked rotor Lyapunov exponents and their dependence on the control parameter are given. The comparison

of the quantum to the classical Lyapunov exponents is also made. Both chaotic and non-chaotic regimes are found for the quantum kicked rotor.

Only trajectories at quantum resonance are studied since the quantum potential is zero at quantum resonance. The momentum diffusion for the average of the Bohmian trajectories is consistent to the traditional quantum mechanics [61].

6.2 Solution of the Schrödinger Equation

In terms of scaled variables [42] the dimensionless Hamiltonian of the kicked rotor is

$$\hat{H} \equiv \frac{1}{2}\hat{p}^2 + KV(\hat{x}) \sum_{n=-\infty}^{\infty} \delta(t-n), \tag{6.1}$$

where t is in units of the period T of the kicks, $V(\hat{x})$ is a periodic potential and K is the control (stochasticity) parameter. The displacement and canonical momentum operators are denoted by $\hat{x}$ and $\hat{p}$, respectively. The Schrödinger equation for the state vector $\psi(t)$ is

$$i\bar{k}\frac{\partial}{\partial t}\psi(t) = \hat{H}\psi(t), \tag{6.2}$$

where the dimensionless scaled Planck's constant $\bar{k} \equiv \hbar k_0^2 T/M$ is given in terms of Planck's constant $h = 2\pi\hbar$, the wave number k_0 of the periodic potential, the period of the kicks T, and the mass M of the kicked rotor. The displacement and canonical momentum satisfy canonical commutation relations with Planck's constant $\hbar$ replaced by the scaled Planck's constant $\bar{k}$.

Using the time evolution operator $\hat{U}$, the solution of the time-dependent Schrödinger equation for the state vector ψ at time t_N is [42]

$$\psi(t_N) = [\hat{U}(\hat{x},\hat{p})]^N \psi(t_0), \tag{6.3}$$

where $\psi(t_0)$ is the initial state vector. The time evolution operator for the kicked rotor is

$$\hat{U}(\hat{x},\hat{p}) = \exp\left[-i\frac{\hat{p}^2}{2k}\right]\exp\left[-ikV(\hat{x})\right], \tag{6.4}$$

where $k \equiv K/\overline{k}$. The last factor on the right-hand side of Eq. (6.4) gives the effect of the kick and the first factor gives free propagation between the kicks.

The state vector after the N^{th} kick can be expanded in the complete set of orthonormal momentum eigenstates $|l\rangle$ as

$$\psi(t_N) = \sum_{l=-\infty}^{\infty} a_l(t_N)\,|l\rangle\,, \tag{6.5}$$

where the coefficients $a_l(t_N)$ are determined from the Schrödinger equation. From Eq. (6.3) the state vector at time t_{N+1} is therefore

$$\psi(t_{N+1}) = \sum_{l=-\infty}^{\infty} a_l(t_N)\hat{U}(\hat{x},\hat{p})\,|l\rangle\,. \tag{6.6}$$

The expansion coefficients $a_m(t_{N+1})$ of the state vector $\psi(t_{N+1})$ after the $(N+1)^{th}$ kick can be

expressed in terms of the expansion coefficients of $a_l(t_N)$ by taking the inner product of Eq. (6.6) with $|m\rangle$,

$$a_m(t_{N+1}) = \exp[-im^2\bar{k}/2] \sum_{l=-\infty}^{\infty} a_l(t_N) W_{ml}, \tag{6.7}$$

where the matrix element is defined as $W_{ml} \equiv \langle m| \exp[-ikV(\hat{x})] |l\rangle$. From this recursion relation we can find the state vector at any time t_N if we know the initial state at time t_0.

We take the periodic potential to be $V(x) \equiv \cos x$ for numerical computation. From the generating function for Bessel functions, we have the formula

$$\exp[-ik\cos x] = \sum_{n=-\infty}^{\infty} (-i)^n J_n(k) \exp(-inx), \tag{6.8}$$

where J_n is the Bessel function of order n and $k \equiv K/\bar{k}$.

Substituting Eq. (6.8) into Eq. (6.7) and using the orthonormality of the momentum eigenfunctions, we obtain the recursion relation for the coefficients $a_m(t_{N+1})$

$$a_m(t_{N+1}) = \exp[-im^2\bar{k}/2] \sum_{l=-\infty}^{\infty} (-i)^{l-m} J_{l-m}(k) a_l(t_N) \tag{6.9}$$

6.3 Mapping of Bohmian Trajectories of the Kicked Rotor at Quantum Resonance

According to $\mathbf{p} = \nabla S$ [10, 11, 12] and using the solution of the wavefuction at expansion, the momentum and velocity of the trajectory can be expressed as

$$p(t) = Im[\bar{k}\frac{\nabla\psi(x,t)}{\psi(x,t)}]_{x=x(t)} \tag{6.10}$$

$$= Re[\frac{\sum_{-\infty}^{\infty} a_l(t) p_l exp(ilx)}{\sum_{-\infty}^{\infty} a_l(t) exp(ilx)}]_{x=x(t)} \tag{6.11}$$

where $p_l \equiv l\bar{k}$ is the momentum at state $\mid l\rangle$. This is the general expression of the momentum according to $\mathbf{p} = \nabla S$. Since the quantum potential is zero at quantum resonance, this expression is still fine at quantum resonance for the theory that the quantum potential is fictitious.

For the resonant case $\bar{k} = 4\pi n$, where $n = 1, 2, 3, ...$, the evolution operator $\exp\left[-i\hat{p}^2/2\bar{k}\right]$ in Eq. (6.4) for free propagation between kicks is unity when it acts on a momentum eigenstate $|m\rangle$ because $p_m = m\bar{k}$ [37, 42]. Therefore, by inserting the resolution of the identity N times between time evolution operators U in Eq. (6.3) and using the coordinate representation, we obtain the wave function

$$\psi(x, t_N) = \langle x \,|\psi(t_N)\rangle = \exp[-iNkV(x)]\psi(x, t_0), \tag{6.12}$$

where the time $t_N = N$.

From Eq. (6.12), with initial state of momentum eigenstate $\mid p_0\rangle$, we obtain

$$p(t_N) = p_0 + NKsin(x(t_{N-1})) \tag{6.13}$$

Since the kicked rotor model is $\delta-$ kick followed by a free evolution, the mapping of the Bohmian trajectories at quantum resonance is

$$p(t_{N+1}) = p_0 + (N+1)Ksin(x(t_N)), \quad x(t_{N+1}) = x(t_N) + p(t_{N+1}) \tag{6.14}$$

The momentum diffusion at quantum resonance is

$$< [p(t_N) - p_0]^2 >= \frac{K^2}{2} N^2 \tag{6.15}$$

which is faster than that of the classical.

6.4 Numerical Experiment of Bohmian Trajectories

For quantum kicked rotor, the angle has 2π period. The system can be considered as space limited from 0 to 2π so that Benettin *et al.* approach should be used for the Lyapunov exponent computation.

Figure 6.1 shows convergence of λ_N on N going to infinity. For numerical computation, it is sufficient for N to reach 2000 from Fig. 6.1. Four curves are provided for $K = 12.5$, 6.49, 2π and 0.55. For $K = 12.5$ and 6.49, λ_N converges to a positive value, which is the signature of a chaotic regime. For $K = 2\pi$, it converges to zero. And for $K = 0.55$, it converges to a negative value. These latter two are non-chaotic regimes.

For giving a general picture and showing the transition of the non-chaotic to chaotic of the

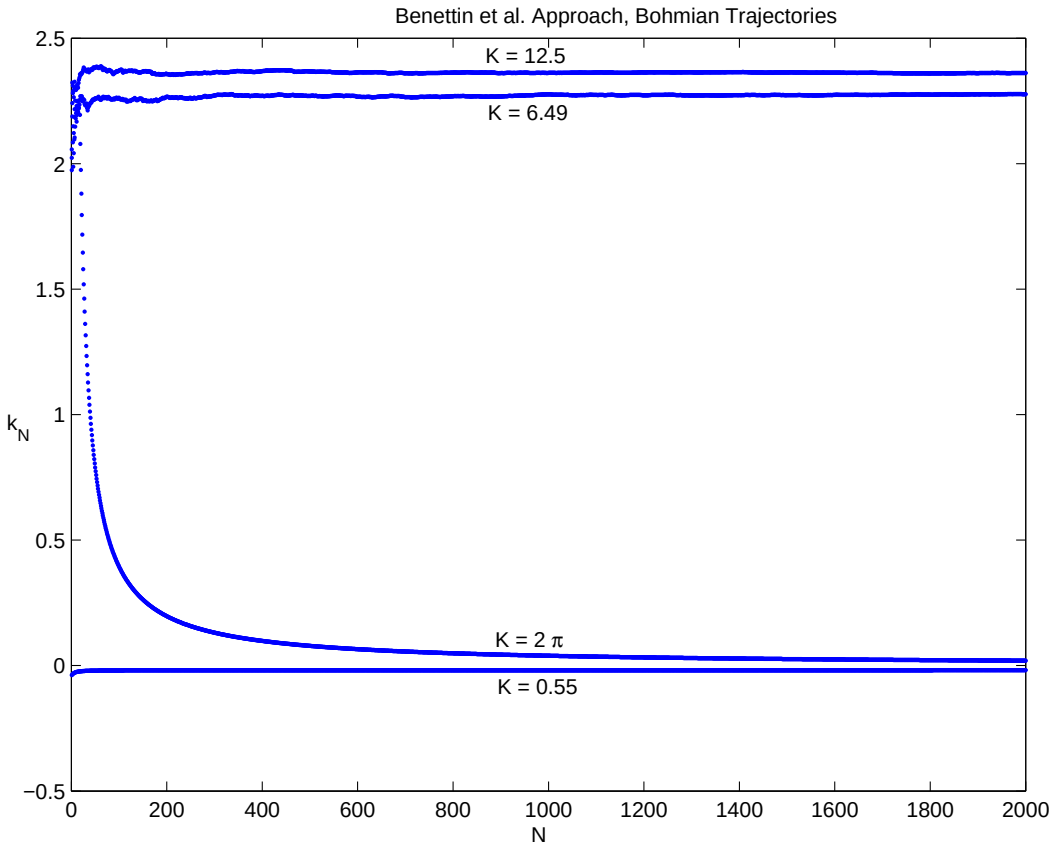

Figure 6.1: Benettin *et al.* approach for the Lyapunov exponent for Bohmian trajectories. $K = 12.5, 6.49, 2\pi$, and 0.55.

system, Fig. 6.2 shows the scan of K from 0 to 50 ($K = 0$ point skipped). The inset specifically presents the transition from non-chaotic to chaotic regimes. Two groups of regular motion in the chaotic sea are discovered in Fig. 6.2. The one is associated with even multiples of π and the other is associated with odd multiples of π.

The bar graphs of each pair in Fig. 6.2 illustrate the classical accelerator islands for even multiples of π. The single dashed lines show the position of $K = (2l + 1)\pi, l = 0, 1, 2, ...$ For showing more detail of the transition from the non-chaotic to chaotic, 500 points are evenly sampled

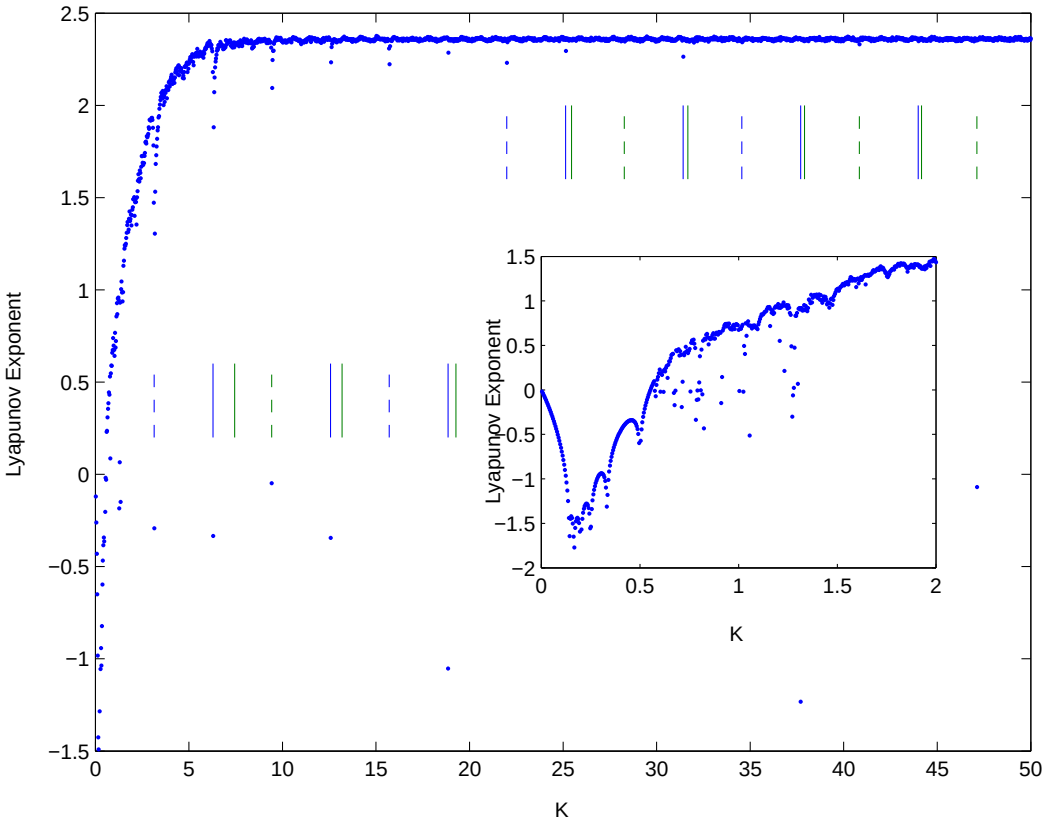

Figure 6.2: Lyapunov exponent of the Bohmian trajectories at Benettin *et al.* approach respecting to K. 2000 points are evenly sampled on K. The small figure shows the transition of non-chaotic to chaotic. 500 points are evenly sampled.

for K only from 0 to 2. Transition happens about at $K = 0.6$.

For further study of the the dips in Lyapunov exponent in areas surrounding $K = l\pi, l = 1, 2, 3, ...$, the resolution $\Delta K = 0.002$ is selected for further K scanning in Fig. 6.3. Actually, all regions for l up to 15 are investigated and they show results similar to Fig. 6.3. They are shown in App. D. Three conclusions can be summarized from those figures:

1) All those regions have points of Lyapunov exponents down to negative, which is the signature of non-chaos in the chaotic sea.

2) There are two groups of K odd integer times of π and even integer times of π. For the odd, $n\pi$ (n odd integer) is located at the center of the region. While for the even, $m\pi$ (m even integer) is located at the left edge of the region, the same as the classical fundamental accelerator islands. However these regions are much narrower than the correspondence classical accelerator and oscillator mode islands.

3) The width of the regions decreases as the order increases.

Stability regions occur periodically in the chaotic sea with period of π is the conclusion drawn from the numerical experiments. The width is very narrow and decreases as the K value increases.

6.5 Conclusion

The mapping of the quantum trajectories of the kicked rotor at quantum resonance is presented. Lyapunov exponents from the Benettin *et al.* approach are obtained for the first time from Bohmian trajectories. Quantum chaos is found for $K > 0.6$ for the quantum resonance case.

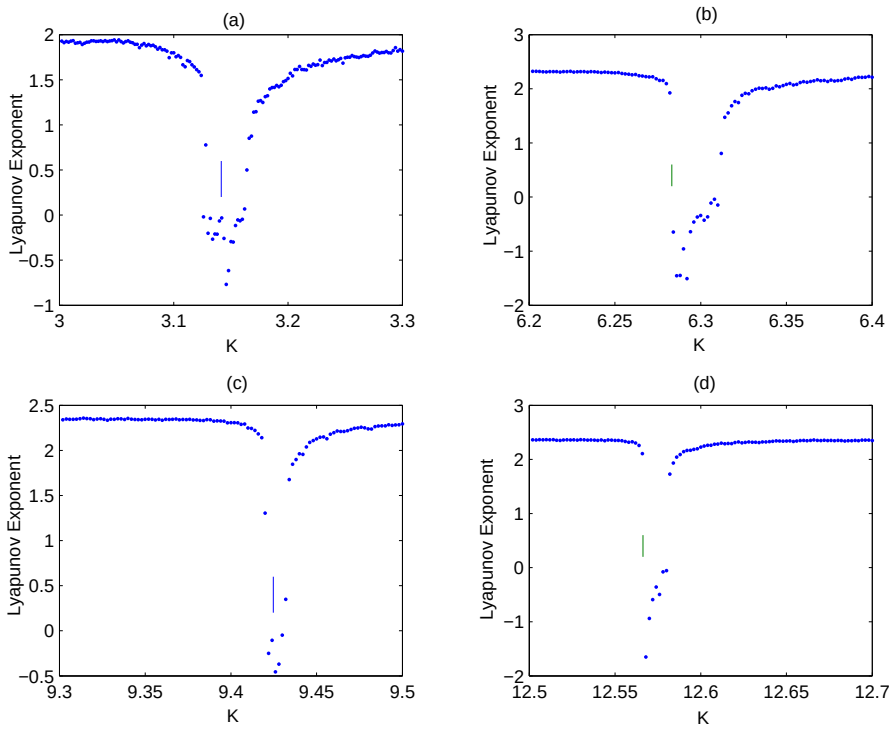

Figure 6.3: Higher resolution on Lyapunov exponent of the Bohmian trajectories from the Benettin *et al.* approach with respect to K. $\Delta K = 0.002$ (a) $K = \pi$ region, (b) $K = 2\pi$ region, (c) $K = 3\pi$ region (d) $K = 4\pi$ region.

Two groups of regular motion corresponding to the regions around odd multiples of π and even multiples of π are discovered. Stability domain exists in the chaotic sea with period π for Bohmian trajectories. However, the widths are much narrower compared to the classical case. The stability regions decrease as the order increases, which is the same as the classical case.

CHAPTER 7

QUANTUM MOMENTUM DIFFUSION OF THE KICKED ROTOR: STANDARD QUANTUM MECHANICAL APPROACH

7.1 Introduction

Using standard quantum mechanics, we obtain the general solution for momentum diffusion at quantum resonance. The analytical and numerical solutions both agree. For nonresonance the numerical simulation of standard quantum mechanics gives a momentum diffusion that saturates, which agrees with experimental results of the atom optics kicked rotor.

Since the first experimental atom optics realization of the quantum kicked rotor, the study of momentum diffusion has been especially important [18, 20, 24, 33, 34, 35, 38]. With atom optics kicked rotor, Peres's [62, 63] proposal of quantum chaos from perturbation on the potential can be arranged experimentally [4, 64]. The study of quantum accelerator modes [65] and quantum resonance [27, 66] can also be undertaken experimentally. In this chapter we study momentum diffusion of the quantum kicked rotor using numerical simulation, which is necessary to go beyond limited analytical solutions. Numerical diffusion rates are computed using a least squares fit to the numerical data. For all the calculations our own implemented programs in Matlab [51] are used.

The solution of the Schrödinger equation solved in Chapter 6 for the kicked rotor in the form of an expansion in momentum eigenstates is used, which is especially convenient to calculate

momentum diffusion.

The probability that the particle is in a momentum eigenstate $|l\rangle$ with momentum $l\bar{k}$ at time t_N is $|a_l(t_N)|^2$. Starting with an initial state vector $\psi(t_0)$, we obtain the coefficients at any subsequent time by iterating Eq. (6.9). Using these coefficients, we obtain the wave function and calculate the momentum diffusion for both resonance and nonresonance.

A general analytical solution for momentum diffusion at quantum resonance is obtained in Sec. 7.2. The specific cases of both plane wave and Gaussian initial momentum distribution are also derived analytically. The corresponding numerical computation for momentum diffusion for both resonance and nonresonance is carried out in Sec. 7.3. The conclusion is given in Sec. 7.4.

7.2 Momentum Diffusion at Quantum Resonance

At quantum resonance, for an initial state that is a momentum eigenstate $|\ p_0\rangle$, the momentum diffusion $\Delta\langle p^2\rangle = \langle p^2(t_N)\rangle - \langle p^2(t_0)\rangle$ calculated in the coordinate representation is

$$\begin{aligned}
\Delta\langle p^2\rangle &= \langle p^2(t_N)\rangle - \langle p^2(t_0)\rangle \\
&= \int_0^{2\pi} dx\ \{\psi^*(x,t_N)\hat{p}^2\psi(x,t_N) - \psi^*(x,t_0)\hat{p}^2\psi(x,t_0)\} \\
&= \int_0^{2\pi} dx\ \psi^*(x,t_0)\{N^2K^2V'(x)^2 + iNK\bar{k}V''(x) - 2NKV'(x)\hat{p}\}\psi(x,t_0),
\end{aligned} \tag{7.1}$$

from Eq. (6.12), where the canonical momentum operator is $\hat{p} = -i\bar{k}\partial/\partial x$ and $V'(x) = dV(x)/dx$.

The state vector in Eq. (6.5) for time t_0 in coordinate space $\psi(x,t_0) = \langle x\,|\psi(t_0)\rangle$ can be expanded in a complete set of momentum eigenfunctions $\langle x\,|l\rangle = \varphi_l(x) = (2\pi)^{-1/2}\exp(ilx)$, where $l = 0, \pm1, \pm2, ...$ If we take the periodic potential to be $V(x) = \cos x$, the evaluation of Eq. (7.1) gives

$$\begin{aligned} & \left\langle \hat{p}^2(t_N)\right\rangle - \left\langle \hat{p}^2(t_0)\right\rangle \\ = \;& K\bar{k}\sum_{l=-\infty}^{\infty}(2l+1)Im[a^*_{l+1}(t_0)a_l(t_0)]N + \frac{1}{2}K^2\{1 - \sum_{l=-\infty}^{\infty} Re[a^*_{l+1}(t_0)a_{l-1}(t_0)]\}N^2, \end{aligned} \quad (7.2)$$

where these coefficients are for an initial time $t_0 = 0$.

For an initial state that is a momentum eigenstate $|\psi(t_0)\rangle = |m\rangle$, the only nonzero coefficient is a_m. Therefore, the momentum diffusion in Eq. (7.2) is exactly [33, 67]

$$\left\langle \hat{p}^2(t_N)\right\rangle - \left\langle \hat{p}^2(t_0)\right\rangle = (K^2/2)N^2. \quad (7.3)$$

For an initial wave function $\psi(x,t_0)$ that has a Gaussian momentum distribution of real coefficients a_l

$$a_l = A\exp(-l^2), \quad \text{for } l = 0, \pm1, \pm2, \pm3, ... \quad (7.4)$$

where the normalization constant A is determined from $A^{-2} = \sum_{n=-\infty}^{\infty} \exp(-2n^2)$, only the quadratic term in time N^2 in Eq. (7.2) contributes. Performing the sum in Eq. (7.2), we obtain a momentum diffusion

$$\left\langle \hat{p}^2(t_N) \right\rangle - \left\langle \hat{p}^2(t_0) \right\rangle = 0.8647(K^2/2)N^2. \tag{7.5}$$

The following section gives the results of numerical simulations for some K values for initial zero momentum states and an initial state with a Gaussian momentum distribution. The numerical results are consistent with the analytical solutions.

7.3 Numerical Results for SQM

We now give the numerical momentum diffusion for SQM. Figure 7.1 gives the momentum distribution and momentum diffusion using an initial zero-momentum state with a control parameter $K = 12.5$ for both resonant and nonresonant cases. The expansion of the wave function in Eq. (6.5) is truncated at ± 150, which gives sufficient accuracy because the sum of the probabilities $|a_l|^2$ is 1.0000 for both cases.

Figure 7.1 (a) shows the probability distribution of momentum as a function of time from 0 to 100 kicks for nonresonance with $\bar{k} = 2$ and $K = 12.5$. Figure 7.1 (c) shows the probability distribution of momenta as a function of time from 0 to 100 kicks for resonance with $\bar{k} = 4\pi$ and $K = 12.5$. Both distributions have an expected symmetry around zero momentum.

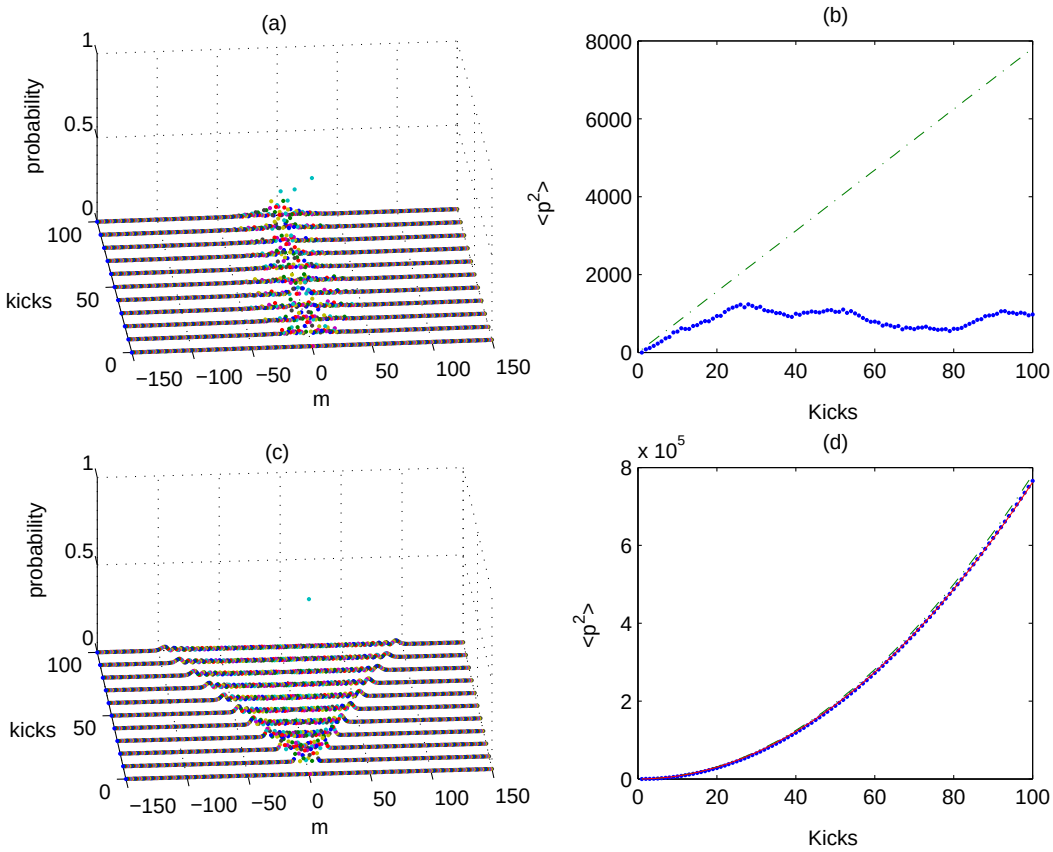

Figure 7.1: Probability distribution and momentum diffusion for standard quantum mechanics with an initial zero-momentum state. The control parameter is $K = 12.5$. (a) Probability distribution of momentum eigenvalues as a function of time from 0 to 100 kicks for nonresonance with $\bar{k} = 2$. (b) Momentum diffusion as a function of time (kicks) for the nonresonant case in (a). The dots are numerical data and the dash-dot line is the classical $(K^2/2)N$ for reference. (c) Probability distribution of momentum eigenvalues as a function of time from 0 to 100 kicks for resonance with $\bar{k} = 4\pi$. (d) Momentum diffusion as a function of time (kicks) for resonant case in (c). The dots are numerical data, the dash-dot line is $(K^2/2)N^2$ in Eq. (7.3), and the solid line is a fitted quadratic curve.

Figure 7.1 (b) shows the momentum diffusion for nonresonance with $\bar{k} = 2$. The dash-dot line is the classical linear momentum diffusion $(K^2/2)N$, which serves as a reference. The dots are the numerical experimental data which is linear between 0 and about 28 kicks, and then begins to saturate. Figure 7.1 (d) shows the momentum diffusion for resonance with $\bar{k} = 4\pi$. The dash-dot line is the momentum diffusion for an initial plane wave $(K^2/2)N^2$ in Eq. (7.3). The dots are the numerical simulation data that shows quadratic growth with a quadratic diffusion rate close to $K^2/2$. A least squares fit to the numerical data gives a quadratic diffusion rate of $D = 76.2$, which differs from the analytical diffusion rate of $K^2/2$ by 2.4% as shown in Table 7.1.

Figure 7.2 gives the results of momentum distribution and momentum diffusion using the initial Gaussian momentum distribution in Eq. (7.4) with a control parameter $K = 12.5$ for both the resonant and nonresonant cases. The initial Gaussian momentum distribution describes the atom optics kicked rotor more closely than the initial zero momentum state [33].

Figure 7.2 (a) shows the momentum distribution as a function of time from 0 to 100 kicks for the nonresonant case with $\bar{k} = 2$. Figure 7.2 (c) shows the momentum distribution as a function of time from 0 to 100 kicks for the resonant case with $\bar{k} = 4\pi$. Both distributions have an expected symmetry around zero momentum. The probability distributions are similar to Fig. 7.1 (a) and (c).

Figure 7.2 (b) for the nonresonant case with $\bar{k} = 2$ shows saturation after about 10 kicks, and is similar to the experimental data for the atom optics kicked rotor [33]. Figure 7.2 (d) shows the momentum diffusion for the resonant case with $\bar{k} = 4\pi$, which is quadratic in kicks (time). For $K = 12.5$ the theoretical momentum diffusion in Eq. (7.5) gives a rate $D = 67.5$, while the numerical

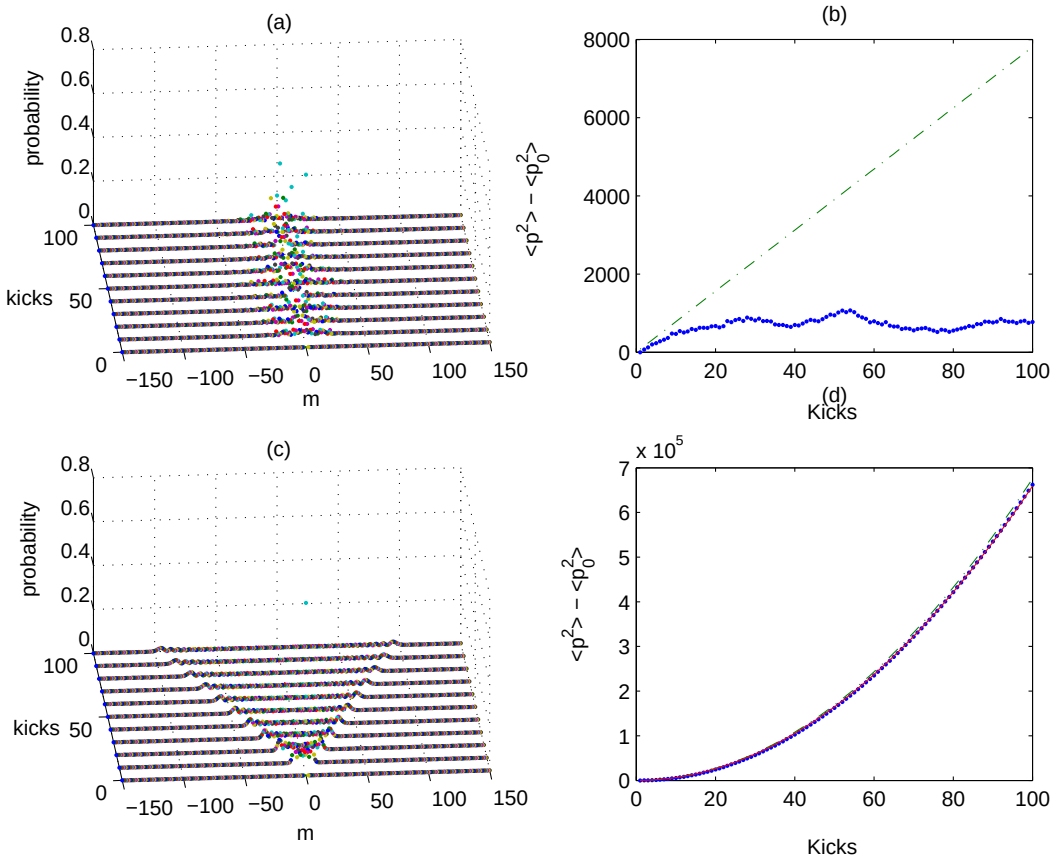

Figure 7.2: Probability distribution and momentum diffusion for standard quantum mechanics with an initial Gaussian distribution of momentum eigenvalues. The control parameter is $K = 12.5$. (a) Probability distribution of momentum eigenvalues as a function of time from 0 to 100 kicks for nonresonance with $\bar{k} = 2$. (b) Momentum diffusion as a function of time (kicks) for the nonresonant case in (a). The dots are numerical data and the dash-dot line is the classical $(K^2/2)N$ for reference. (c) Probability distribution of momentum eigenvalues as a function of time from 0 to 100 kicks for resonance with $\bar{k} = 4\pi$. (d) Momentum diffusion as a function of time (kicks) for resonant case in (c). The dots are numerical data, the dash-dot line is the theoretical curve in Eq. (7.5), and the solid line is a fitted quadratic curve.

simulation gives a rate $D = 65.9$, which is a 2.4% error.

K	12.5	12.5	6.49	0.96
Initial State	$p_0 = 0$	Gaussian	Gaussian	Gaussian
Theoretical	78.1	67.5	18.2	0.398
Experimental	76.2	65.9	17.8	0.389
Percent Error	2.4%	2.4%	2.2%	2.3%

Table 7.1: Standard quantum mechanics quadratic diffusion rates D at resonance with different control parameters K and different initial states for numerical simulation data and theoretical values in Eq. (7.2).

Table 7.1 compares the theoretical and numerical quadratic diffusion rates for resonance with $\bar{k} = 4\pi$. For a control parameter $K = 12.5$ we show both the initial zero-momentum state and the initial Gaussian momentum distribution. The initial Gaussian distribution is used for $K = 6.49$, the control parameter for the classical first mode anomalous momentum diffusion, and for $K = 0.96$, a control parameter in a classically nonchaotic regime. The momentum diffusion with $K = 6.49$ and 0.96 for resonance and nonresonance show behavior similar to Fig. 7.2. There seems to be no correlation between momentum diffusion in the classical and the quantum cases.

7.4 Conclusion

For quantum resonance the momentum diffusion is quadratic in time if all coefficients in the momentum eigenstate expansion for the initial wave function are real. The momentum diffusion is $(K^2/2)N^2$ times a constant less than or equal to unity depending on the coefficients in the momentum eigenstate expansion of the initial state. For an initial zero momentum state the constant is

unity. Quantum resonance occurs when the scaled Planck's constant $\bar{k}$ is equal to an integer times 4π in both approaches and the momentum diffusion depends on the control parameter K.

Using the standard approach to quantum mechanics for nonresonance, it is found from the numerical simulation that both plane wave and Gaussian distribution of the initial momentum states gives a momentum diffusion that saturates. This result is in agreement with the atom optics kicked rotor experimental results [33].

CHAPTER 8

QUANTUM MOMENTUM DIFFUSION OF THE KICKED ROTOR: DE BROGLIE-BOHM APPROACH

8.1 Introduction

The de Broglie-Bohm (BB) approach introduces quantum trajectories in quantum mechanical systems in analogy with classical mechanics. A quantum potential is fundamental in BB. Indeed, the quantum potential is obtained from the quantum Hamilton-Jacobi equation by comparison with classical Hamilton-Jacobi equation [12]. The quantum potential and quantum force are both "fictitious" in the sense that quantum potential is part of kinetic energy.

The kicked rotor, or standard map, plays an important role in both the classical and quantum study of chaos and provides a testing ground in many aspects for theoretical study. Since the first experimental realization of atom optics quantum kicked rotor, the study of momentum diffusion has been especially important [18, 33]. Numerical study of momentum diffusion of Bohmian trajectories supports the view that the quantum potential is fictitious. This conclusion is supported by comparing the results of BB with the SQM approach in Chapter 7.

In Sec. 8.2 the argument is provided that the quantum potential is fictitious. In Sec. 8.3 analytical solution is given for the momentum diffusion in terms of wavefunction, which is the foundation for the numerical computation. Sec. 8.4 gives the numerical results of momentum diffusion for both

resonance and nonresonance. The conclusion is given in Sec. 8.5.

8.2 Fictitious Quantum Potential

SQM is well developed and supported by experimental results. The fundamental principles of SQM should not be violated. For SQM, the kinetic energy operator is $\hat{T} = \hat{\mathbf{p}}^2/2m$, where $\hat{p} = -i\hbar\nabla$ is the momentum operator and m is the mass. If we express the wavefunction in polar form $\psi = Rexp(iS/\hbar)$ in the way introduced by BB, the physical observable of the average kinetic energy is

$$\begin{aligned} \langle \hat{T} \rangle &= \int d\mathbf{x}\, \psi^* \left(-\frac{\hbar^2}{2m}\nabla^2 \right) \psi \\ &= \int d\mathbf{x}\, R^2 \left(\frac{(\nabla S)^2}{2m} + Q \right) \end{aligned} \tag{8.1}$$

where

$$Q = -\frac{\hbar^2}{2m}\frac{\nabla^2 R}{R} \tag{8.2}$$

is defined as the quantum potential and $\nabla S = \mathbf{p}$ is defined as the momentum of the quantum particle [12]. More specifically for one dimensional, the local kinetic energy $\mathcal{T}$ in dimensionless units is [68]

$$\mathcal{T}(x,t) = Re\left[\frac{\psi^* \hat{T} \psi}{\psi^* \psi}\right] = \frac{1}{2} S'^2 + Q, \tag{8.3}$$

where the kinetic energy operator is $\hat{T} = -\bar{k}^2 \partial^2/\partial x^2$ and the quantum potential is $Q = -\bar{k}^2 R''/R$ with $\bar{k}$ the scaled Planck's constant.

For the kicked rotor the scaled Planck's constant is $\bar{k} = \hbar k_0^2 T/M$, where $\hbar$ is Planck's constant, T is the period of the kicks, M is the mass, and k_0 is the wave number associated with the periodic potential energy. Therefore the kinetic energy calculated from the momentum $p = S'$ in the de Broglie-Bohm theory does not give the full quantum mechanical kinetic energy. The de Broglie-Bohm approach can give results different from standard quantum mechanics if this feature is not taken into account. For the kicked rotor in an initial momentum eigenstate, the case of quantum resonance with a scaled Planck's constant $\bar{k} = 4\pi$ gives a quantum potential equal to zero $Q = 0$. Therefore, in this case the de Broglie-Bohm kinetic energy is $p^2/2 = \mathcal{T}(x,t)$, the local value of the kinetic energy operator.

In general, if the quantum potential is zero, the expectation value of the kinetic energy is the average $\left\langle (\nabla S)^2/2m \right\rangle$ over a constant spatial distribution at each time. If Q is not zero $\left\langle (\nabla S)^2/2m \right\rangle$ does not equal to the average of the momentum of SQM.

We will show in the following momentum diffusion simulation of the quantum kicked rotor that for quantum resonance ($\bar{k} = 4\pi$ or a positive integer multiple) and initial plane wave that BB agrees with SQM, where the quantum potential is zero. On the other hand, for non-resonance a naive use of Eq. (8.4) to obtain BB trajectories gives incorrect results, as shown in Fig. 8.1 (a) below because

the quantum potential has not been included to obtain the trajectories. For non-resonance SQM gives the saturation shown in Figs. 7.1 and 7.2 that agrees with the experimental results [33].

8.3 Momentum Diffusion at Resonance: BB

In BB, using the current definition, the momentum is [12]

$$p = \partial S/\partial x = S'(x,t), \tag{8.4}$$

where the phase of the wave function is $S/\bar{k}$ [11, 12]. For the wave function $\psi = R\exp(iS/\bar{k})$, the momentum or the velocity of the trajectory is therefore taken to be

$$p(t) = \dot{x}(t) = \bar{k}Im\left[\frac{\psi'(x,t)}{\psi(x,t)}\right]_{x=x(t)}, \tag{8.5}$$

where the mass is taken as unity and $\psi' = \partial\psi/\partial x$. Substituting the expansion in Eq. (6.5) for the wave function, we obtain

$$p(t) = Re\left[\frac{\sum_{l=-\infty}^{\infty} a_l(t)p_l\exp(ilx)}{\sum_{m=-\infty}^{\infty} a_m(t)\exp(imx)}\right]_{x=x(t)} \tag{8.6}$$

where $p_l \equiv l\bar{k}$ is the momentum of the state $|l\rangle$.

The quantum potential Q in dimensionless units is

$$Q(x,t) = -\frac{\bar{k}^2}{2}\frac{R''}{R}, \tag{8.7}$$

where $R'' = \partial^2 R/\partial x^2$. Expressed in terms of the wave function the quantum potential Eq. (8.7) is

$$Q(x,t) = -\frac{1}{2}\bar{k}^2 \left\{ Re\left(\frac{\psi''}{\psi}\right) + \left[Im\left(\frac{\psi'}{\psi}\right)\right]^2 \right\}. \tag{8.8}$$

For an initial zero momentum state and quantum resonance, where $\bar{k} = 4\pi n$ and $n = 1, 2, ...,$ the de Broglie-Bohm approach simplifies. If the initial state is a momentum eigenstate $|l_0\rangle$ with momentum $p_0 \equiv l_0\bar{k}$, then in the coordinate representation this state is the wave function $\psi(x,0) = \varphi_{l_0}(x) = (2\pi)^{-1/2}\exp(ikl_0x)$. From Eq. (6.12) this wave function evolves into

$$\psi(x,t_N) = (2\pi)^{-1/2}\exp\{i[l_0x - kNV(x)]\}, \tag{8.9}$$

at the N^{th} kick. From Eqs. (8.9) and (8.4) the momentum after N kicks is therefore

$$p(t_N) = p_0 - NKV'(x), \tag{8.10}$$

where $p_0 = l_0\bar{k}$ and $x = x(t_N)$.

If we choose $V(x) = \cos x$, then

$$p(t_N) = p_0 + NK\sin[x(t_N)]. \tag{8.11}$$

By squaring Eq. (8.11) and taking the average, we obtain the momentum diffusion

$$\langle p^2(t_N)\rangle - p_0^2 = (K^2/2)N^2, \tag{8.12}$$

since p_0 is a constant, $\langle \sin x(t_N)\rangle = 0$ and $\langle \sin^2 x(t_N)\rangle = 1/2$.

In the quantum resonance case $\bar{k} = 4\pi n$, where $n = 1, 2, ...$, an initial momentum eigenstate evolves into Eq. (8.9) so the quantum potential in Eq. (8.7) is zero $(Q = 0)$ because $R = |\psi| = (2\pi)^{-1/2}$ is a constant.

8.4 Numerical Results for BB

Figure 8.1 shows momentum diffusion in the BB approach with a control parameter $K = 12.5$ and an initial zero-momentum state for both resonance and nonresonance. For the nonresonant case in Fig. 8.1 (a) the momentum diffusion, calculated from Eq. (8.4), shows some saturation, but much less than in Fig. 7.1 (b) for SQM. The reason for this disagreement is that the quantum potential in Eq. (8.7) has not been included in the momentum diffusion. Figure 8.1 (b) shows a plot of the weighted average of twice the quantum potential $2Q$ in Eq. (8.7) as a function of kicks (time). It is similar to Fig. 8.1 (a) in that it shows some saturation. When Figs. 8.1 (a) and (b) are added together to get twice the quantum kinetic energy $2\langle \hat{T} \rangle$, which is $< p^2 >$ in dimensionless units. The momentum diffusion in Fig. 8.1 (c) agrees with Fig. 7.1 (b), as it should.

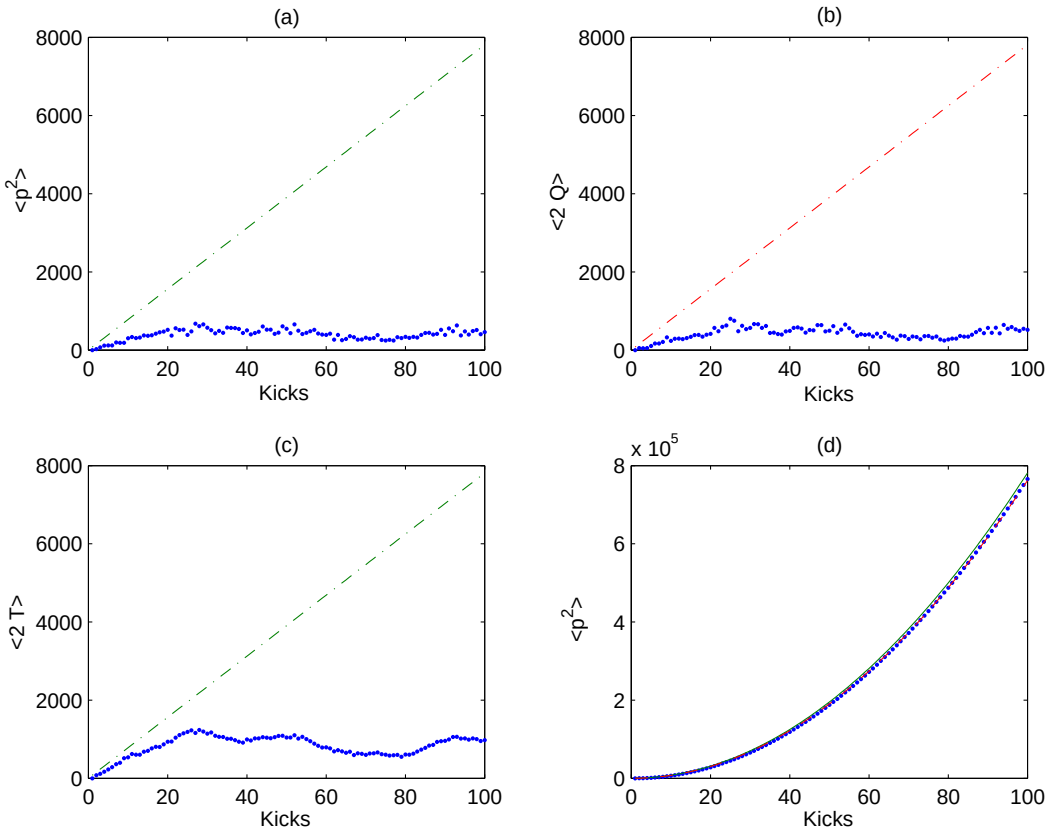

Figure 8.1: Momentum diffusion de Broglie-Bohm approach with an initial zero-momentum state. The control parameter is $K = 12.5$. Subgraphs (a), (b), and (c) are for the nonresonant case with $\bar{k} = 2$, where the dash-dot lines are the classical $(K^2/2)N$ for reference. (a) The numerical data of a weighted average for $(S')^2$ for time from 0 to 100 kicks. (b) The numerical data of a weighted average for twice the quantum potential $2Q$ for time from 0 to 100 kicks. (c) The sum of (a) and (b), which is a weighted average for twice the quantum kinetic energy. (d) Resonant case with $\bar{k} = 4\pi$. The dots are the numerical data, the dash-dot curve is $(K^2/2)N^2$ for reference, and the solid line is a fitted quadratic curve.

Figure 8.1 (d) and Fig. 7.1 (d) for resonance agree with each other because the quantum potential is zero. There is good agreement in Fig. 8.1 (d) between the numerical simulation and the theoretical curve in Eq. (7.3).

K	12.5	6.49	0.96
Initial State	$p_0 = 0$	$p_0 = 0$	$p_0 = 0$
Theoretical	78.1	21.1	0.461
Experimental	76.2	20.5	0.450
Percent Error	2.4%	2.8%	2.4%

Table 8.1: de Broglie-Bohm quadratic diffusion rates D at resonance with different control parameters K and an initial zero-momentum $(p_0 = 0)$ for numerical simulation data and theoretical values in Eq. (8.12).

For an initial zero-momentum state Table 8.1 compares the theoretical and the experimental (numerical) diffusion rates at quantum resonance for different control parameters. The momentum diffusion with control parameters $K = 6.49$ and 0.96 are similar to Fig. 8.1 for $K = 12.5$. For these control parameters there is no correspondence between the classical and quantum momentum diffusion.

8.5 Conclusion

Both numerical and analytical solutions for BB are obtained. For resonance the quantum potential is zero and the same results are obtained from BB at momentum diffusion for $\mathbf{p} = \nabla S$ as for SQM. For non-resonance a naive application of the BB for the momentum diffusion with $\mathbf{p} = \nabla S$ only does not give correct results. The reason is that the quantum potential is not included as part

of the total quantum kinetic energy, since it is a fictitious potential. The total quantum kinetic energy average $< \hat{T} >$ is the summation $< (\nabla S)^2/2m >$ and the quantum potential average $< Q >$ as shown by analysis in Sec. 8.2 and numerical calculations in Sec. 8.4.

CHAPTER 9

SUMMARY AND DISCUSSION

Chaos and momentum diffusion are studied for both classical and quantum kicked rotor. It is shown that even for the well-studied classical kicked rotor, or standard model, new discoveries are still possible. For the classical kicked rotor, the local Lyapunov exponent is defined and studied. An upper bound is found analytically for the local Lyapunov exponent as a function of time. A numerical simulation is performed and shown to be a powerful and useful method. The Benettin *et al.* approach to the Lyapunov exponent is accepted for bounded systems. This Lyapunov exponent gives a general correspondence of the chaotic and non-chaotic regimes as a function of the control parameter K with that of the Poincaré phase space portraits. However, the portraits are just sampled over a few K values and are rather coarse. The scanning over K for Lyapunov exponents is performed numerically and results in the discoveries of stability regions in the chaotic sea. Analytical explanations are provided for even multiples of π group and an empirical formula is obtained for the stability regions for odd multiples of π group.

Momentum diffusion of the classical kicked rotor, especially anomalous diffusion, is studied here both analytically and numerically. An upper bound for anomalous diffusion is obtained analytically. The non-linear diffusion rate, or coefficient in the power law behavior, and the exponent of the time for anomalous diffusion as functions of the control parameter K are obtained numerically for regions

of K from 0 to 100. Those values can also be compared with the quantum kicked rotor momentum diffusion and a study of the quantum to classical correspondence.

We show that the quantum potential is a fictitious potential in the sense that it is part of the kinetic energy. The quantum potential is derived from the real part of the equation obtained when the wave function in polar form is substituted into the Schrödinger equation. Indeed by looking at the local value of the quantum kinetic energy in standard quantum mechanics, both a de Broglie-Bohm kinetic energy and the quantum potential are obtained. This is also verified by numerical experiment on quantum momentum diffusion, which shows that by adding the two parts together, the quantum kinetic energy of the system is obtained.

The quantum kicked rotor and quantum atom optics kicked rotor are also studied in this dissertation. For a quantum chaos approach that is analogous to the definition of classical deterministic chaos, the de Broglie-Bohm trajectories of the quantum kicked rotor is studied. The map of the quantum trajectories at quantum resonance is presented first. Quantum chaos is found from this approach. The quantum Lyapunov exponents at quantum resonance show that the onset of chaos takes place for $K > 0.6$. However, there are stability regions in the chaotic sea happened periodically at period π that are similar to the classical regions. The widths of the quantum regions are much less than that of the classical regions.

Analytical studies and numerical experiments for the momentum diffusion of the quantum kicked rotor are performed for both traditional quantum mechanics and the de Broglie-Bohm approach. The results of our numerical experiments are consistent with those of the real atom optics experiments.

Numerical computation and trajectory simulation are proved to be useful and insightful. They can go beyond the limited analytical solutions. The numerical experiments using computers and programming eliminate the necessity of more expensive and complicated experimental equipment in the laboratory.

It is not possible to exhaust this rich subject in one dissertation. Indeed the subject dealt with in this research has both broadness and depth. We focus on the famous standard model, or kicked rotor and study some very important areas. We achieve new results for classical and quantum chaos and momentum diffusion, as well as the de Broglie-Bohm approach to quantum mechanics. Numerical simulation, computation and experiment combined with analytical methods are a powerful method for research. This dissertation opens a broad theoretical area, which involves numerical and analytical methods. Problems for further study include the quantum to classical correspondence principle, quantum chaos when the quantum potential is nonzero, and quantum Poincaré phase space portraits. This dissertation provides a foundation for further study in my scientific career.

APPENDIX A

MATHEMATICAL DETAILS

A.1 Dimensionless Hamiltonian

The Hamiltonian of the kicked rotor in standard units is

$$\widetilde{H} = \frac{\widetilde{p}^2}{2M} + \widetilde{K}\widetilde{V}(\widetilde{x}) \sum_{n=-\infty}^{\infty} \delta(\widetilde{t} - nT) \tag{A.1}$$

Define dimensionless units as $x \equiv k_0\widetilde{x}$, momentum $p \equiv (k_0T/M)\widetilde{p}$ and time $t \equiv \widetilde{t}/T$, then multiplying Eq. (A.1) by $k_0^2T^2/M$ yields

$$\frac{k_0^2T^2}{M}\widetilde{H} = [\frac{k_0T}{M}\widetilde{p}]^2/2 + \frac{k_0^2T^2}{M}\widetilde{K}\widetilde{V}(x/k_0) \sum_{-\infty}^{\infty} \delta(tT - nT) \tag{A.2}$$

$$= \frac{p^2}{2} + KTV(x) \sum_{-\infty}^{\infty} \delta(tT - nT) \tag{A.3}$$

Here $K \equiv \widetilde{K}k_0^2T/M$ and the scaled potential $V(x) \equiv \widetilde{V}(x/k_0)$.

The integral of the $\delta-$ function is

$$\int_{-\infty}^{\infty} \delta(t-n)dt = \int_{-\infty}^{\infty} \delta(\widetilde{t} - nT)d\widetilde{t} \tag{A.4}$$

since

$$\delta(tT - nT) = \frac{1}{T}\delta(t - n) \tag{A.5}$$

Further define

$$H = \frac{k_0^2 T^2}{M}\widetilde{H} \tag{A.6}$$

From Eq. (A.3), we have

$$H \equiv \frac{p^2}{2} + KV(x)\sum_{n=-\infty}^{\infty}\delta(t - n) \tag{A.7}$$

This is the dimensionless Hamiltonian.

A.2 Schrödinger Equation in Dimensionless Units

The Schrödinger equation of the kicked rotor is

$$\not{h}\frac{\partial}{\partial\widetilde{t}}\Psi(\widetilde{x}) = \hat{\widetilde{H}}\Psi(\widetilde{x}) \tag{A.8}$$

$$= \frac{M}{k_0^2 T^2}\hat{H}\Psi(\widetilde{x}) \tag{A.9}$$

Multiplying both sides by $k_0^2 T^2/M$ and realized that $\partial/\partial\widetilde{t} = (1/T)\partial/\partial t$, we have

$$i(\frac{\bar{h}k_0^2T}{M})\frac{\partial}{\partial t}\Psi(x) = \hat{H}\Psi(x) \tag{A.10}$$

Define the scaled Planck's constant $\bar{k} \equiv \bar{h}k_0^2T/M$. Then from Eq. (A.10), we obtain

$$i\bar{k}\frac{\partial}{\partial t} \mid \psi\rangle = \hat{H} \mid \psi\rangle \tag{A.11}$$

The dimensionless Schrödinger equation.

A.3 Worst Case Scenario

From equation (4.2), let's develop worst case scenario.

Assuming two trajectories initially start at $x_1(0) = x_0$ and $x_2(0) = x_0 + d(0)$ where $d(0)$ is positive without losing the generality. Then let's do the iterations, which starts from $p_1(t_0)$. According to equation 4.2

$$p_1(t_1) = p_1(t_0) + ksin(x_1(t_0)) \geq p_1(t_0) - k \tag{A.12}$$

since *sin* is no less than -1.

By mathematical induction, assuming that

$$p_1(t_{N-1}) \geq p_1(t_0) - (N-1)k \tag{A.13}$$

Then

$$p_1(t_N) = p_1(t_{N-1}) + ksin(x_1(t_{N-1})) \tag{A.14}$$

$$\geq p_1(t_0) - (N-1)k - k \tag{A.15}$$

$$= p_1(t_0) - Nk \tag{A.16}$$

So we have proved that in general

$$p_1(t_N) \geq p_1(t_0) - Nk \tag{A.17}$$

Similarly, because sin is no more than 1 and by similar induction, we have

$$p_2(t_N) \leq p_2(t_0) + Nk \tag{A.18}$$

For the coordinate, still start from equation (4.2), we have

$$x_1(t_1) = x_1(t_0) + T p_1(t_1) \tag{A.19}$$

$$= x_0 + T[p_1(t_0) + ksin(x_1(t_0))] \tag{A.20}$$

$$\geq x_0 + T[p_1(t_0) - k] \tag{A.21}$$

$$= x_0 + T p_1(t_0) - Tk \tag{A.22}$$

Again, by mathematical induction, assuming that

$$x_1(t_{N-1}) \geq x_0 + (N-1)T p_1(t_0) - [1+2+\cdots+(N-1)]Tk \tag{A.23}$$

Then,

$$x_1(t_N) = x_1(t_{N-1}) + T p_1(t_N) \tag{A.24}$$

$$\geq x_0 + (N-1)T p_1(t_0) - [1+2+\cdots+(N-1)]Tk + T[p_1(t_0) - Nk] \tag{A.25}$$

$$= x_0 + NT p_1(t_0) - [1+2+\cdots+N]Tk \tag{A.26}$$

$$= x_0 + NT p_1(t_0) - \frac{N(N-1)}{2}Tk \tag{A.27}$$

So, in general, we have proved

$$x_1(t_N) \geq x_0 + NTp_1(t_0) - \frac{N(N+1)}{2}Tk \tag{A.28}$$

Similarly, since the maximum of sin is 1, for $x_2(t_N)$

$$x_2(t_N) \leq x_0 + d(0) + NTp_2(t_0) + \frac{N(N+1)}{2}Tk \tag{A.29}$$

A.4 Quantum Potential Terms

The quantum theory of motion, or BB theory, expresses the wavefunction in polar form of the dimensionless coordinates

$$\psi(x,t) = R(x,t)e^{iS(x,t)/\bar{k}} \tag{A.30}$$

Then acting operator ∇ on Eq. (A.30), we have

$$\nabla\psi(x,t) = (\nabla R)e^{iS/\bar{k}} + R(\frac{i\nabla S}{\bar{k}})e^{iS/\bar{k}} \tag{A.31}$$

$$= (\frac{\nabla R}{R})\psi + i(\frac{\nabla S}{\bar{k}})\psi \tag{A.32}$$

And acting operator ∇ on Eq. (A.32), we obtain

$$\nabla^2\psi(x,t) = \{(\nabla^2 R) + (\nabla R)(\frac{i\nabla S}{\bar{k}}) + i(\frac{\nabla R \nabla S}{\bar{k}}) + iR(\frac{\nabla^2 S}{\bar{k}}) - R(\frac{\nabla S}{\bar{k}})^2\} e^{iS/\bar{k}} \tag{A.33}$$

$$= \{\frac{\nabla^2 R}{R} - (\frac{\nabla S}{\bar{k}})^2 + i[\frac{2\nabla R \nabla S}{\bar{k} R} + \frac{\nabla^2 S}{\bar{k}}]\}\psi \tag{A.34}$$

The real parts of $\nabla^2\psi/\psi$ from Eq. (A.34) are

$$Re(\frac{\nabla^2\psi}{\psi}) = \frac{\nabla^2 R}{R} - [\frac{\nabla S}{\bar{k}}]^2 \tag{A.35}$$

And the imaginary parts of $[\nabla\psi/\psi]^2$ from Eq. (A.32) are

$$[Im(\frac{\nabla\psi}{\psi})]^2 = (\frac{\nabla S}{\bar{k}})^2 \tag{A.36}$$

Add Eq. (A.35) and Eq. (A.36) together, we obtain

$$Re(\frac{\nabla^2\psi}{\psi}) + [Im(\frac{\nabla\psi}{\psi})]^2 = \frac{\nabla^2 R}{R} \tag{A.37}$$

The quantum potential for this dimensionless coordinate in terms of the wavefunction is

$$Q(x,t) = -\frac{\bar{k}^2}{2}\frac{\nabla^2 R}{R} = -\frac{\bar{k}^2}{2}\{Re(\frac{\nabla^2\psi}{\psi}) + [Im(\frac{\nabla\psi}{\psi})]^2\}. \tag{A.38}$$

A.5 Expansion in Bessel Function

Since

$$cosx = \frac{e^{ix} + e^{-ix}}{2} \tag{A.39}$$

we have

$$-ikcosx = \frac{-ike^{ix} - ike^{-ix}}{2} \tag{A.40}$$

$$= (\frac{k}{2})[(-ie^{-ix}) - (\frac{1}{-ie^{-ix}})] \tag{A.41}$$

$$= \frac{k}{2}(y - \frac{1}{y}) \tag{A.42}$$

where $y \equiv -ie^{-ix}$.

Using the generating function of the Bessel function $e^{(k/2)(y-1/y)} = \sum_{n=-\infty}^{\infty} J_n(k)y^n$, we have

$$e^{-ikcosx} = e^{(k/2)(y-1/y)} \tag{A.43}$$

$$= \sum_{n=-\infty}^{\infty} J_n(k)(-ie^{-ix})^n \tag{A.44}$$

$$= \sum_{n=-\infty}^{\infty} (-i)^n J_n(k)e^{-inx} \tag{A.45}$$

A.6 Coefficients

Let us now substitute Eq. (A.45) into Eq. (6.7). Since

$$V_{ml} = \langle m \mid e^{-ikcosx} \mid l \rangle \tag{A.46}$$

$$= \langle m \mid \sum_{n=-\infty}^{\infty} (-i)^n J_n(k) e^{-inx} \mid l \rangle \tag{A.47}$$

$$= \sum_{n=-\infty}^{\infty} (-i)^n J_n(k) \langle m \mid e^{-inx} \mid l \rangle \tag{A.48}$$

Using the orthonormality property of the functions, the condition for $\langle m \mid e^{-inx} \mid l \rangle \neq 0$ is $n = l - m$. So, we have

$$V_{ml} = (-i)^{l-m} J_{l-m}(k) \tag{A.49}$$

which gives

$$a_m(t_n + t') = e^{-im^2 \bar{k} t'/2} \sum_{l=-\infty}^{\infty} (-i)^{l-m} J_{l-m}(k) a_l(t_n) \tag{A.50}$$

where $0 < t' \leq 1$ for the duration after the kick of $t = t_n$ and before the kick of $t = t_{n+1}$.

A.7 Mathematical Induction for the Oscillator Modes

By doing iterations as presented in table (4.1), it can be seen that the motion repeats itself at four kicks. Now let's do mathematical induction as follow:

Assume that at the $4(N-1)th$ kick, the momentum is zero and the coordinate is θ, then at $4(N-1)+1$ kick

$$p_{4(N-1)+1} = p_{4(N-1)} + Ksin\theta = m\pi \tag{A.51}$$

$$x_{4(N-1)+1} = x_{4(N-1)} + p_{4(N-1)+1} = \theta' \tag{A.52}$$

At $4(N-1)+2$ kick, the momentum and coordinate are

$$p_{4(N-1)+2} = p_{4(N-1)+1} + Ksin\theta' = 0 \tag{A.53}$$

$$x_{4(N-1)+2} = x_{4(N-1)+1} + p_{4(N-1)+2} = \theta' \tag{A.54}$$

By doing further iteration, at $4(N-1)+2$ kick, the momentum and coordinate are

$$p_{4(N-1)+3} = p_{4(N-1)+2} + Ksin\theta' = -m\pi \tag{A.55}$$

$$x_{4(N-1)+3} = x_{4(N-1)+2} + p_{4(N-1)+3} = \theta \tag{A.56}$$

At the integer times of 4 kicks of $4Nth$ kick, the momentum and coordinate go back to the original.

$$p_{4N} = p_{4(N-1)+3} + Ksin\theta = 0 \tag{A.57}$$

$$x_{4N} = x_{4(N-1)+3} + p_{4N} = \theta \tag{A.58}$$

It is proved in general that this oscillator mode is a period four motion.

APPENDIX B

FIGURES OF CLASSICAL STABILITY REGIONS AT CHAOTIC SEA

We show more figures for the detailed view of the stability regions in chaotic sea similar to Fig. 4.6 in Chapter 4. The regions are from 7π to 16π. All show a dip in the Lyapunov exponent in areas surrounding an integer times π. The widths are decreasing as the order increasing. The widths of even multiples of π group is relatively larger than that of the odd multiples of π group.

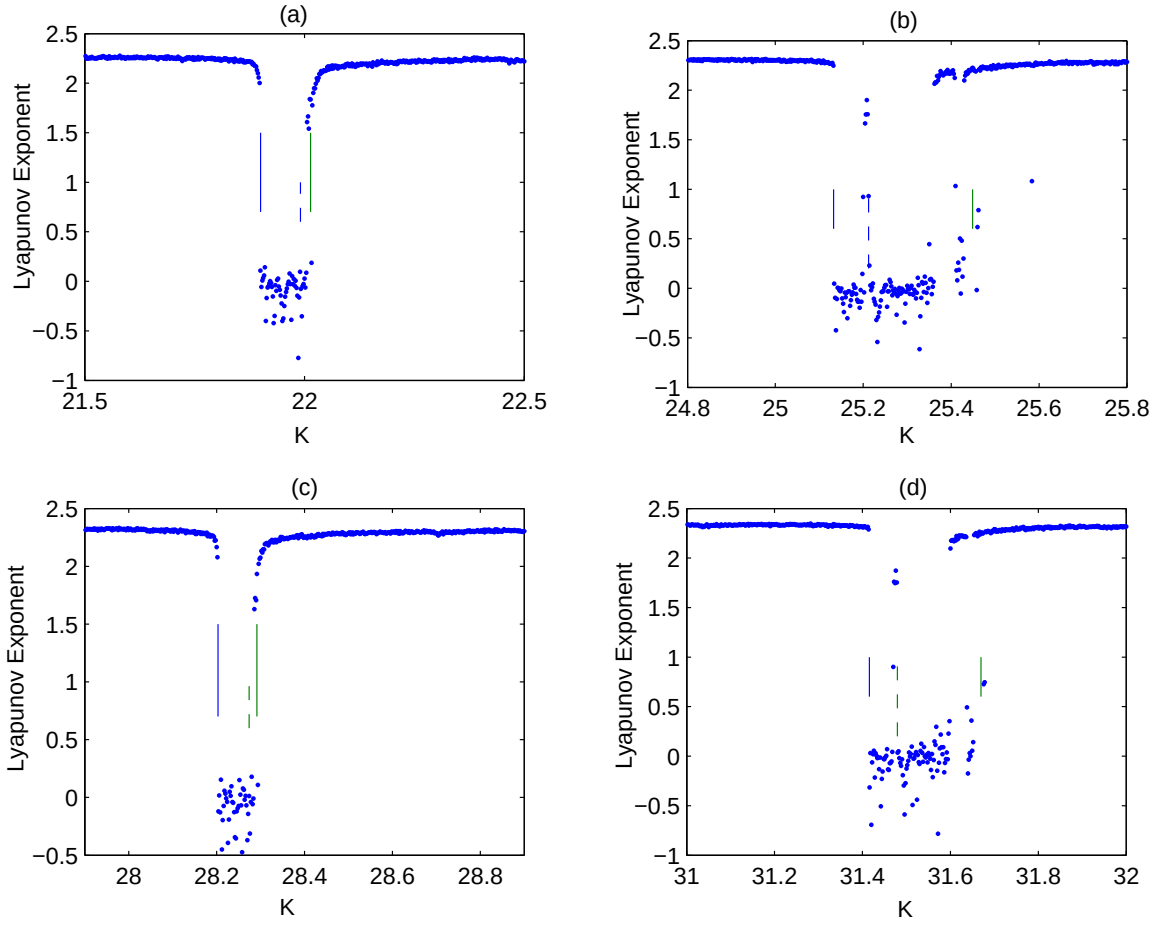

Figure B.1: Higher resolution on K for the Lyapunov exponent of the classical trajectories at Benettin *et al.* approach. $\Delta K = 0.002$ (a) $K = 7\pi$ region. Dashed line points to $K = 7\pi$ and solid lines illustrate region of Eq. (4.13) (b) $K = 8\pi$ region. Solid lines illustrate region of Eq. (4.12) while the dashed line is the right boundary of the second accelerator mode islands (c) $K = 9\pi$ region. Dashed line points to $K = 9\pi$ and solid lines illustrate region of Eq. (4.13) (d) $K = 10\pi$ region. Solid lines illustrate region of Eq. (4.12) and the dashed line is the right edge of the second accelerator mode islands.

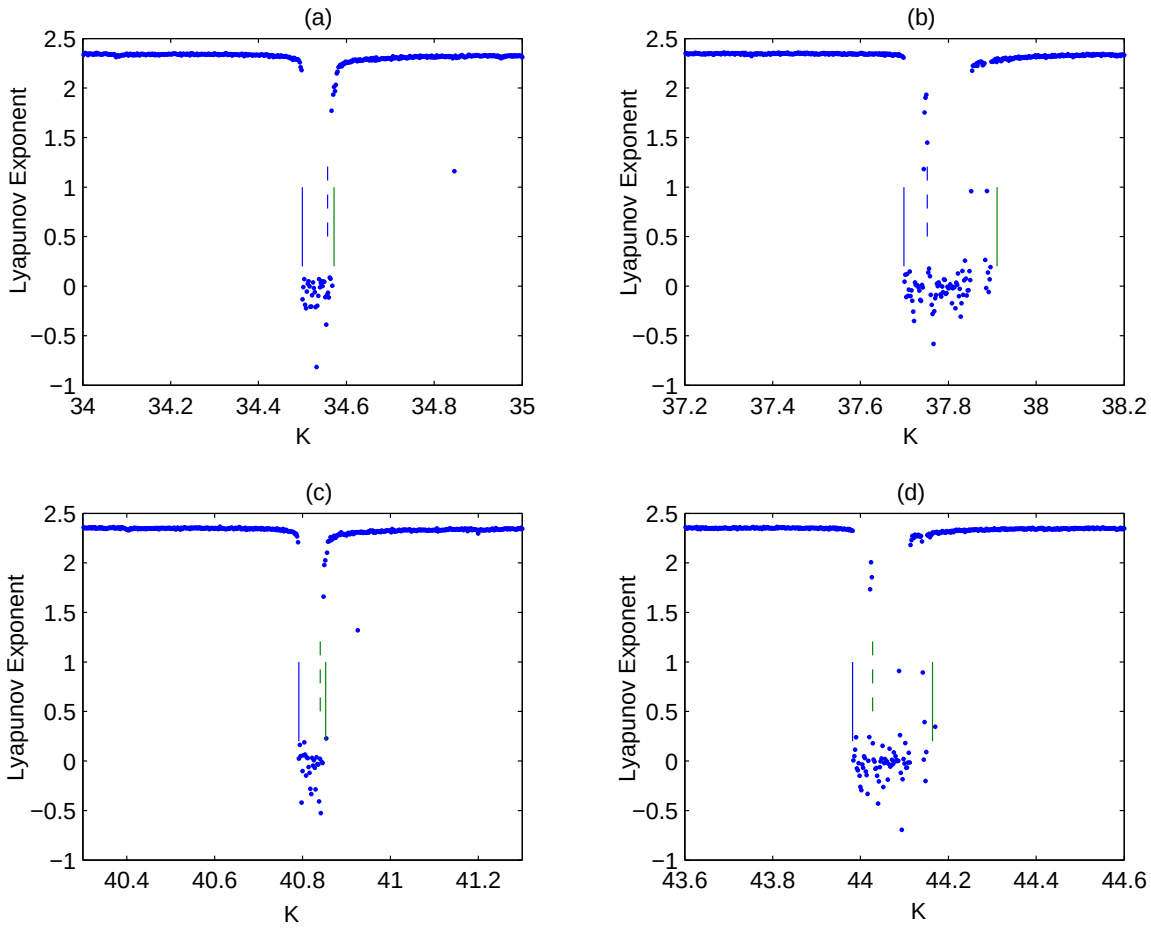

Figure B.2: Higher resolution on K for the Lyapunov exponent of the classical trajectories at Benettin *et al.* approach. $\Delta K = 0.002$ (a) $K = 11\pi$ region. Dashed line points to $K = 11\pi$ and solid lines illustrate region of Eq. (4.13) (b) $K = 12\pi$ region. Solid lines illustrate region of Eq. (4.12) while the dashed line is the right boundary of the second accelerator mode islands (c) $K = 13\pi$ region. Dashed line points to $K = 13\pi$ and solid lines illustrate region of Eq. (4.13) (d) $K = 14\pi$ region. Solid lines illustrate region of Eq. (4.12) and the dashed line is the right edge of the second accelerator mode islands.

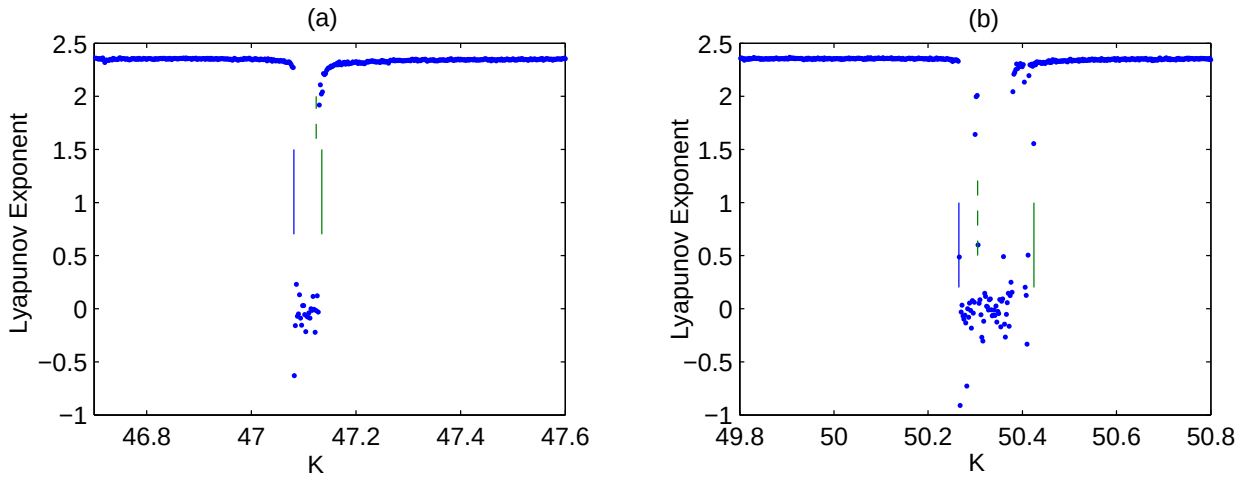

Figure B.3: Higher resolution on K for the Lyapunov exponent of the classical trajectories at Benettin *et al.* approach. $\Delta K = 0.002$ $K = 15\pi$ region. Dashed line points to $K = 15\pi$ and solid lines illustrate region of Eq. (4.13)

APPENDIX C

FIGURES OF CLASSICAL ANOMALOUS MOMENTUM DIFFUSION

We show more figures for the $\beta(K)$ and $D(K)$ of the anomalous diffusions for K within 100 similar to Fig 5.2 and Fig 5.3 in Chapter 5. All show that $\beta(K)$ is a little bit smaller than 2 and has a three-fold structure. $D(K)$ shows three-fold structure as well, due to the effects of higher order accelerator modes. In those figures the vertical solid bars indicate the position and width of the corresponding fundamental accelerator mode islands. The vertical dashed bar indicates the positive of the maximum anomalous momentum diffusion.

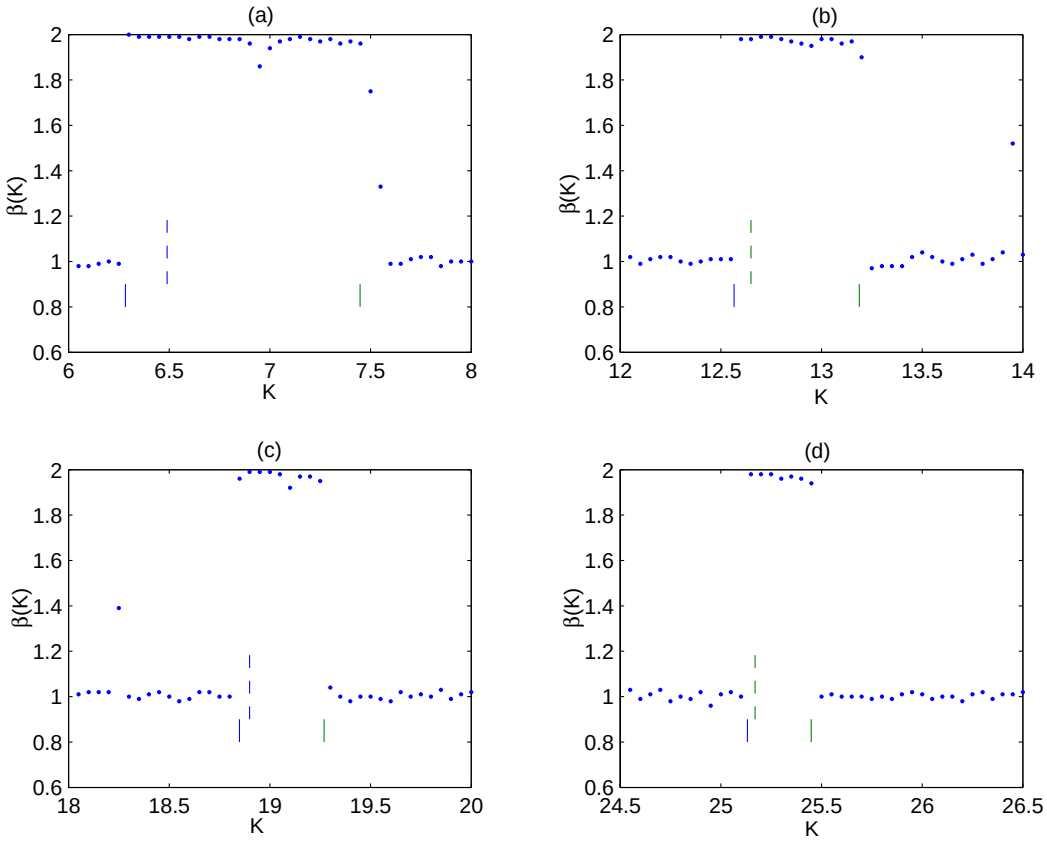

Figure C.1: Values of exponent $\beta(K)$ in Eq. (5.7) around nonlinear regions of anomalous diffusion for (a) $K_1 = 6.49$, (b) $K_2 = 12.65$, (c) $K_3 = 18.90$ and (d) $K_4 = 25.17$. The increment in K used for computation is $1/20$.

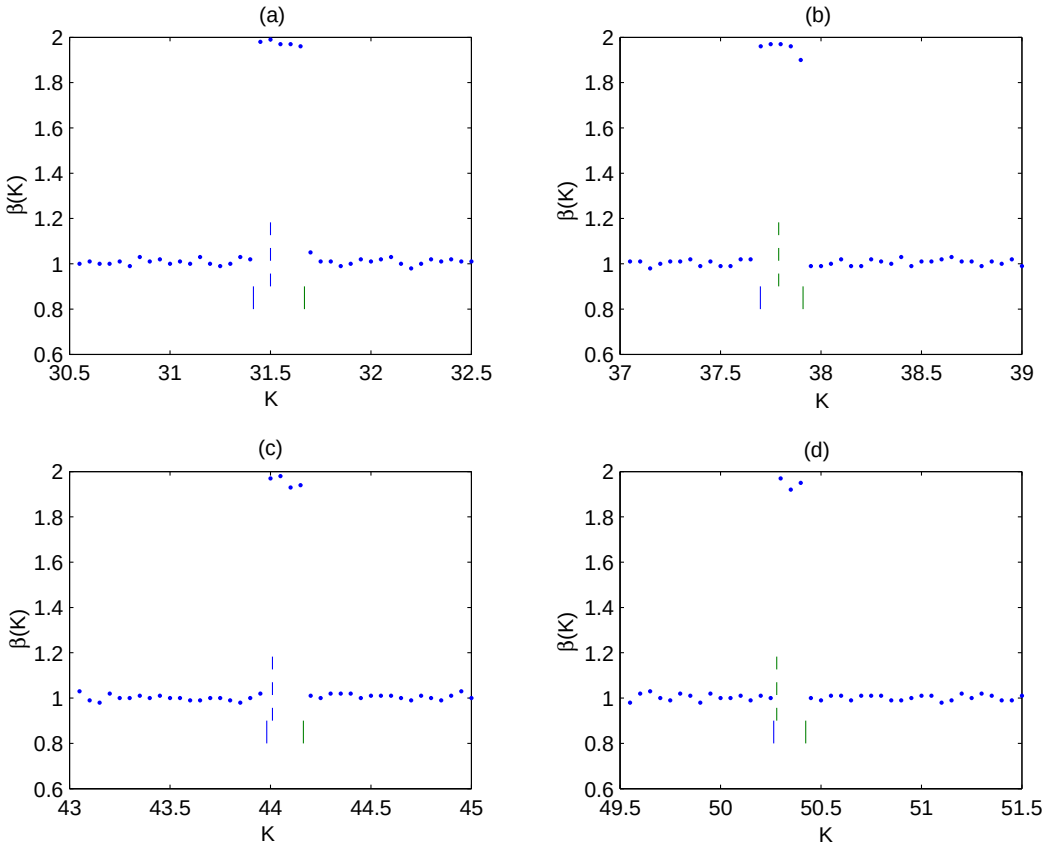

Figure C.2: Values of exponent $\beta(K)$ in Eq. (5.7) around nonlinear regions of anomalous diffusion for (a) $K_5 = 31.50$, (b) $K_6 = 37.79$, (c) $K_7 = 44.01$ and (d) $K_8 = 50.28$. The increment in K used for computation is $1/20$.

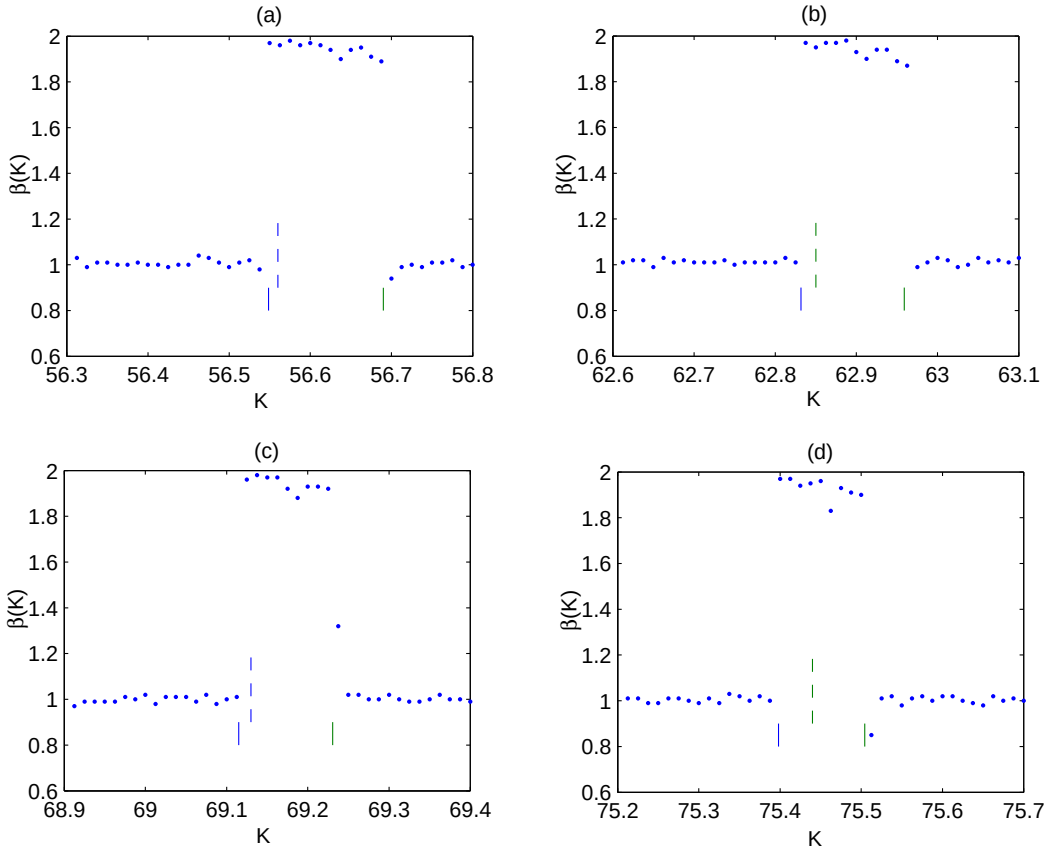

Figure C.3: Values of exponent $\beta(K)$ in Eq. (5.7) around nonlinear regions of anomalous diffusion for (a) $K_9 = 56.56$, (b) $K_{10} = 62.85$, (c) $K_{11} = 69.13$ and (d) $K_{12} = 75.44$. The increment in K used for computation is $1/80$.

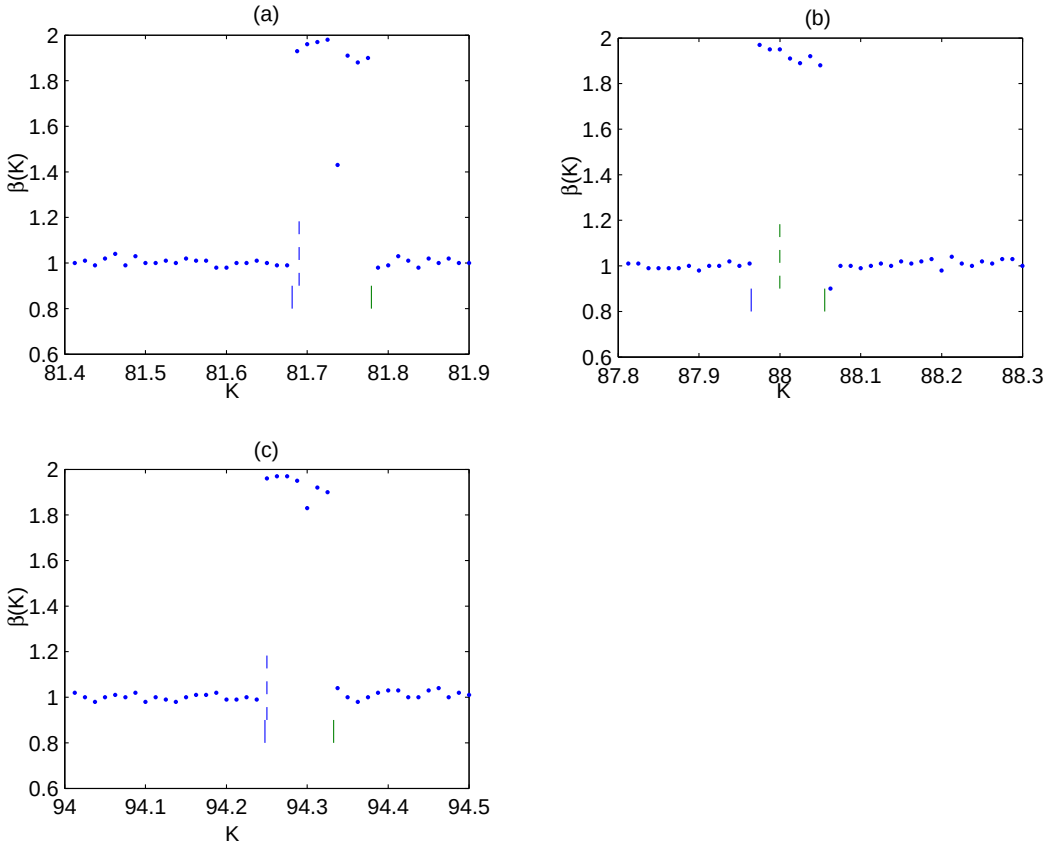

Figure C.4: Values of exponent $\beta(K)$ in Eq. (5.7) around nonlinear regions of anomalous diffusion for (a) $K_{13} = 81.69$, (b) $K_{14} = 88.00$, and (c) $K_{15} = 94.25$. The increment in K used for computation is $1/80$.

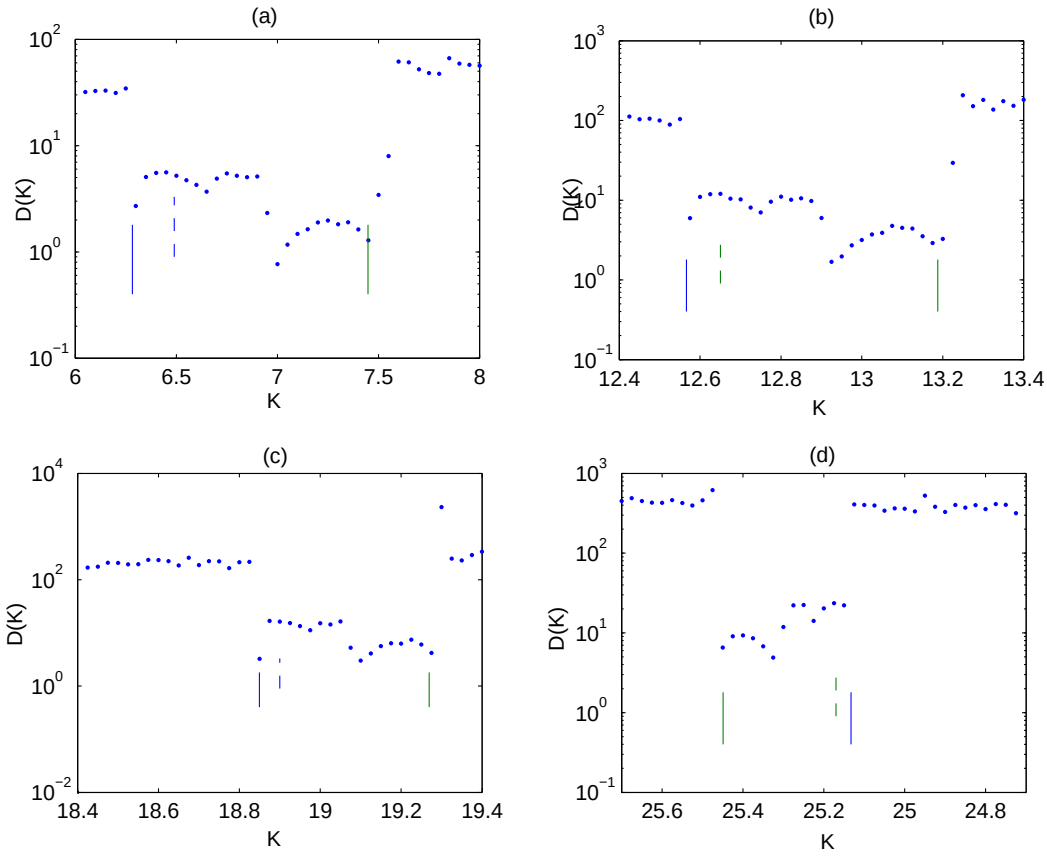

Figure C.5: Values of exponent $D(K)$ in Eq. (5.7) around nonlinear regions of anomalous diffusion for (a) $K_1 = 6.49$, (b) $K_2 = 12.65$, (c) $K_3 = 18.90$ and (d) $K_4 = 25.17$. The increment in K used for computation is $1/20$ for (a) while $1/40$ for (b), (c), and (d).

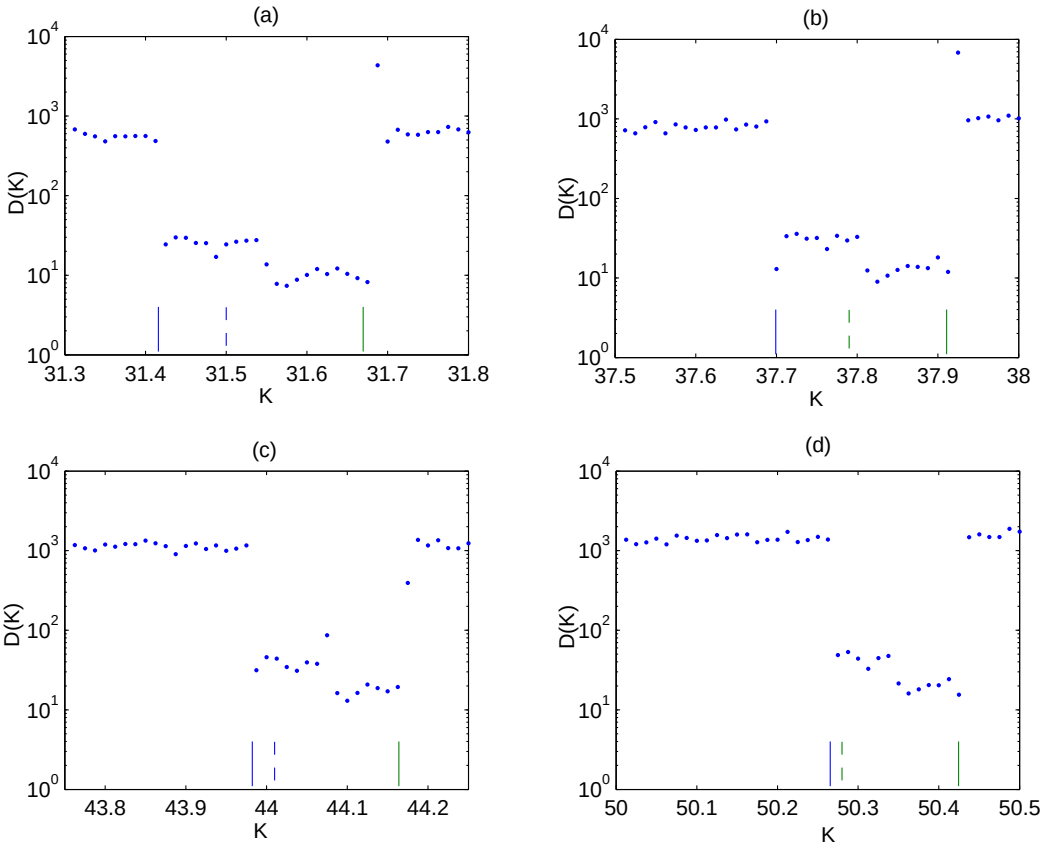

Figure C.6: Values of exponent $D(K)$ in Eq. (5.7) around nonlinear regions of anomalous diffusion for (a) $K_5 = 31.50$, (b) $K_6 = 37.79$, (c) $K_7 = 44.01$ and (d) $K_8 = 50.28$. The increment in K used for computation is $1/80$.

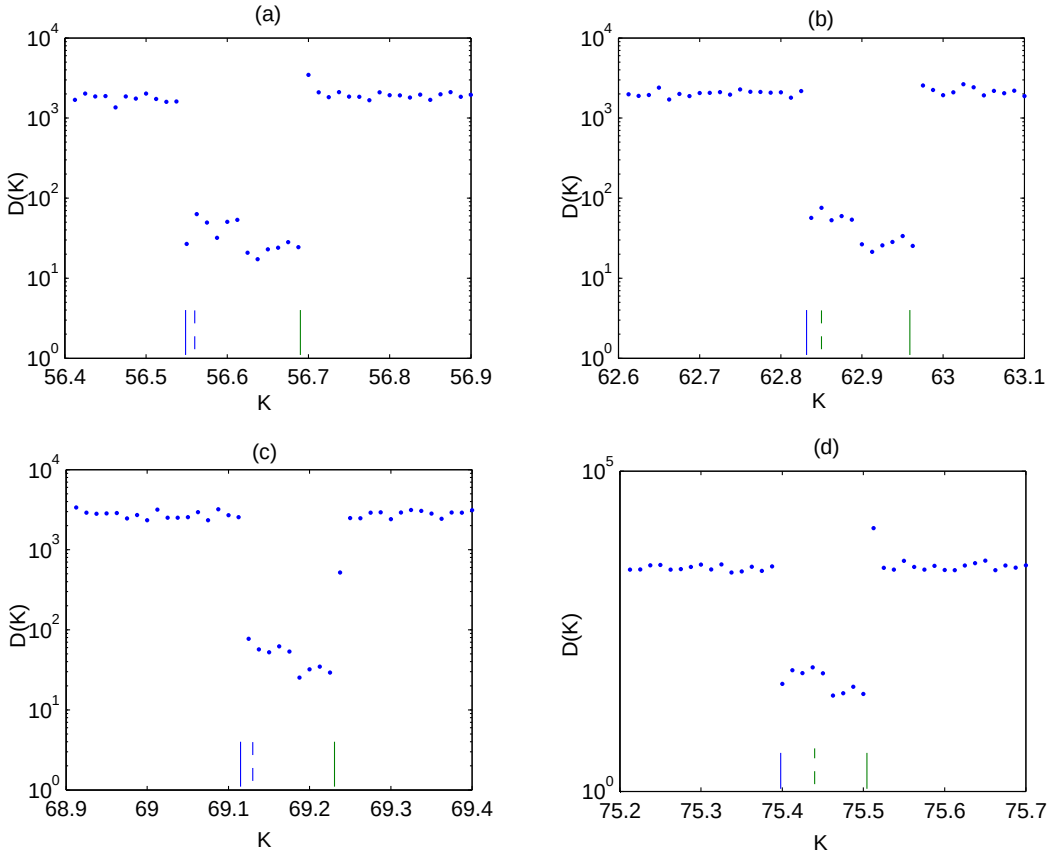

Figure C.7: Values of exponent $D(K)$ in Eq. (5.7) around nonlinear regions of anomalous diffusion for (a) $K_9 = 56.56$, (b) $K_{10} = 62.85$, (c) $K_{11} = 69.13$ and (d) $K_{12} = 75.44$. The increment in K used for computation is $1/80$.

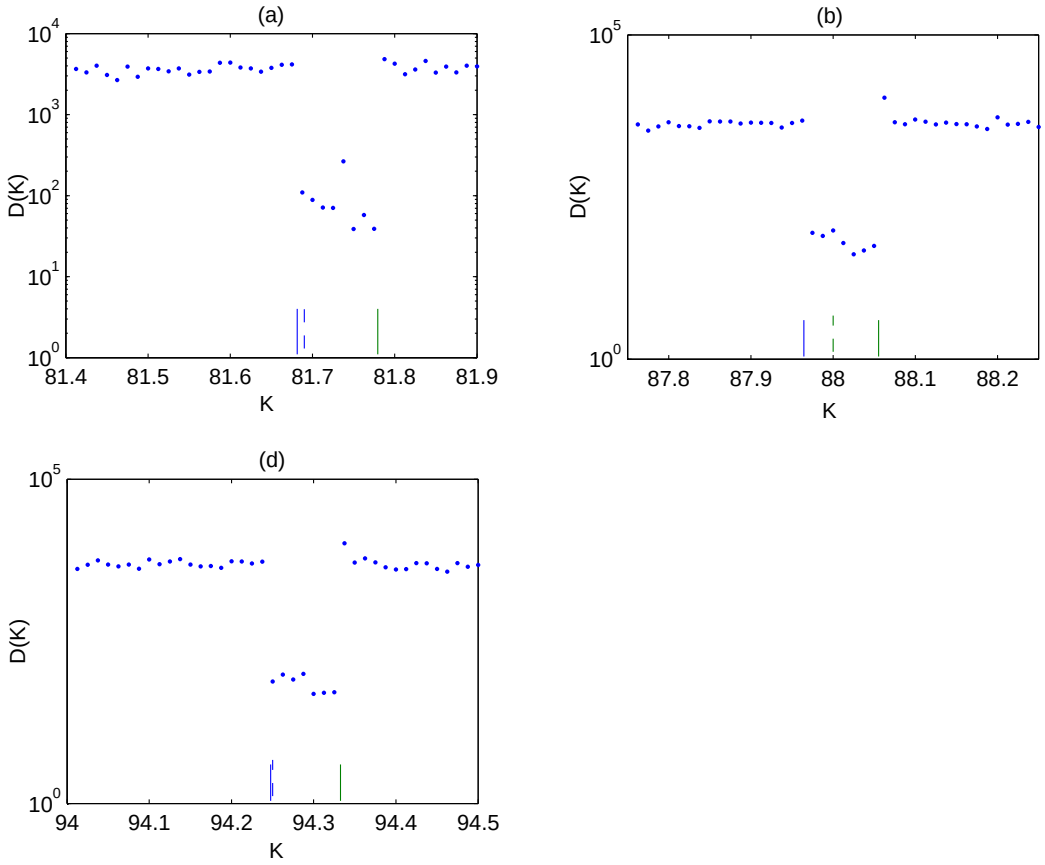

Figure C.8: Values of exponent $D(K)$ in Eq. (5.7) around nonlinear regions of anomalous diffusion for (a) $K_{13} = 81.69$, (b) $K_{14} = 88.00$, and (c) $K_{15} = 94.25$. The increment in K used for computation is $1/80$.

APPENDIX D

FIGURES OF QUANTUM STABILITY REGIONS IN THE CHAOTIC SEA

We show more figures for the quantum stability regions in the chaotic sea similar to Fig 6.3 in Chapter 6. Similar to those of classical regions, these regions occur in the areas surrounding an integer times π. The widths are much narrower, however. The vertical lines in these figures show the corresponding values of $l\pi$, where l is a positive integer.

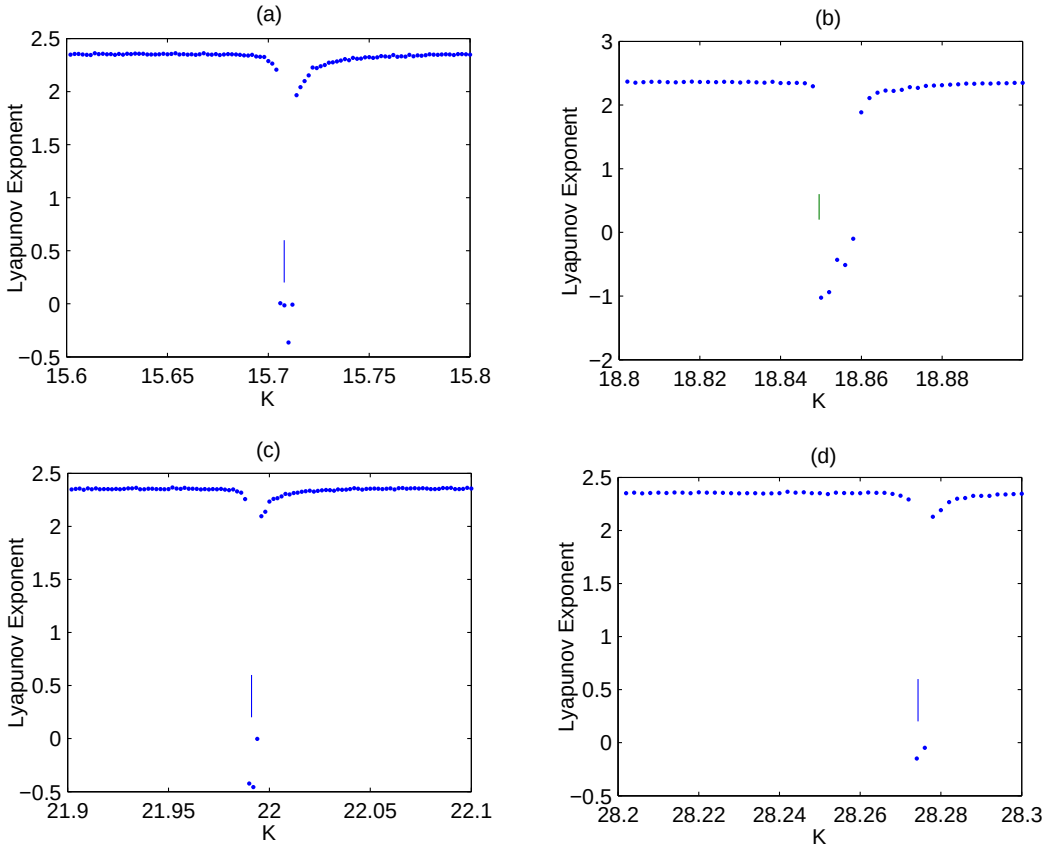

Figure D.1: Higher resolution on Lyapunov exponent of the Bohmian trajectories at Benettin *et al.* approach respecting to K. $\Delta K = 0.002$ (a) $K = 5\pi$ region, (b) $K = 6\pi$ region, (c) $K = 7\pi$ region (d) $K = 8\pi$ region.

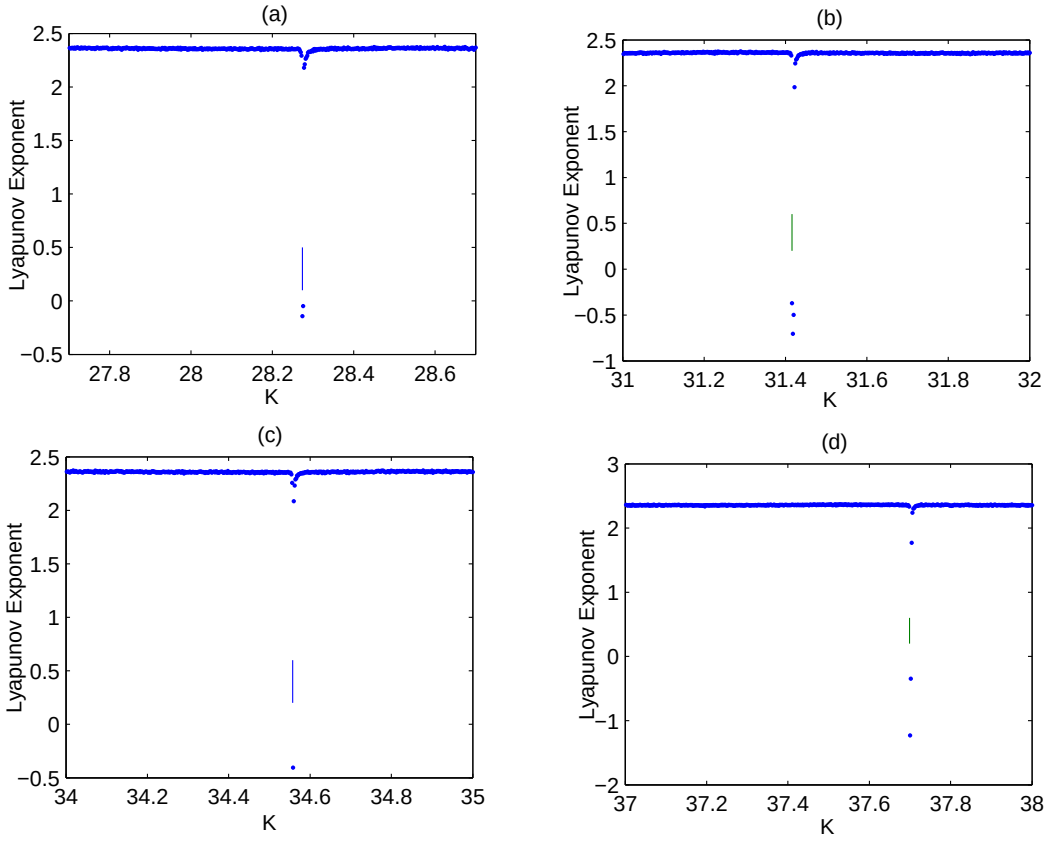

Figure D.2: Higher resolution on Lyapunov exponent of the Bohmian trajectories at Benettin *et al.* approach respecting to K. $\Delta K = 0.002$ (a) $K = 9\pi$ region, (b) $K = 10\pi$ region, (c) $K = 11\pi$ region (d) $K = 12\pi$ region.

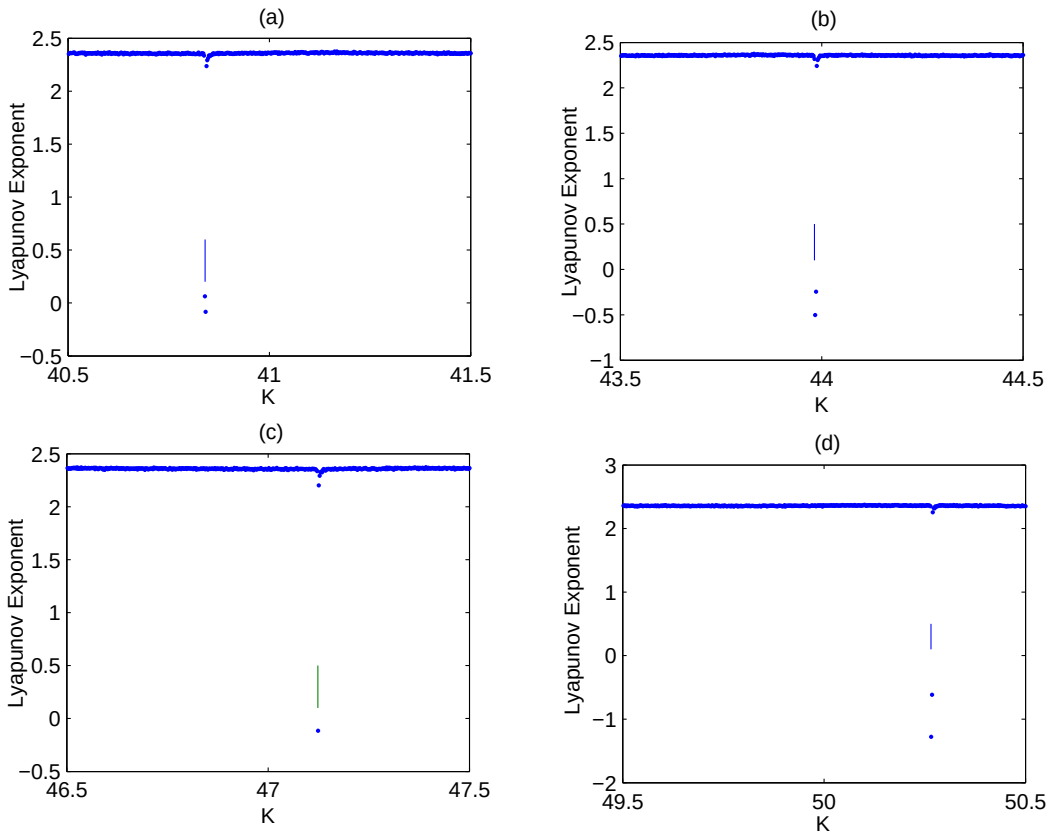

Figure D.3: Higher resolution on Lyapunov exponent of the Bohmian trajectories at Benettin *et al.* approach respecting to K. $\Delta K = 0.002$ (a) $K = 13\pi$ region, (b) $K = 14\pi$ region, (c) $K = 15\pi$ region (d) $K = 16\pi$ region.

BIBLIOGRAPHY

[1] H. Wu, and D. W. L. Sprung, Phys. Lett. A, 261 (1999) 150.

[2] H-J Stöckmann, *Quantum Chaos: an introduction* (Cambridge University Press, 1999).

[3] D. A. Steck, W. H. Oskay, and M. G. Raizen, Science, 293 (2001) 274.

[4] M. B. dArcy, R. M. Godun, D. Cassettari, and G. S. Summy, Phys. Rev. A 67, (2003) 023605.

[5] M. H. Partovi, Phys. Rev. Lett., 89 (2002) 144101.

[6] F. H. M. Faisal, and U. Schwengelbeck, Phys. Lett. A, 207 (1995) 31.

[7] F. M. Izrailev, Physics Reports, 196 (1990) 299.

[8] T. Prosen, M. and Znidaric, J. Phys. A: Mathematical and General, 35 (2002) 1455.

[9] Y. S. Weinstein, S. Lloyd, and C. Tsallis, Phys. Rev. Lett., 89 (2002) 214101.

[10] D. Bohm, Phys. Rev., 85 (1952) 166.

[11] D. Bohm, Phys. Rev., 85 (1952) 180.

[12] P. R. Holland, *The Quantum Theory of Motion - An Account of the de Broglie-Bohm Causal Interpretation of Quantum Mechanics* (Cambridge University Press, 1997).

[13] P. K. Chattaraj, S. Sengupta and A. Poddar, Current Science, 74 (1998) 758.

[14] U. Schwengelbeck, F. H. M. Faisal, Phys. Lett. A, 199 (1995) 281.

[15] A. B. Rechester and R.B. White, Phys. Rev. Lett., 44 (1980) 1586.

[16] B. V. Chirikov, Phys. Rept. 52 (1979) 263.

[17] G.M. Zaslavsky, Physics Reports 371 (2002) 461.

[18] C. Tian, A. Kamenev, and A. Larkin, Phys. Rev. Lett. 93 (2004) 124101.

[19] J. Gong, and P. Brumer, Phys. Rev. Lett. 86, (2001) 1741.

[20] M. E. K. Williams, M. P. Sadgrove, A. J. Daley, R. N. C. Gray, S. M. Tan, A. S. Parkins, N. Christensen and R. Leonhardt, J. Opt. B: Quantum Semiclass. Opt. 6 (2004) 28.

[21] M. Leibscher, I. Sh. Averbukh, P. Rozmej, and R. Arvieu, Phys. Rev. A 69, (2004) 032102.

[22] Y. Zheng and D. H. Kobe, Phys. Lett. A, 334 (2005) 306.

[23] A. Iomin and G. M. Zaslavsky, Phys. Rev. E, 63 (2001) 047203.

[24] J. Gong, H. J. Wörner, and P. Brumer, Phys. Rev. E 68, (2003) 026209.

[25] M. B. dArcy, R. M. Godun, M. K. Oberthaler, G. S. Summy, and K. Burnett, Phys. Rev. E, 64, (2001) 056233.

[26] M. Khodas, S. Fishman, and O. Agam, Phys. Rev. E 62 (2000) 4769.

[27] M. B. dArcy, R. M. Godun, M. K. Oberthaler, D. Cassettari, and G. S. Summy, Phys. Rev. Lett., 87 (2001) 074102.

[28] L. E. Reichl, *The Transition to Chaos* (Springer-Verlag, New York, 1992).

[29] M. C. Gutzwiller, *Chaos in Classical and Quantum Mechanics* (Springer-Verlag, New York, 1990).

[30] G. Benettin, L. Galgani, and J. Strelcyn, Phys. Rev. A, 14 (1976) 2338.

[31] M. Casartelli, E. Diana, L. Galgani and A. Scotti, Phys. Rev. A, 13 (1976) 1921.

[32] G. Tancredi, A. Sànchez and F. Roig, The Astronomical Journal, 121 (2001) 1171.

[33] F. L. Moore, J. C. Robinson, C. F. Bharucha, B. Sundaram, and M. G. Raizen, Phys. Rev. Lett. 75, (1995) 4598.

[34] A. C. Doherty, K. M. D. Vant, G. H. Ball, N. Christensen, and R. Leonhardt, J. Opt. B: Quantum Semiclass. Opt. 2 , (2000) 605-611.

[35] A. J. Daley, A.S. Parking, R. Leonhardt, and S. M. Tan, Phys. Rev. E., 65 (2002) 035201.

[36] H. Ammann, R. Gray, I. Shvarchuck, and N. Christensen, Phys. Rev. Lett., (1998) 4111.

[37] M. G. Raizen, Adv. At., Mol., Opt. Phys. 41, (1999) 43.

[38] M. Sadgrove, A. Hilliard, T. Mullins, S. Parkins, and R. Leonhardt, Phys. Re. E 70, (2004) 036217.

[39] T. Bhattacharya, S. Habib, and K. Jacobs, Phys. Rev. A, 65, (2002) 032115.

[40] V. Milner, D. A. Steck, W. H. Oskay, and M. G. Raizen, Phys. Rev. E, (2000) 7223.

[41] W. K. Hensinger, A. G. Truscott, B. Upcroft, N. R. Heckenberg, and H. Rubinsztein-Dunlop, J. Opt. B: Quantum Semiclass. Opt. 2 , (2000) 659.

[42] M. Bienert, F. Haug, W. P. Schleich, and M.G. Raizen, Fortschritte der Physik, 51, (2003) 474.

[43] Y. Zheng and D. H. Kobe, *Quantum Potential and Chaos of the Kicked Rotor*, Submitted manuscript.

[44] F. Haug, *Quantum Phenomina of Atoms in Standing Light Fields*, Ph. D. Dissertation, (2004).

[45] A. L.Lichtenberg and M. A. Lieberman, *Regular and Stochastic Motion* (Springer-Verlag, New York, 1992).

[46] E. Ott, *Chaos in Dynamical Systems* (Cambridge University Press 2002).

[47] L. E. Ballentine, Phys. Rev. A, 63 (2001) 024101.

[48] A. K. Pattanayak and P. Brumer, Phys. Rev. E, 56 (1997) 5174.

[49] B. Eckhardt and D. Yao, Physica D 65 (1993) 100.

[50] H. Shibata and R. Ishizaki, Physica A 197 (1993) 130.

[51] The MathWorks, Matlab 6.5, Release 13, (2002).

[52] D. Braum, *Disipative Quantum Chaos and Decoherence* (Springer Tracts in Modern Physics, Volume 172, 2001).

[53] D. Ruelle, *Chaotic Evolution and Strange Attractors* (Cambridge University Press, Cambridge, 1989) Chap. 9.1.

[54] I. Dana, Phys. Rev. E 69, (2004) 016212.

[55] J. D. Meiss, J. R. Cary, C. Grebogi, J. D. Crawford, A. N. Kaufman and H. D. I. Abarbanel, Physica 6D (1983) 375, eq. (10).

[56] A. Iomin, S. Fishman, and G. M. Zaslavsky, Phys. Rev. E, 65 (2002) 036215.

[57] Y. H. Ichikawa, T. Kamimura and T. Hatori, Physica 29D (1987) 247.

[58] R. Ishizaki, T. Horita, T. Kobayashi, and H. Mori, Prog. Theoret. Phys. 85 (1991) 1013.

[59] G. M. Zaslavsky, M. Edelman, and B. A. Niyazov, Chaos 7, (1997) 159.

[60] C. F. F. Karney, A. B. Rechester, and R. B. White, Physica 4D (1982) 425.

[61] Y. Zheng and D. H. Kobe, *Quantum Momentum Diffusion of the Kicked Rotor*, Submitted manuscript.

[62] A. Peres, *Quantum Theory: Concepts and Methods* (Kluwer Academic Publishers, Dordrecht, 1993).

[63] M. Feingold and A. Peres, Phys. Rev. A. 34 (1986) 591.

[64] S. A. Gardiner, J. I. Cirac, and P. Zoller, Phys. Rev. Lett. 79 (1997) 4790.

[65] M. K. Oberthaler, R. M. Godun, M. B. dArcy, G. S. Summy, and K. Burnett, Phys. Rev. Lett. 83 (1999) 4447.

[66] S. Fishman, I. Guarneri, and L. Rebuzzini, Phys. Rev. Lett., 89 (2002) 084101.

[67] F. M. Izrailev and D. L. Shepelyansky, Theor. Math. Phys., 43 (1980) 553.

[68] L. Cohen, in *Foundations of Quantum Mechanics,* eds. T. D. Black, M. M. Nieto, H. S. Pilloff, M. O. Scully, and R. M. Sinclair, (World Scientific, Singapore, 1992), pp. 78-90.